

THESIS FOR THE DEGREE OF DOCTOR OF PHILOSOPHY

Strategies to Mitigate the Degradation of Stainless-Steel Interconnects Used in Solid Oxide Fuel Cells

Claudia Göbel



CHALMERS

Department of Chemistry and Chemical Engineering
CHALMERS UNIVERSITY OF TECHNOLOGY

Göteborg, Sweden 2020

Strategies to Mitigate the Degradation of Stainless-Steel Interconnects Used in Solid
Oxide Fuel Cells

CLAUDIA GÖBEL

ISBN 978-91-7905-358-1

© CLAUDIA GÖBEL, 2020.

Doktorsavhandlingar vid Chalmers tekniska högskola

Ny serie nr 4825

ISSN 0346-718X

Department of Chemistry and Chemical Engineering

Chalmers University of Technology

SE-412 96 Göteborg

Sweden

Telephone: +46 (0)31-772 1000

Cover:

Top: Backscattered SEM micrographs of BIB milled cross-sections of Ce/Co-coated AISI 441 that was exposed to air at Sandvik Materials Technology for 7 000 h, 23 000 h, and 35 000 h. *Bottom:* Mass gain and area specific resistance values for Ce/Co-coated AISI 441 exposed to air at Sandvik Materials Technology at 800 °C.

Chalmers Reproservice

Göteborg, Sweden 2020

Strategies to Mitigate the Degradation of Stainless-Steel Interconnects Used in Solid Oxide Fuel Cells

CLAUDIA GÖBEL

Department of Chemistry and Chemical Engineering
Chalmers University of Technology

ABSTRACT

Interconnects are a vital part of solid oxide fuel cells (SOFC), where they electrically connect individual cells to form a fuel cell stack. They are a main contributor to the overall stack cost and the limited life-time of fuel cells, and, therefore, improvements carried out on the interconnect level could further the commercialization of SOFCs.

The limited life-time of the interconnect is related to the material used today, ferritic stainless steels (FSS). FSS interconnects are more cost-effective than previously used ceramics, but they degrade under the conditions prevalent in an SOFC: high temperatures between 600 °C and 850 °C, and a $p(\text{O}_2)$ gradient. Certain corrosion phenomena that occur, such as Cr evaporation and continuous oxide scale growth, negatively impact cell performance due to cathode poisoning and increased electrical resistance, respectively. These phenomena have been found to be effectively mitigated by coatings, such as the $(\text{Co,Mn})_3\text{O}_4$ (MCO) coating, or reactive element coatings, such as Ce.

The present thesis examines these coatings with regard to three aspects: (i) does the semi-conducting spinel coating affect the electrical resistance of the interconnect negatively, or is its conductivity negligible in comparison to the continuously growing Cr_2O_3 scale below it; (ii) does the coating self-heal if it is cracked even at intermediate temperatures, i.e. 650 °C and 750 °C, or do the cracks persist and increase Cr evaporation; and (iii) is the long-term stability of the state-of-the-art Ce/Co coating (10 nm Ce/640 nm Co) still effective after 35 000 h, or not. The second aspect is not only important to understand corrosion behavior, but it would also allow for large-scale roll-to-roll PVD coating, which is significantly more cost-effective than batch coating.

Another corrosion phenomenon that is elucidated within the scope of this work is the dual atmosphere effect. This effect leads to increased corrosion on the air-facing side of the interconnect if the FSS is exposed to a dual atmosphere, i.e. air on one side and hydrogen on the other side, compared to if the FSS is exposed to an air-only atmosphere. A new theory as to why the dual atmosphere effect occurs is proposed, and it is indirectly verified by means of excluding all other possibilities. Factors that influence the dual atmosphere effect are discussed, and it is shown how the dual atmosphere effect could, in part, be mitigated.

Keywords: Solid Oxide Fuel Cell; Corrosion; Interconnect; Cr Evaporation; Area Specific Resistance; Deformation; Long-term; Dual Atmosphere; Hydrogen

ACKNOWLEDGEMENTS

First and foremost I would like to thank my main supervisor Associate Professor Jan Froitzheim and my co-supervisor Professor Jan-Erik Svensson for giving me the opportunity to carry out my PhD studies in the SOFC group at Chalmers. Thank you for all the guidance you provided me with in the past years. The in-depth scientific discussions made me grow as a researcher, and the constant chocolate replenishment made me happy 😊.

A big part of my research work would not have been possible without the support of the entire SOFC group. Thank you for welcoming me so warmly into the group and for instructing me in the beginning of my PhD studies. Special thanks goes to Patrik, Maria, and Hannes who spent lots of time in the beginning showing me around the labs and teaching me how to do exposures, Cr evaporation measurements, and ASR measurements. In my experimental work I was often supported by my countless interns and thesis students, who produced a ton of results. Robin, Alex, Matthieu (who even came back for seconds and thirds), Maxime, Caterina, Thibault, and Sarah, thanks to all of you! I would also like to acknowledge Mohammad Sattari, for showing me how the BIB works and Vijay for investigating some of my samples with FIB/SEM and STEM. Of course, I would also like to thank all of the "newer" SOFC staff, Alberto, Anton, Özgür, Matthieu, and Reddy, for bringing in new perspectives into the group. This has led to the SOFC group revising the humidifying systems, improving our ASR systems, giving us a sound solution of the dual atmosphere mechanism, and continuing the neutron work that was started up together by Jan, Maths, Lars-Gunnar, Laura and me.

I would also like to give my appreciation to the entire Energy and Materials Division. Thank you for welcoming me into the group and for always helping me, when I asked for it. Also thank you for all the after-work celebrations, which helped with the frustration that is part of research every now and then. Special thanks goes to Christine and Loli for ordering lab ware for me and providing interesting science related or non-science related conversations, and to Sedi, who did some last-minute FactSage calculations for me.

I would also like to thank all our industrial partners for providing us with interesting new research questions and good discussions. A special thanks goes to AB Sandvik Materials Technology with whom I have also published a paper, and to Ceres Power for providing me insights into the fuel cell industry.

Thanks to the administrators, current and former, of our group; Sandra, Susanne, Anna and Christina; for helping me out with all the administrative things and for managing to find places for all my interns. And thank you to Esa and Torbjörn, for technical support.

High quality research always requires funding, so I would also like to acknowledge all the funding we received, from the High Temperature Corrosion Centre, the Swedish Energy Agency, and the FFI program. Additionally this work was performed in part at the Chalmers Materials Analysis Laboratory, CMAL.

I wouldn't be here today, without the support of my family, especially my parents Christine and Karl, and all my close friends. Thank you for your continuous support, especially in times when I was very stressed or felt home sick, I would have never gotten this far without you. And last, but not least, I want to thank Hannes for always supporting me and urging me on in the last few months and for answering all my work related questions even when he was working himself!

LIST OF PUBLICATIONS

This thesis is based on the following papers:

- I C. Göbel, A. G. Fefekos, J.-E. Svensson and J. Froitzheim. Does the Conductivity of Interconnect Coatings Matter for Solid Oxide Fuel Cell Applications? *Journal of Power Sources* **383** (2018), 110-114.
- II C. Göbel, V. Asokan, S. Khieu, J.-E. Svensson and J. Froitzheim. Self-Healing Properties of Ce/Co-Coated Stainless Steel Under Simulated Intermediate Temperature Solid Oxide Fuel Cell Conditions. *Manuscript*.
- III C. Göbel, R. Berger, C. Bernuy-Lopez, J. Westlinder, J.-E. Svensson and J. Froitzheim. Long-Term (4 Year) Degradation Behavior of Coated Stainless Steel 441 Used for Solid Oxide Fuel Cell Interconnect Applications. *Journal of Power Sources* **449** (2020), 1-7.
- IV K. O. Gunduz, A. Chyrkin, C. Göbel, L. Hansen, O. Hjorth, J.-E. Svensson and J. Froitzheim. The Effect of Hydrogen on the Breakdown of the Protective Oxide Scale in Solid Oxide Fuel Cell Interconnects. *Manuscript*.
- V C. Göbel, P. Alnegren, R. L. Faust, J.-E. Svensson and J. Froitzheim. The Effect of Pre-Oxidation Parameters on the Corrosion Behavior of AISI 441 in Dual Atmosphere. *International Journal of Hydrogen Energy* **43** (2018), 14665-14674.
- VI C. Göbel, C. Bo, J.-E. Svensson and J. Froitzheim. The Influence of Different Factors on the Dual Atmosphere Effect Observed for AISI 441 Interconnects Used in Solid Oxide Fuel Cells. *ECS Transactions* **91** (2019), 2261-2266.

Statement of author's contribution

With the exception of Paper IV, I was the main author of all appended papers. A more detailed description of my contribution to the papers is given below.

The area specific resistance measurements and the x-ray diffraction analysis in Paper I were done in part by Alexander G. Fefekos within the scope of an internship under my supervision. I carried out the micro-structural analysis using scanning electron microscopy (SEM), and I wrote the paper.

Some of the Cr evaporation measurements in Paper II were carried out by Sarah Khieu as part of her internship under my supervision. The focused ion beam (FIB) milling and subsequent energy dispersive x-ray (EDX) mapping with transmission electron microscopy (TEM) was conducted by Dr. Vijay Asokan. I completed the Cr evaporation measurements, carried out broad ion beam (BIB) milling and SEM/EDX mapping, and wrote the paper.

Sandvik Materials Technology exposed the samples for up to 37 000 h for Paper III, and I did the subsequent analysis of those samples, e.g. Cr evaporation measurements, area resistance measurements, and micro-structural investigations, and wrote the paper.

I was mainly involved in the experiment planning for Paper IV, including deciding on an experimental matrix, and I helped Dr. Kerem Ö. Gunduz with some of the microstructural analysis.

Part of the experimental work on the influence of pre-oxidation location on the dual atmosphere effect in Paper V was conducted by Robin Faust within the scope of his master thesis under my supervision. I performed all other experimental work, and I wrote the paper.

Caterina Bo carried out most of the experiments for Paper VI within the scope of her master thesis under my supervision. I conducted the SEM analysis and wrote the paper.

Related Work

The following papers are related to the work discussed in this thesis:

C. Göbel, R. Berger, M.W. Lundberg, J. Westlinder, J.-E. Svensson and J. Froitzheim. Long Term (4 Years) Performance of Co/Ce Coated 441 for SOFC Interconnect Applications. *ECS Transactions* **78** (2017), 1675-1679.

C. Göbel, P. Alnegren, R.L. Faust, J.-E. Svensson and J. Froitzheim. Influence of Pre-Oxidation on Dual Atmosphere Effect on AISI 441 Interconnects for Solid Oxide Fuel Cell Applications. *ECS Transactions* **78** (2017), 1559-1563.

M. Tomas, C. Göbel, J.-E. Svensson and J. Froitzheim. Cu-Based Coatings For IT-SOFC Applications. *ECS Transactions* **91** (2019), 2291-2298.

LIST OF ACRONYMS

APU	Auxiliary Power Unit
ASR	Area Specific Resistance
BF	Box Furnace
BCC	Body-Centered Cubic
BSE	Backscattered Electron
CGO	Gadolinia-Doped Ceria
CHP	Combined Heat and Power
EDX	Energy Dispersive X-ray Spectroscopy
FCC	Face-Centered Cubic
FIB	Focused Ion Beam
FSS	Ferritic Stainless Steel
GB	Grain Boundary
HAADF	High-Angle Annular Dark-field
InCF	Intrinsic Chemical Failure
IOZ	Internal Oxidation Zone
IT	Intermediate Temperature
LSGM	Sr and Mg doped LaGaO ₃
LSM	Sr-doped LaMnO ₃
MCO	(Mn,Co) ₃ O ₄
MICF	Mechanically Induced Chemical Failure
MIEC	Mixed Ionic and Electronic Conductors
PBR	Pilling and Bedworth Ratio
PEMFC	Proton-Exchange Membrane Fuel Cell
PVD	Physical Vapor Deposition
RE	Reactive Elements
SE	Secondary Electron
SEM	Scanning Electron Microscopy
SHE	Standard Hydrogen Electrode
SMT	Sandvik Materials Technology
SOFC	Solid Oxide Fuel Cell
STEM	Scanning Transmission Electron Microscopy
TEC	Thermal Expansion Coefficient
TF	Tube Furnace
TPB	Triple-Phase-Boundary
UV-VIS	Ultraviolet-Visible
XRD	X-Ray Diffraction
YSZ	Yttria Stabilized Zirconia

CONTENTS

Abstract	iii
Acknowledgements	iv
List of Publications	v
List of Acronyms	vii
Contents	ix
1 Introduction	1
1.1 Background	1
1.2 Aim of this Thesis	4
1.2.1 Coatings as a Strategy to Increase Life-Time of Interconnects - Papers I to III	4
1.2.2 Dual Atmosphere Corrosion - Papers IV to VI	5
2 Theory	7
2.1 Fuel Cells	7
2.1.1 Background - Electrochemistry	7
2.1.2 Introduction to Fuel Cells	8
2.1.3 Solid Oxide Fuel Cell	10
2.2 Oxidation Theory	13
2.2.1 Thermodynamics	13
2.2.2 Kinetics	14
2.2.3 Oxide Properties	19
2.2.4 Oxidation of Alloys	22
2.3 Oxidation of Ferritic Stainless-Steel Interconnects	24
2.3.1 Material Selection	24
2.3.2 Protective Coatings	27
2.3.3 Electrical Conductivity of Oxide Scales	29
2.3.4 The Dual Atmosphere Effect	32
3 Materials and Methods	35
3.1 Materials	35
3.2 Exposures	36
3.2.1 Cr Evaporation Measurements	38
3.2.2 Long-Term Exposures	39
3.2.3 Dual Atmosphere Exposures	39
3.3 Analytical Methods	42
3.3.1 Spectrophotometry	42
3.3.2 Area Specific Resistance	44
3.3.3 X-Ray Diffraction	44
3.3.4 Ion Beam Milling	46

3.3.5	Electron Microscopy	47
4	Results and Discussion	51
4.1	Nano-Coatings and their Influence on Corrosion Properties	51
4.1.1	Co Coating Thickness and Its Influence on Area Specific Resistance	51
4.1.2	Self-healing Capabilities of Ce/Co Coating at Intermediate Temperatures .	54
4.1.3	Long-Term Stability of Ce/Co-Coated AISI 441	59
4.2	The Dual Atmosphere Effect	64
4.2.1	Temperature Dependence	64
4.2.2	Pre-oxidation and its Influence on the Dual Atmosphere Effect	72
4.2.3	Influence of Material Thickness	77
4.2.4	Influence of Surface Treatment	78
4.2.5	Discrepancy in the Literature	80
5	Summary	85
	References	89

Introduction

1.1 Background

In 2019, the Oxford Dictionary named "climate emergency" as the word of the year. At the same time, large areas in Australia were in flames, over 17 million hectares had burned at the end of the fire season in Australia, and the US was fighting hurricane after hurricane. Of course climate change sceptics often say Australia has always had bush fires and the US has always had hurricanes, but many studies suggest that the frequency and the extent of these weather conditions have increased significantly in recent years, and a correlation of these events with climate change is hard to deny [1–4]. The danger of climate change has also reached the general populace, and, in over 150 countries all over the world, the Fridays for Future movement has developed and expanded and is supported by many researchers all across the world [5, 6]. All these points stress how important it is to finally act on a large-scale world-wide level.

But the question is: What is needed to actually circumvent or at least limit global warming and, thus, climate change?

The first important step to answering this question is to understand that climate change is a normal occurrence on earth, with glacial periods and warmer and dry periods alternating. However, starting with the industrial revolution in the late 17th century a dramatic increase in atmospheric CO₂ levels occurred and is still ongoing (see Figure 1.1a) [7–10]. Besides other greenhouse gases, such as methane and nitrous oxide, CO₂ is one of the reason for climate change, and, thus, the reduction of greenhouse gas emissions is crucial in the fight against global warming. As shown in Figure 1.1b, electricity and heat production account for the highest greenhouse gas emissions world-wide, and, therefore, a change in this sector would be most effective. A revolution in this sector has already begun, and across the world green energy technologies are being used. However, most renewable energy sources are intermittent, such as wind and solar power, and, therefore, energy storage systems are extremely important as grid scale storage systems. One option amongst many is to store energy in a fuel, for example, hydrogen [11]. The advantages of this technique are especially important for long-term storage facilities, because, unlike batteries, negligible self-discharge rates are present as the energy is stored in chemical bonds, and the energy density by mass of hydrogen as a fuel is higher than that of any other energy storage device or carrier [12, 13]. Different technologies are needed to use hydrogen as a storage medium. First, electrolyzers are important to convert excess electrical energy into fuel, and then fuel cells are used to convert the chemical energy

stored inside the fuel back to electrical energy (see Figure 1.2). The present work focuses on a fuel cell as a device that converts the chemical energy of a fuel into electrical energy via a controlled reaction and without or with reduced greenhouse gas emission, depending on the fuel used. In addition to supplying electricity for housing and industry, fuel cells can also be used in other sectors, for example, the transportation sector, which also contributes greatly to the overall greenhouse gases produced by humankind (see Figure 1.1b).

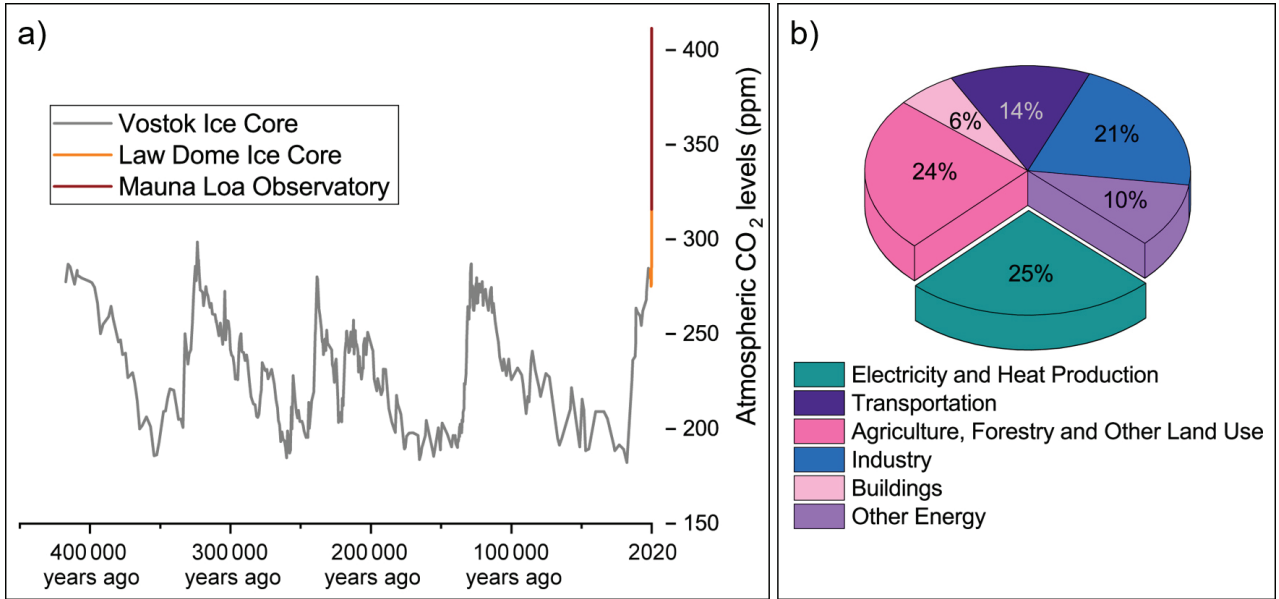


Figure 1.1: A) Atmospheric CO₂ levels over the last 425 000 years. The data was collected by Barnola et al. [8] from the Vostok ice core, Etheridge et al. [10] from the Law Dome ice core and Tans et al. [9] from the Mauna Loa Observatory. B) Global greenhouse gas emissions by economic sector, based on global emissions from 2010 and reported in [14].

As with many types of technologies, there are different types of fuel cells, each with a different set of advantages and disadvantages. Today the most widely spread and also the most commonly researched fuel cell types are proton exchange membrane fuel cells (PEMFC) and solid oxide fuel cells (SOFC). The main difference between these two types is that PEMFCs require a Pt catalyst for a reaction to occur sufficiently fast, while SOFCs operate at high temperatures ($\geq 550^\circ\text{C}$) to achieve the same effect. This difference leads to disadvantages and/or advantages of the different fuel cell types. High temperatures can be avoided by using a Pt catalyst, and the operating temperatures of PEMFCs range between 70 and 130 $^\circ\text{C}$, however, in addition to the high cost of Pt, another drawback is that these fuel cells can only operate on high purity H₂ as the fuel. In contrast, SOFCs require high temperatures that lead to longer start-up times and safety concerns for mobile applications. However, there is no need for expensive catalysts, and many different fuels can be used for SOFCs. Another advantage SOFCs have is their extremely high electrical efficiency, above 60 % [15], in comparison to a PEMFC, which has an electrical efficiency up to 50 % [16]. The overall efficiency of SOFCs can be increased even further by using the waste heat that the fuel cell produces either for heating or for additional

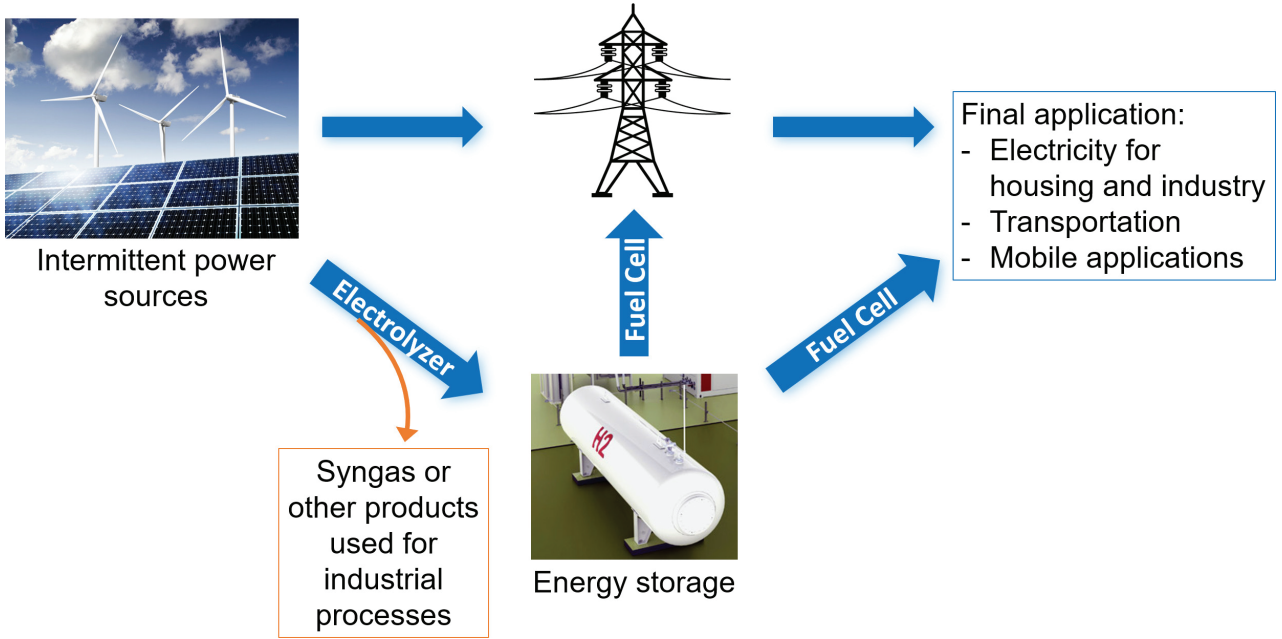


Figure 1.2: *Renewable electricity is stored in a fuel, and subsequently, converted into electricity.*

energy generation, for example with steam turbines. Reported overall system efficiencies of up to 90 % are common for SOFCs [15, 17–19].

The main issues to overcome before wide-spread commercialization of fuel cells can be achieved are threefold: sufficient infrastructure, especially with refueling stations; competitive cost, especially in comparison with similar green energy conversion systems; and long life-times (at least 5 000 h for mobile applications and 60 000 h for stationary applications according to the US Department of Energy [20, 21]). The infrastructure for SOFCs might be less of an issue, due to their fuel flexibility, which even allows for the use of diesel reformat [19] and biodiesel [22]. However, the cost and the life-time of fuel cells still need to be improved drastically. In the present work both of these factors will be addressed by focusing on one essential part of the fuel cell, the interconnect, which contributes greatly to both factors.

The main function of the interconnect in an SOFC is to electrically connect individual fuel cells to form a fuel cell stack, but, additionally, it also serves to separate the two gases used to power the fuel cell: air on the cathode side and the fuel, e.g. H_2 , on the fuel side. These two functions of the interconnect lead to several requirements, such as good electrical conductivity, stability in low and high $p(O_2)$ environments, impermeability to the gases used, and ease of formability so that gas channels can be shaped [23]. Ferritic stainless steels (FSS) fulfill most of these requirements and are additionally much cheaper than previously used ceramics and, consequently, are the material of choice nowadays. Nevertheless, cost remains an issue, and the contribution of the interconnect to the overall fuel cell stack cost has been estimated between 6 to 45 % of the fuel cell manufacturing stack cost for an SOFC [24–26].

The other major limitation of ferritic stainless-steel interconnects is that they corrode in the environment prevalent in SOFC, i.e. low and high $p(O_2)$ with high temperatures

between 600 and 850 °C. This leads to many other issues. For example, the continuous oxidation of the FSS results in a growing Cr_2O_3 layer, which increases the interconnect's electrical resistance, and leads to continuous Cr consumption. The Cr consumption is further increased by another corrosion phenomenon, the evaporation of Cr-containing species [27–30]. While this evaporation can lead to a decrease in oxide scale thickness, it not only increases Cr consumption, which could lead to Cr depletion of the FSS, but more importantly it results in poisoning of the cathode, which leads to cell degradation and eventual failure of the entire SOFC.

The long-term performance of the SOFC is often directly related to the life-time of the interconnect, and, therefore, the corrosion of the interconnect must be mitigated. One very effective method to achieve this is by applying coatings to the interconnect, which decrease oxide scale growth and Cr evaporation. These coatings become especially relevant when cheaper interconnect materials are used to decrease the fuel cell cost further, as cheaper materials often contain less Cr and/or less reactive elements, which decelerate oxide scale growth. Therefore, it is vital to decrease all Cr-consuming processes that occur at the interconnect level, and in that way, avoid Cr depletion and material failure of the interconnect.

Another unrelated corrosion mechanism that affects FSS interconnects and, thus, impacts the fuel cell life-time, is dual atmosphere corrosion. In dual atmosphere, i.e. air on one side of the interconnect and hydrogen as the fuel on the other side, the corrosion on the air-facing side can be increased under certain circumstances compared to an air-only atmosphere. This increase in corrosion can lead to the formation of unwanted and fast growing Fe-rich oxides on the air-facing side [31, 32]. This corrosion phenomenon is to-date poorly understood and, thus, mitigation strategies are non-existent.

All these issues related to cost and life-time must be addressed and solved to achieve wide-spread commercialization of the solid oxide fuel cell system, and, therefore, research focusing on the interconnect is crucial.

1.2 Aim of this Thesis

The aim of the present thesis is to address some of the aforementioned issues and hopefully further the understanding of corrosion mechanisms occurring on the interconnect level and evaluate coatings as a mitigation strategy. For this the thesis is split into two parts: the first part will focus on coatings as a mitigation strategy, while the second part will focus on the dual atmosphere corrosion mechanism.

1.2.1 Coatings as a Strategy to Increase Life-Time of Interconnects - Papers I to III

Coatings are applied onto the interconnect for two reasons, first to decelerate oxide scale growth and second to mitigate Cr evaporation. Therefore, coatings play a vital role in extending the interconnect life-time. The most common coatings nowadays are spinel oxide coatings, due to their high Cr retention rates [33, 34] and reactive element coatings, due to their ability to reduce the oxide scale growth rate [35, 36]. While the latter

coating is typically applied in very thin layers (up to 100 nm thin), the thickness of the spinel coating is much thicker ($\geq 1 \mu\text{m}$) and varies greatly, with investigations carried out on $1.5 \mu\text{m}$ [37] to $50 \mu\text{m}$ [38] thick spinel coatings. Because the spinel coating is fairly thick, the question arises if or when the conductivity of the coating negatively effects the overall conductivity of the interconnect. Many different publications have, therefore, focused on increasing the conductivity of the coating, for example, by adding dopants [39–46]. However, because the thermally grown Cr_2O_3 is a very poor electron conductor and most of the spinel coatings are much better electron conductors at the SOFC operating temperatures, the conductivity of the latter might not be significant for the overall conductivity of the interconnect. The present work tries to answer this question by examining the area specific resistance (ASR) of Crofer 22 APU, which was coated with different Co coating thicknesses and exposed at the same temperature for the same duration. A very low exposure temperature was chosen (600°C), which should result in a very thin Cr_2O_3 scale in comparison to fairly thick Co coatings, thus, resembling an extreme situation.

An additional study that was carried out within the scope of this thesis investigated the self-healing properties of Co coatings at intermediate temperatures. It has previously been shown by *Falk-Windisch* et al. [47, 48] that cracks that had formed in the coating, healed quickly during exposure at 850°C due to rapid Co diffusion into the cracks. This allows for the interconnect to first be coated and then deformed, which has the benefit that the steel can be strip coated instead of batch coated. Strip coating is the economically favorable manufacturing route, but cracks are introduced into the coating during the subsequent deformation step. However, the self-healing process has to-date only been investigated at 850°C , and nowadays there is a clear trend towards intermediate temperature SOFCs (IT-SOFC) with operating temperatures ranging from 600 to 750°C [49–51]. Because the self-healing process relies on Co diffusion, which is temperature controlled as a diffusion process, the self-healing process might not occur at a high enough rate at lower temperatures. The present work investigates this process at 650°C and 750°C .

Another important question when it comes to coatings is: how long do they last and can they fulfill the requirement of life-times above 40 000 h. In general, long-term investigations are scarce for interconnect materials and only few coatings have been investigated for life-times above 3 000 h. Some studies on longer life-times can be found in [52–55]. To investigate the longevity of coated interconnects further, the present thesis analyzes Ce/Co-coated AISI 441, which was exposed at 800°C for up to 38 100 h. The material is especially interesting as AISI 441 is a comparably cheap steel. The state-of-the-art coating (10 nm Ce/640 nm Co) [56, 57] shows good Cr-retention properties along with a decrease in the oxide scale growth rate for exposure times below 3 000 h [58, 59]. However, long-term data on this coating does not yet exist.

1.2.2 Dual Atmosphere Corrosion - Papers IV to VI

Finally, the present thesis examines the dual atmosphere effect in more detail. This effect occurs when an FSS is exposed to fuel on one side and air on the other side, and it leads to increased corrosion on the air-facing side, which does not occur in an air-only atmosphere. The present work analyzes this effect with regard to different factors:

- Exposure temperature, i.e. which exposure temperature has the most severe dual atmosphere effect and what conclusions about the mechanism can be drawn from that?
- Pre-oxidation, i.e. how does pre-oxidation influence the dual atmosphere effect, especially with regard to the pre-oxidation time and the pre-oxidation location, and how can this knowledge be used to mitigate the dual atmosphere effect?
- Sample thickness, i.e. does the sample thickness affect the dual atmosphere effect?
- Surface modification, i.e. how does the surface morphology achieved, for example, by grinding or polishing, influence the dual atmosphere effect?

A new mechanism is proposed for the dual atmosphere effect through an examination of these factors and how they influence the effect, and conclusions on mitigation strategies against the dual atmosphere effect are drawn.

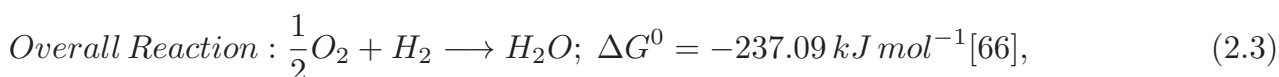
Before presenting and discussing the results (see Chapter 4) that were obtained within the scope of this thesis, more details are given on the fuel cell system, high temperature corrosion, and the background to the studies carried out in this thesis (see Chapter 2). Information on the experimental setups used in this thesis is given in Chapter 3. Results and conclusions are summarized in Chapter 5.

2.1 Fuel Cells

2.1.1 Background - Electrochemistry

Fuel cells, as a way to generate energy by converting chemical energy into electrical energy, were first described in 1838/1839 separately by two scientists, William Grove [60, 61] and Christian Friedrich Schönbein [62]. However, the working principle on which fuel cells are based, the galvanic or voltaic cell, had already been demonstrated in 1780 [63, 64] by Luigi Galvani and explained in 1790 by Alessandro Volta [65]. These discoveries opened up a new research field: Electrochemistry, which has led to the discovery of many different green energy technologies, such as fuel cells, batteries and electrolysis [66]. As the word electrochemistry already hints at, this research field examines the overlap between electricity and chemistry.

For some chemical reactions, specifically redox reactions, electrons are transferred from one atom to another [67]. In case the redox reaction is exothermic, i.e. energy is set free during the reaction, combustion occurs, and with that large amounts of heat are set free. To harness this energy as electrical energy instead of heat, the reaction can be physically separated into reduction and oxidation. This separation avoids combustion, the redox reaction is instead controllable, and the electrons are transferred through an external circuit providing electrical energy. One redox reaction, which is highly exothermic, is the reaction between oxygen and hydrogen to form water, which is shown in Equations 2.1, 2.2 and 2.3. The first fuel cells reported on by *Grove* and *Schönbein* are based on these equations [67]. A benefit of this reaction is that the end product is water, which is harmless as an exhaust product.



where ΔG^0 is the Gibbs free energy under standard conditions (298 K, 10^5 Pa) for 1 mol of H_2O .

Another important factor to describe Equation 2.3 is the standard cell potential E_{cell}^0 , which describes the maximum potential that Equation 2.3 can deliver. E_{cell}^0 is related to ΔG^0 by Equation 2.4.

$$\Delta G^0 = -nFE_{cell}^0, \quad (2.4)$$

where n is the number of electrons involved in the reaction, and F is the Faraday constant, which is 96.40 kJ V. The standard cell potential is also defined as the sum of the standard half-cell potentials (see Equation 2.5).

$$E_{cell}^0 = E_O^0 + E_R^0, \quad (2.5)$$

where E_O^0 and E_R^0 are the respective standard half-cell potentials of the oxidation and reduction. E_O^0 or E_R^0 is derived against the standard hydrogen electrode (SHE), which acts as a reference electrode. For the above half reactions 2.1 and 2.2, the standard half potentials are $E_O^0 = 0$ V and $E_R^0 = 1.23$ V, respectively, resulting in $E_{cell}^0 = 1.23$ V [66]. The Nernst equation (see Equation 2.6) can be employed to calculate the cell potential E_{cell} for non-standard conditions [68, 69].

$$E_{cell} = E_{cell}^0 - \frac{RT}{nF} \ln Q, \quad (2.6)$$

where R is the gas constant, T is the absolute temperature, and for the specific case in Equation 2.3, Q is defined according to Equation 2.7.

$$Q = \frac{a_{H_2O}}{a_{H_2} a_{O_2}^{1/2}}, \quad (2.7)$$

where a_x is the activity for species x .

These equations are not only important to understand how fuel cells work, but also the limitations of the system and how a fuel cell is designed.

2.1.2 Introduction to Fuel Cells

To convert chemical energy from a reaction into electricity instead of heat, the redox reaction must be separated physically into reduction and oxidation. In a fuel cell, this is achieved by placing an electrolyte between two electrodes, the cathode, where the reduction takes place, and the anode, where the oxidation takes place. The electrolyte must fulfill two main requirements; it must be highly ion conductive, and at the same time it should be poorly electron conductive. This combination of requirements leads to the ion species travelling through the electrolyte, while the electrons are transferred through an external circuit, and, thus, provide electrical energy [70].

Many different fuel cell types exist today, and their main distinguishing factor is the choice of electrolyte, which then influences other parameters, such as operating temperature, fuel flexibility, and certainly also fuel cell cost. The most wide-spread fuel cell systems nowadays are proton exchange membrane fuel cells (PEMFC) and solid oxide fuel cells (SOFC) [71]. Their names already hint at the difference between these two systems; the electrolyte is a proton exchange membrane in the former case, and in the latter case it is a solid oxide. In PEM fuel cells, the electrolyte conducts protons (H^+) through a membrane, which results in low operating temperatures, ranging between 70 and 110 °C, the need for high purity H_2 fuel, and no CO contamination [70, 72]. Even though low operating temperatures are often desirable, as they allow for fast start-up times, which are deemed necessary for the transportation sector, and they convey a higher sense of security, they also lead to the need for an expensive Pt catalyst. On the other hand, SOFCs have very high operating temperatures, typically between 600 to 850 °C. The high temperature is not only required to achieve satisfactory ion conduction through the electrolyte, but it also negates the need for a Pt catalyst, which can drastically reduce the cost of the fuel cell [19]. Because the conducted species in SOFCs are oxide ions, the demand on the fuel is much less stringent, and, in addition to contaminated H_2 , even hydrocarbons, such as ethanol, methanol and diesel reformat, can be used as a fuel [19]. This has the great benefit that the infrastructure for refueling is already available world-wide, which is not the case for H_2 as a fuel. However, hydrocarbons as a fuel partly negate the green energy argument for SOFCs, because the release of CO_2 is not prevented. Nevertheless, if SOFCs are compared to conventional combustion engines, the levels of CO_2 released is much lower for the SOFC. This is because fuel cells are not limited thermodynamically by the Carnot cycle, thus, their electrical efficiencies are much higher than those of combustion engines [73]. SOFCs outperform most other fuel cell types when it comes to electrical efficiencies, and electrical efficiencies of above 60 % [15] have been reported for SOFCs compared to up to 50 % for PEMFCs [46]. By using the waste heat that is produced during the operation of the fuel cell for the generation of additional electricity using heat engines or heating, the overall efficiency of an SOFC can be increased even more to above 90 % [15, 17, 74, 75]. Especially the market for combined heat and power (CHP) units has expanded drastically in the last few years. This can be found in the ENE-FARM project in Japan, which had installed over 260 000 PEM and SOFC micro-CHP units all across Japan as of 2018 [76, 77]. The benefits of these CHP units are not only low emissions, but also the autonomy of the system. This was for example demonstrated in 2018, when Osaka experienced a typhoon and most households were without power, except for the ones that had previously installed the ENE-FARM systems [78]. Even though the high operating temperatures for SOFCs result in some benefits, they are also the cause of issues that do not arise at lower temperatures, especially material degradation and slow start-up times. The latter is only problematic for some applications, such as car engines, and, therefore, this technology is mostly considered for stationary applications, range-extendors or as auxiliary power units (APU) in trucks or recreational vehicles [70]. However, the high operating temperatures are often the reason for fuel cell failure after long life-times and, thus, must be addressed, and the degradation must be mitigated. In addition to the high cost of a SOFC, the degradation remains the biggest obstacle to overcome before wide-spread commercialization of this technology can

be achieved.

2.1.3 Solid Oxide Fuel Cell

The electrolyte in SOFCs is an oxygen anion conductor, and, thus reduction and oxidation that take place in a SOFC (see Equations 2.8 and 2.9) differ from, for example, a PEMFC (see Equations 2.1 and 2.2). The overall reaction, however, remains the same (see Equation 2.3).



A single fuel cell consists of three different parts, the anode, where oxidation occurs, the cathode, where reduction occurs, and the electrolyte, which separates the electrodes and, thus, the two half reactions from each other. The operating principle of a fuel cell is depicted in Figure 2.1a.

Because the standard cell potential E_{cell}^0 for Equation 2.3 is 1.23 V (see Chapter 2.1.1) and due to further polarization losses, the applied energy output is typically below 1 V [69, 79]. This is too low for any application, therefore, multiple fuel cells are connected in series using interconnects to form a fuel cell stack, as shown in Figure 2.1b. All components, the electrodes, the electrolyte and the interconnect, must fulfill certain requirements. These are discussed in the following, and information on the state-of-the-art materials used today is given. One requirement that all components must comply with is matching thermal expansion coefficients (TEC). If this requirement is not fulfilled, thermal stresses can build up during the heating or cooling that occurs during start-up or shut-down, respectively [69].

Electrolyte The main requirements for an electrolyte were briefly touched upon in Chapter 2.1.2: good ionic conductivity and poor electronic conductivity [81–83]. These two requirements are what prevent combustion from occurring and instead lead to a controllable reaction. The output energy of this reaction can be harnessed as electrical energy. However, in addition, the electrolyte must be stable at high temperatures and in anode and cathode atmospheres. No reaction should occur with the electrodes during operation, and the electrolyte must be dense and non-porous to prevent the cathode and anode gases from mixing [81–83]. The most commonly used materials today are oxides that crystallize in fluorite structure or in perovskite structure and contain oxygen defects that allow for good O^{2-} conductivity [83]. Popular choices for electrolyte materials are yttria-stabilized zirconia (YSZ) for high operating temperatures (above 700 °C) or gadolinia-doped ceria (CGO) for lower temperatures [82, 83]. $LaGaO_3$ is the most prominent candidate for perovskite-based structures. Substitution of this material with Sr and Mg (LSGM) results in higher ionic conductivity than YSZ if no secondary phases are formed [82].

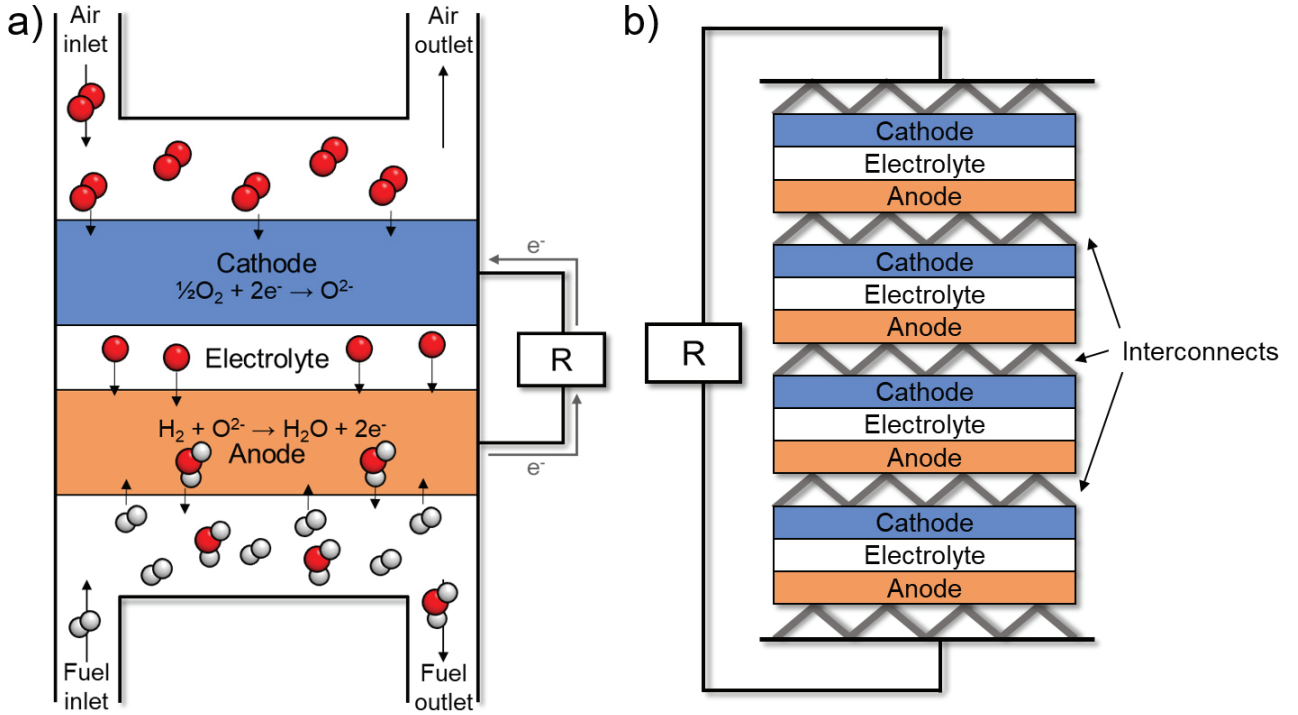


Figure 2.1: Solid oxide fuel cell. a) Operating principle and b) fuel cell stack. Drawing based on [80].

Anode The anode material must be stable at the operating temperatures and within a large range of $p(\text{O}_2)$ pressures. The latter might be counter-intuitive, as the anode experiences mainly low $p(\text{O}_2)$ levels during fuel cell operation. However, high $p(\text{O}_2)$ is often present during the preparation of the anode, and the $p(\text{O}_2)$ levels vary drastically throughout the fuel cell during fuel cell operation, due to increased levels of H_2O towards the fuel outlet [84]. The anode must also be catalytically active towards Equation 2.8. Further requirements can be derived from Equation 2.8: the material must be a good ion and electron conductor, and it must be permeable to H_2 and H_2O to ensure good transport of the reactants and products through the electrode and towards the electrolyte, the external circuit, or the gas outlet. This permeability is achieved through high porosity, which also significantly increases the catalytically active surface area. High ionic and high electronic conductivity are achieved in many practical cases by using composites that contain two materials with either high ionic or high electronic conductivity. These composites lead to the need for a large triple-phase-boundary (TPB) area. Most anode materials today are a mixture between a good electron conductor and the electrolyte material, which is a good ion conductor. This ensures that the TEC of the anode and the electrolyte are very similar [84, 85]. The state-of-the-art anode material today is Ni-YSZ [84].

Cathode The cathode material must fulfill requirements similar to the anode material, with the exception that the cathode must be stable in high $p(\text{O}_2)$ atmospheres. The cathode must also be stable at high temperatures, catalytically active towards the reduction of O_2 (see Equation 2.9), porous to ensure good gas flow, and it must be a good electron

conductor that ideally would be a decent ion conductor. The last requirement is not always fulfilled for cathode materials, and the TPB area is rather small in those cases. An example of this is Sr-doped LaMnO_3 (LSM), which is often used as a cathode material. Sometimes YSZ is added to increase the ionic conductivity of this material. Mixed ionic electronic conductors (MIEC) are preferred especially for intermediate temperature (IT) SOFCs, with $(\text{La,Sr})(\text{Co,Fe})\text{O}_3$ (LSCF) being the most common choice [86, 87].

One important degradation mechanism of fuel cells is Cr poisoning of the cathode, which will be discussed in Chapters 2.2.3 and 2.3.1. This process, even if not yet fully mechanistically understood, affects both LSCF and LSM cathodes, but due to the reduced TPB area in LSM cathodes, the effect is more pronounced in there [73, 85, 86].

Interconnect Requirements for the interconnect material are very similar to those for the electrolyte material, with the main difference being that while the electrolyte must be a good ion conductor but a poor electron conductor, the exact opposite is required of the interconnect. In addition to the high electron and low ionic conduction properties, the interconnect must be stable at the operating temperature and in low and high $p(\text{O}_2)$ atmospheres, and it must be non-permeable to the cathode and the anode gases. Additionally, interconnects should be good thermal conductors and show high chemical stability towards the electrodes [23, 73, 88]. A secondary function of the interconnect, besides electrically connecting the cells, is distributing the gases throughout the entire cell, therefore, the material should be easy to form. The design of gas channels varies drastically among fuel cell manufacturers, with each company trying to minimize the pressure drop, temperature gradients, and gas composition gradients throughout the cell.

Interconnects are primarily made of ceramics, especially perovskites, such as Ca or Sr-doped LaCrO_3 , for operating temperatures above 1000°C . Because perovskites are semiconductors, they require high operating temperatures to reach sufficiently high electronic conductivities. Even though ceramic interconnects are highly stable under fuel cell conditions, they are nowadays rarely used, not only because they are brittle and, thus, not easy to form, but also because they are extremely expensive. Owing to improvements carried out at the electrode and electrolyte levels, the operating temperatures of fuel cells today are much lower and range between 600°C and 850°C . This allows for a completely different material group to be considered as the new standard for interconnect materials: stainless steels [23, 73, 88].

Stainless steels as interconnect material fulfill most requirements that an interconnect must fulfill. They are very good electron and thermal conductors, easy to form, and cheaper than ceramics. Ferritic stainless steels (FSS) have very similar TECs compared to the state-of-the-art materials used as the electrodes and the electrolyte, and therefore, are the main choice as interconnect materials [23, 88, 89]. However, steels degrade under harsh conditions, such as high temperatures or aggressive atmospheres, both of which are present in solid oxide fuel cells, with operating temperatures above 600°C and low $p(\text{O}_2)$ and high $p(\text{O}_2)$. To avoid heavy corrosion, steels are designed to form a slow growing protective oxide on top of the material. The protective oxide for FSSs used as interconnect material is typically the semi-conductor Cr_2O_3 . Even though Cr_2O_3 protects the interconnect from further degradation, it also causes some issues, such as evaporation

of Cr(VI) species or an increase in the resistance of the interconnect [23, 88, 89]. These degradation processes are one of the main factors that limit the life-time of SOFCs. It has also been shown that the interconnect greatly impacts the overall cost of a fuel cell stack, with estimates for the interconnect contribution ranging from 6 % to 45 % of the fuel cell manufacturing stack cost [24–26]. Therefore, improvements in the interconnect, i.e. increased life-time at decreased cost, could advance the commercialization of SOFCs.

The present thesis contributes knowledge about the degradation mechanism related to the interconnect and then devises strategies for how to mitigate the degradation at low cost. Some general background on corrosion is given in the following chapter to understand these corrosion-related issues better, before delving into how corrosion affects interconnects.

2.2 Oxidation Theory

Under ambient conditions, the thermodynamically favorable form for most metals is the oxidized form, which is usually achieved through the reaction of the metal M with air, according to Equation 2.10 [27].



Even though the stable form is typically the oxidized metal, at ambient temperature and in dry atmospheres the kinetics of Equation 2.10 are sluggish. This changes drastically at elevated temperatures, and the oxidized form of the metal becomes the more prevalent form. High temperature corrosion is detrimental to many applications for various reasons and results in material loss [27]. Therefore, protective measures must be applied.

To understand the research conducted within the scope of this work, some basic theory on high temperature corrosion, how diffusion impacts oxide growth or material failure, and why evaporation phenomena occur is given in the following.

2.2.1 Thermodynamics

To understand if the reactant or the product of a reaction is in the thermodynamically stable form, the Gibbs free energy of the reaction ΔG can be calculated according to Equation 2.11, which is derived from the second law of thermodynamics under the assumption of constant pressure and temperature.

$$\Delta G = \Delta H - T\Delta S, \quad (2.11)$$

where ΔH is the change in enthalpy, and ΔS is the change in the entropy of the reaction. The reaction is in equilibrium when ΔG equals 0. For $\Delta G < 0$ the reaction occurs spontaneously, and the products are thermodynamically favorable, while the opposite is true for $\Delta G > 0$, and the reaction will not occur spontaneously with the reactants being in the thermodynamically favorable form [27, 68, 90]. Per mole oxygen ΔG of Equation

2.10 can be calculated according to Equation 2.12.

$$\Delta G = \Delta G^0 + RT \ln \left(\frac{a_{M_\alpha O_\beta}^{2/\beta}}{a_M^{2\alpha/\beta} a_{O_2}} \right), \quad (2.12)$$

where ΔG^0 is the change in the Gibbs free energy under standard conditions for Equation 2.10, R is the gas constant, T is the absolute temperature, and a_i is the thermodynamic activity of species i . The thermodynamic activity can be assumed to be 1 for pure solids¹. The thermodynamic activity of gases is approximately equal to the gases' partial pressure, i.e. $a_{O_2} = p_{O_2}$. Thus, for the equilibrium state $\Delta G = 0$, Equation 2.12 can be rewritten as Equation 2.13.

$$\Delta G^0 = RT \ln p_{O_2}. \quad (2.13)$$

Equation 2.13 defines the two factors that determine whether the metal oxide or the metal is thermodynamically stable: the temperature T and the oxygen partial pressure p_{O_2} . The latter factor is also named dissociation pressure, as it describes the oxygen pressure below which the metal oxide dissociates into the metal and oxygen [27].

Equation 2.13 can be used to classify different metals and their behavior according to temperature and partial pressure. For this purpose, Equation 2.13 for different metals is plotted against temperature and partial pressures of the oxidizing medium. This plot is called the Ellingham/Richardson diagram. The Ellingham/Richardson diagram is visualized in Figure 2.2 for selected oxides and their corresponding reduced form. The slope of each line corresponds to ΔS in Equation 2.11. More stable oxides possess a lower ΔG value, and all oxides become less thermodynamically stable with increasing temperatures. [27, 91]. Cr_2O_3 plays a vital role in the present work, as this oxide was formed on the investigated materials and is therefore highlighted in Figure 2.2.

2.2.2 Kinetics

Even though the oxidized form of most metals is thermodynamically more stable than the pure metal, the oxidized form might still not be the prevalent one, due to the kinetics of Equation 2.10. Kinetics also define how quickly an oxide scale grows and are, thus, an indicator for when a material fails, due to material loss, mechanical failure, or other application-dependent issues. Therefore, the kinetics of oxide scale growth are an important factor in determining the life-time of metals and steels.

Oxide Formation and Growth Reactions like in Equation 2.10 are multiple step processes in reality, and these multiple steps must be understood, and the rate-determining step must be identified to understand the kinetics of a reaction. Three steps occur in the oxidation of a pure metal, as depicted in Figure 2.3. In the first step, oxygen is adsorbed onto the metal surface, and in the second step, metal oxide nucleation occurs. Both

¹Alloys are not pure solids, therefore, their activity a_M depends on the concentration of the metal M in the alloy.

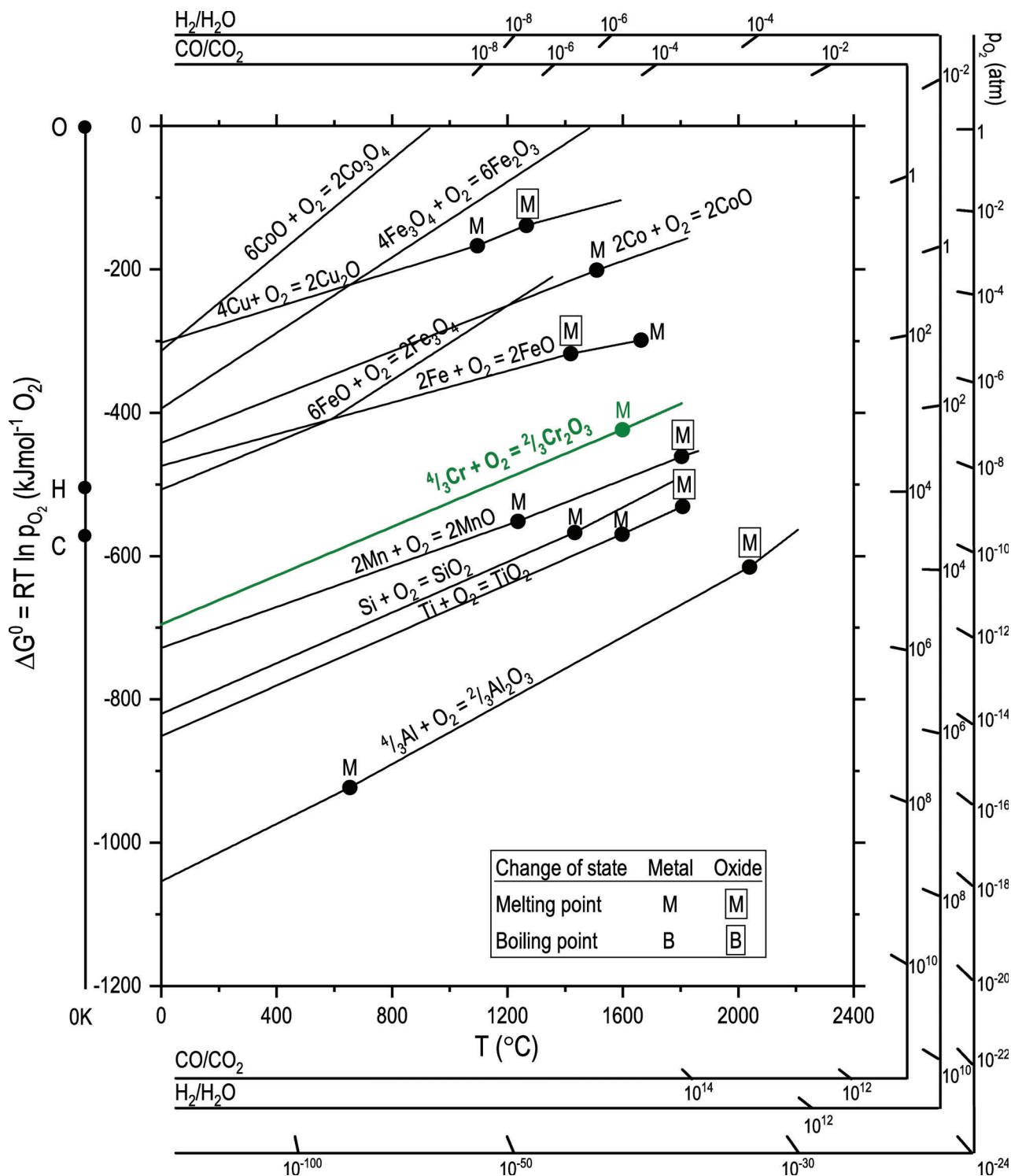


Figure 2.2: Ellingham/Richardson diagram for selected oxides relevant for the present thesis. This diagram was reconstructed from [27, 92]. The $\text{CoO}/\text{Co}_3\text{O}_4$ equilibrium was calculated using [93].

of these processes are highly dependent on surface conditions, e.g. surface preparation, defects at the surface of the material, and gas or metal impurities. Once a continuous oxide scale has formed on the metal, the third step, scale growth occurs. This process is subsequently dependent on the solid-state diffusion of electrons and ions through the oxide scale. Porous oxides can form on certain metals and under certain atmospheric conditions. In these cases, the oxide does not act as a solid-state diffusion barrier [27, 90]. The first two steps of oxide formation are typically rapid at high temperatures, and the third step is commonly the rate-determining step. Slow-growing oxide scales can form a protective layer on the metal, preventing direct contact between the gas and the pure metal. These oxides are called protective oxides, and several properties of an oxide lead to it being slow-growing, such as low porosity, high density, high stoichiometry, and the low diffusivity of oxygen anions and metal cations [27, 90].

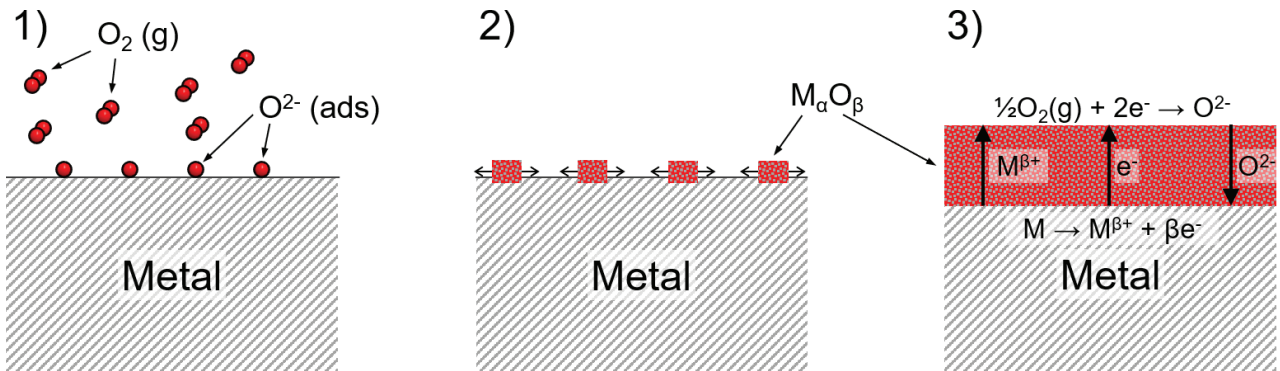


Figure 2.3: *Schematic drawing of the process of oxide growth on a metal substrate according to [27]. The three main steps are: 1) Oxygen adsorption, 2) oxide nucleation, and 3) continuous oxide scale growth.*

Rate Equations To analyze oxide scale growth and its progress, three different aspects can be observed throughout high temperature exposure of a metal: metal consumption, oxygen uptake, or oxide scale growth. From an experimental point of view, the latter option is preferable, as they can be easily followed by measuring the weight gain of the metal. However, under certain conditions, e.g. evaporation phenomena or the formation of different oxide scales, the mass gain might be falsified, and factors besides weight must be analyzed [90]. Rate equations are employed to describe scale growth mathematically. The three most basic rate equations that apply for metal oxide growth are described below, and their behavior is visualized in Figure 2.4. The true behavior of oxide scale growth in reality is often a mixture between different rate equations, but even simple rate equations can still serve as a rough classification for different oxides and can help identify protective oxides [90].

Linear Rate Equation The growth of highly porous oxide scales or very thin oxide scales often follows the linear rate equation shown below (see Equations 2.14).

$$x = k_l t + C, \quad (2.14)$$

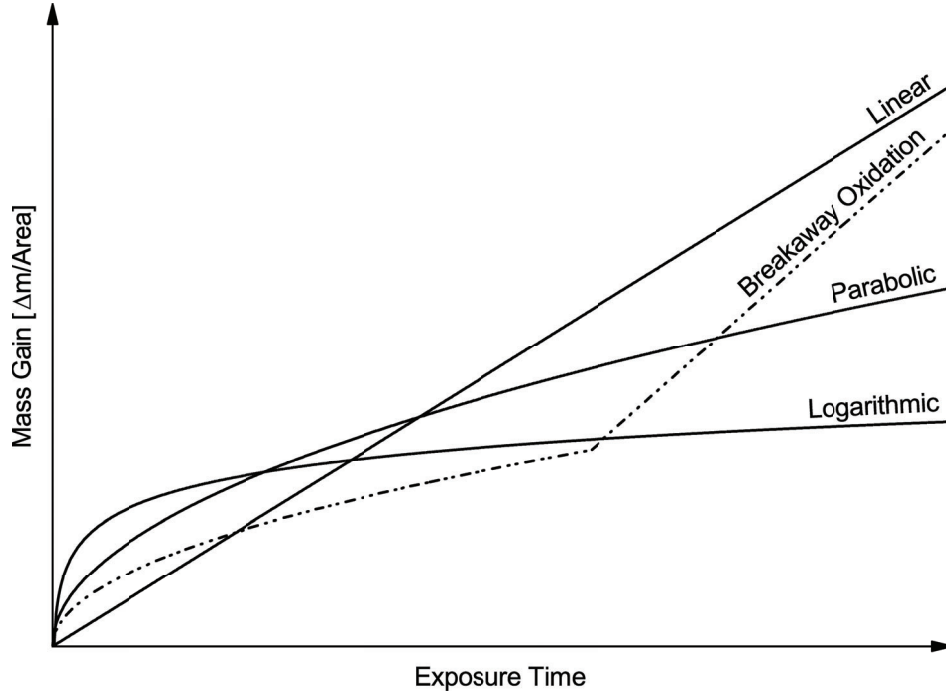


Figure 2.4: Typical growth behavior of metal oxides [27].

where x is the oxide thickness and can be substituted with the mass gain Δm , k_l is the linear rate constant, and C is the integration constant. As can be seen in Figure 2.4, this oxide scale growth behavior increases linearly, and no decrease in mass gain over time is found. This growth behavior is independent of gas or metal consumption, and the rate-determining step is either a surface-related process that occurs during the oxygen adsorption (step one) and oxide nucleation (step two) of the oxide scale growth (see Figure 2.3), or a phase boundary process [27].

Logarithmic Rate Equations Logarithmic scale growth occurs primarily at rather low temperatures, between 300 °C and 400 °C and for thin oxide scales up to 50 nm. Two different mathematical functions can be used to describe logarithmic oxide scale growth: the direct logarithmic function (see Equation 2.15) or the inverse logarithmic function (see Equation 2.16) [94, 95].

$$\text{Direct Logarithmic : } x = k_{\log} \log(t + t_0) + A, \quad (2.15)$$

$$\text{Inverse Logarithmic : } \frac{1}{x} = B - k_{il} \log t, \quad (2.16)$$

where x is the oxide thickness or the mass gain Δm , k_{\log} is the logarithmic, and k_{il} is the inverse logarithmic rate constant, t is the exposure time, and A and B are the integration constants. Figure 2.4 depicts the direct logarithmic rate law; a steep mass gain occurs during the initial stages of oxidation but then drastically decreases to nearly negligible values [95]. The mechanism, including the rate-determining step for these rate laws, has

not yet been agreed upon, especially because the parameters that influence this rate law are complicated to verify independently. Suggestions for the rate-determining step include: the transport of ions or electrons through the oxide scale along an electric field, chemisorption, or cavity formation [90, 91, 95].

Parabolic Rate Equations Numerous metals comply with the parabolic rate equations at high temperatures [27, 95]. This rate law is given by Equation 2.17.

$$x^2 = k_p t + C, \tag{2.17}$$

where x is the oxide thickness or the mass gain Δm , k_p is the parabolic rate constant, t is the exposure time, and C is the integration constant. One limitation of this rate law is that it does not cover the initial stages of oxidation, as it is based on a pre-existing oxide scale. For parabolically growing oxide scales, the rate-determining step is solid-state diffusion through the oxide scale [27, 95]. Parabolically growing oxides are often considered the ideal case to form protective oxide scales, because the increasing thickness of the oxide scale over time results in longer diffusion paths and, thus, leads to a decrease in the oxide scale growth rate at longer exposure times [27].

In 1933, Carl Wagner postulated an oxidation theory stating that oxide scale growth occurs only via lattice diffusion [96–98]. Within this theory, Wagner made the following assumptions about oxide scales [90, 91, 98]:

- The formed oxide scale is dense, continuous, and well-adherent.
- The rate-determining step is solid-state diffusion of ions, electrons, or electron holes through the scale.
- The processes occurring at the phase boundaries are rapid enough that they do not influence the reaction rate.
- Both interfaces, the metal-oxide and the oxide-gas, are in a thermodynamic equilibrium state.
- The stoichiometry of the oxide is consistent throughout the scale.
- The scale is in thermodynamic equilibrium throughout the scale.
- The thickness of the scale is much greater than the maximum length where charge effects occur.
- Oxygen solubility is negligible in the metal.

Some of these assumptions have been questioned and even Carl Wagner himself has proposed some alterations [99]. Nevertheless, the model delivers sufficiently good results and is still used today.

2.2.3 Oxide Properties

The parabolic growth of oxide scales is dependent on ion mobility through the scale, and this is influenced by certain properties of the oxide. Therefore, the properties that affect oxide scale growth will be discussed next. First, oxide defects, which are the main contributor to ion mobility through the oxide scale and determine if an oxide scale is inward or outward growing, are addressed. Then the volume expansion that occurs during the oxidation of a metal will be analyzed according to *Pilling* and *Bedworth* [100], and lastly, the decrease in oxide thickness due to the vaporization of oxide species will be discussed.

Oxide Defects The growth mechanism of oxides is highly dependent on the solid-state diffusion of metal cations, oxygen anions or electrons, and electron holes through the oxide scale. Defects must be present for solid-state diffusion to occur. Even highly stoichiometric oxides, such as Al_2O_3 and Cr_2O_3 , have defects, because below a certain concentration, the presence of defects decreases the free energy of the crystal [101]. Defects are classified into three different classes: point defects, line defects, and plane defects, with the latter two occurring, for example, along grain boundary interfaces or stacking faults [27]. Point defects can be divided into two groups: stoichiometric defects, also called intrinsic defects, and non-stoichiometric defects, also called extrinsic defects. Doping of an oxide with another element leads to extrinsic defects. The two most common intrinsic defects in oxides are Schottky and Frenkel defects, which are visualized in Figure 2.5 with the most basic crystal structure, the rock-salt structure of NaCl or AgCl, respectively. For Schottky defects, a cation vacancy is charge-compensated by an anion vacancy, whereas for Frenkel defects, the charge compensation of either a cation or an anion vacancy is achieved by an interstitial cation or anion, respectively. The Frenkel defect is visualized with a cation defect in Figure 2.5 [101].

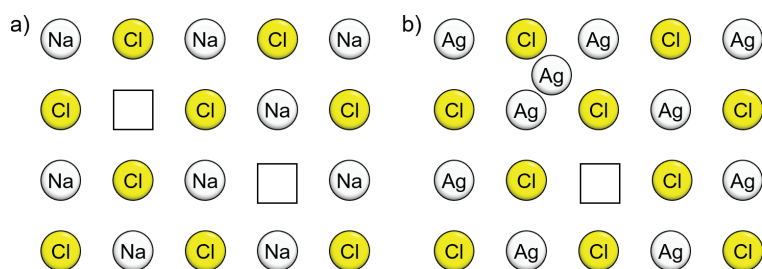


Figure 2.5: Schematic drawing of Schottky (a) and Frenkel (b) point defects common to stoichiometric oxides. The ratio of the ion diameter in this drawing is not representative of the actual ratio [101].

The diffusion of ions or electrons through the oxide occurs along defects. The diffusion rate varies depending on the defect that is involved and the exposure temperature. Lattice diffusion, for example, takes place utilizing point defects and is the slowest form of diffusion. In contrast, diffusion along grain boundaries is much faster and is, thus, termed short-circuit diffusion [27]. The high activation energy for lattice diffusion and the low activation energy for grain boundary diffusion results in the latter being more dominant

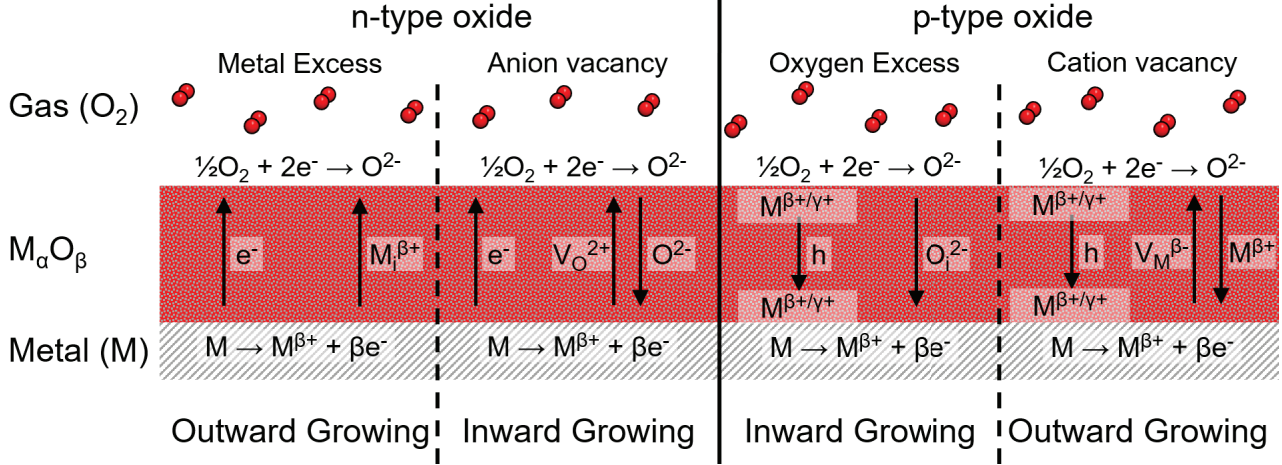


Figure 2.6: *Schematic drawing of defect structure in oxides and what they implicate for the growth direction of an oxide. Reconstructed from [103], with $\gamma = \beta + 1$, i = interstitial, V_x = vacancy at lattice site x .*

at lower temperatures and the former being more dominant at higher temperatures [27, 102]. This temperature dependence is even further amplified by the coarsening of the grains that occurs at higher temperatures [91]. These general statements are not only valid for diffusion within an oxide but also for diffusion within the steel used, which is important for alloys [102].

The defects that exist in a thermally grown oxide also influence the growth direction of the oxide (see Figure 2.6). Depending on their predominant defect, the oxides can be classified similar to semi-conductors into n- and p-type oxides; the former conduct electrons along the conduction band, and the latter conduct electron holes along the valence band.

Pilling-Bedworth Ratio The requirements a protective oxide must fulfill were stated in Chapter 2.2.2. For a quick assessment if an oxide is protective or non-protective N. B. Pilling and R. E. Bedworth formulated Equation 2.18 in 1923 [100]. They suggested that the protectiveness of an oxide can be evaluated according to what stresses buildup in the oxide, and this can easily be calculated by the ratio between the volume of the metal oxide V_{oxide} and the metal V_{metal} itself [27, 90].

$$PBR = \frac{V_{\text{oxide}}}{V_{\text{metal}}}, \quad (2.18)$$

where a Pilling-Bedworth ratio (PBR) < 1 results in tensile stresses and possibly pores in the oxide, and a PBR > 1 results in compressive stresses in the oxide. Due to the nature of these stresses, Pilling and Bedworth have suggested that oxides with a PBR just above 1 are protective and lead to continuous oxide coverage, because compressive stresses inhibit crack and pore formation. However, Pilling and Bedworth expect buckling of the oxide for oxides with PBR values that are much greater than one; this would gradually result in oxide spallation. In general, the PBR approach assumes that the oxide is inward growing, and oxygen inward diffusion is the predominant diffusion. Many

exceptions to this assumption are currently known, and the classification of an oxide into protectiveness or non-protectiveness is not straightforward [27, 90]. Even though the original interpretation of the PBR is outdated, it is still broadly used today to estimate the volume expansion that occurs when a metal is fully oxidized. Some important PBR values that are used in this thesis are given in Table 2.1.

Table 2.1: PBR values for some metal-oxygen systems. Unless otherwise stated, the values were taken from [90].

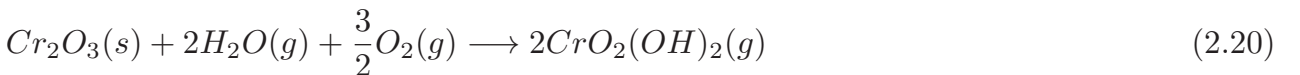
Oxide	PBR
Al_2O_3	1.28
Cu_2O	1.64
FeO (on $\alpha\text{-Fe}$)	1.68
CoO	1.86
Co_3O_4	1.98 [104]
Cr_2O_3	2.07
Fe_3O_4 (on $\alpha\text{-Fe}$)	2.10
Fe_2O_3 (on $\alpha\text{-Fe}$)	2.14

Volatilization of Oxides Most metal oxides are stable at high temperatures, however, there are also some metal oxides that form volatile oxide species at higher temperatures or in certain environments. Examples that are often discussed in relation to high temperature corrosion are Cr oxides, Mn oxides, and W oxides. Because of the high activation energy of the evaporation process, this process becomes more important at high temperatures [27]. Cr-evaporation is a major topic in the present thesis, therefore, the evaporation process will be explained using Cr evaporation.

A very common protective oxide scale for alloys is Cr_2O_3 , which is considered stable in a dry atmosphere and at low oxygen partial pressures. However, this oxide can form many different gaseous Cr(VI)-species, and the vaporization process of gaseous CrO_3 (see Equation 2.19) becomes relevant for the life-time of an alloy above 1 000 °C and at $p(\text{O}_2) \geq 1 \text{ atm}$.



Besides leading to the release of carcinogenic Cr(VI) species, this evaporation also results in material consumption, Cr depletion in alloys or poisoning of the cathode in SOFCs (see Chapter 2.3.1). What is even more problematic, however, is that under humid conditions, a different gaseous Cr(VI)-species, $\text{CrO}_2(\text{OH})_2$, forms at much lower temperatures according to Equation 2.20.



Even small amounts of water vapor favor the formation of $\text{CrO}_2(\text{OH})_2$ over the formation

of CrO_3 [28–30]. The difference in temperature dependence for both gaseous Cr(VI) -species is also mirrored by the difference in activation energy for the formation of CrO_3 versus $\text{CrO}_2(\text{OH})_2$. The latter has a comparatively low activation energy, resulting in reduced temperature dependence [28].

Cr evaporation leads to an increase in the consumption of Cr. The scale growth rate is altered due to the competing processes of continuous parabolic Cr_2O_3 growth and continuous Cr evaporation. In theory, most systems will eventually reach a steady-state scale thickness, which is expressed as weight loss in a thermogravimetric analysis [27]. This behavior is called paralinear oxidation.

2.2.4 Oxidation of Alloys

Today very few pure metals are used commercially, and instead, alloys are the material of choice, for example steels, which are Fe containing alloys. Different steels have different alloying elements, which are often added to achieve certain properties. Stainless steels comprise one common steel class. They contain at least 10 wt% Cr and are often the material of choice for high temperature applications. The oxides formed during the oxidation of alloys usually do not have the same composition as the alloy, and the oxide composition and structure might change during oxidation. Oxides can be formed on the surface of the material and internally in the alloy. Some basic information is given in the following on how alloys oxidize and what general rules might influence oxidation. For more detailed information, the reader is referred to [27].

Two elements can oxidize in a simple binary alloy, element A and element B. If both oxides are thermodynamically stable at a given temperature and oxygen partial pressure and the concentration of both alloying elements is high enough, a transient oxide may form on the surface of the alloy in the initial stages of oxidation. In theory, a faster growing oxide (BO) will quickly overgrow a slower growing oxide (AO). However, in practice, if element A is less noble than element B, a displacement reaction (see Equation 2.21) will take place at the scale/metal interface, and concentration gradients throughout the scale and in the metal will occur [27].



Over time, a continuous oxide scale of AO will be formed on the alloy surface, and, if the rate-determining step for the progressing oxidation is solid-state diffusion through the scale, the oxidation will then proceed according to the parabolic rate law. To achieve a continuous AO scale, sufficiently high concentrations of A are needed. If this is not the case, the oxidation of B will instead occur. This can also happen locally, for example the alloy might still have a high concentration (mole fraction: N_A) of alloying element A in its bulk, but a depletion zone below the scale forms because of slow diffusivity of alloying element A (D_A) through the alloy. In that case, the fast-growing oxide BO will form [27].

Another species that has been neglected in the discussion above is oxygen. If oxygen is soluble in the alloy, it can penetrate the alloy and lead to internal oxidation. Therefore, two other factors must be acknowledged: the diffusivity (D_O) and mole fraction (N_O) of oxygen. In very simple terms, external oxidation is favored if Equation 2.22 is fulfilled [27, 105].

$$N_A D_A \gg N_O D_O, \quad (2.22)$$

With these parameters Carl Wagner derived two conditions, one for the initial stages of oxidation and one for the latter stages. These two criteria describe, at what concentration (N_A) the formation of an external oxide scale (AO) occurs (Criterion 1), or at what concentration (N_A) the upkeep of the oxide AO is secured (Criterion 2). These conditions are explained and shown below for a case where Cr is the element that forms the protective oxide scale and is, thus, considered as element A.

The first criterion that Wagner devised, describes above which critical Cr concentration N_{Cr}^{crit1} an external Cr_2O_3 scale is formed and internal oxidation is prevented (see Equation 2.23).

$$N_{Cr}^{crit1} > \left[\frac{\pi g^*}{3} \frac{V_M}{V_{M_x O_y}} \frac{N_O^{(s)} D_O}{\tilde{D}_{Cr}} \right] \frac{1}{2}, \quad (2.23)$$

where g^* is a factor that is set to 0.3 according to [106], V_M and $V_{M_x O_y}$ are the molar volumes of the alloy and the oxide $M_x O_y$, which for Cr_2O_3 on top of Fe-Cr, results in $V_M = 7 \text{ cm}^3 \text{ mol}^{-1}$ and $V_{M_x O_y} = 15 \text{ cm}^3 \text{ mol}^{-1}$, $N_O^{(s)}$ is the oxygen solubility in the alloy, D_O is the oxygen diffusivity in the alloy, and \tilde{D}_{Cr} is the chemical diffusivity of Cr. This criterion (see Equation 2.23) is only valid if no prior oxide scale is present on the alloy [107, 108].

The second criterion by Wagner describes above which critical concentration N_{Cr}^{crit2} the pre-formed external Cr_2O_3 scale is sustained (see Equation 2.24).

$$N_{Cr}^{crit2} > \frac{V_M}{32v} \left(\frac{\pi k_p}{\tilde{D}_{Cr}} \right) \frac{1}{2}, \quad (2.24)$$

where v is a stoichiometric factor, which is 1.5 for Cr_2O_3 , and k_p is the parabolic rate constant. Below the critical Cr concentration, N_{Cr}^{crit2} , Fe will oxidized instead of Cr in the Fe-Cr system. The failure is due to a depletion of Cr below the oxide scale caused either by the depletion of Cr in the entire material, or by local depletion caused by an insufficiently fast Cr diffusivity in the base alloy [107, 109].

Failure to fulfill these Wagnerian criteria results in breakaway corrosion.

Breakaway Oxidation Breakaway corrosion occurs under certain circumstances in alloys, where one of the elements forms a protective oxide scale and another element forms a poorly or non-protective scale. Breakaway oxidation is defined as a sudden change from primarily forming a slow-growing oxide to primarily forming a fast-growing oxide and can be detected by a sudden change in mass gain behavior from a formerly parabolic behavior to a linear behavior (see Figure 2.4) [27, 110].

Breakaway corrosion occurs due to different circumstances, but the two main reasons

are intrinsic chemical failure (InCF) or mechanically induced chemical failure (MICF) [110]. InCF is primarily due to the above discussed depletion of the protective oxide-forming element in the alloy. Material failure and the formation of a non- or less protective fast-growing metal-oxide (e.g. Fe-rich oxide) scale occurs when the Cr content of the alloy, N_{Cr}^{crit2} , falls below a certain threshold (see Equation 2.24) [27, 110].

On the other hand, MICF occurs when the oxide scale reaches a critical thickness and cracks, ruptures, or even detaches partly. This negates the barrier effect the oxide has, and instead the metal and the gas come in direct contact. Depending on other factors, this can either lead to breakaway oxidation or not. No breakaway oxidation will occur if the Cr concentration in the alloy directly beneath the crack fulfills Equation 2.23 [27, 110]. The first criterion of Wagner applies to this example, because no oxide scale is directly present at the crack and instead metal gas contact occurs. Breakaway oxidation will, however, happen, if the Cr concentration N_{Cr}^{crit1} does not fulfill criterion 1 locally (see Equation 2.23) [111].

Outside factors are known to influence the probability that breakaway oxidation will occur. For example, it is generally acknowledged that for Cr_2O_3 -forming alloys, the presence of water vapor in high $p(O_2)$ atmospheres greatly increases the risk of breakaway oxidation due to Cr evaporation (see Chapter 2.2.3) [112–114].

2.3 Oxidation of Ferritic Stainless-Steel Interconnects

The function and requirements for interconnects was discussed in Chapter 2.1.3. Nowadays, the state-of-the-art interconnect material for solid oxide fuel cells is stainless steel. The following chapter explains which steels and which coatings are the most suitable for interconnect applications in terms of corrosion resistance, electrical conductivity, and cost, amongst others. Degradation mechanisms that affect the interconnect are also explained, such as Cr evaporation and the dual atmosphere effect.

2.3.1 Material Selection

Steels that are used at high temperatures often rely on the formation of a protective oxide to slow down the continuous oxidation of the material, which can eventually lead to material failure. Most steels either form an Al_2O_3 or a Cr_2O_3 scale. Even though the former is highly stable at high temperatures and has a lower k_p value than the latter, meaning that Al_2O_3 grows slower than Cr_2O_3 , it is unsuitable for interconnect applications. This is because the main function of an interconnect is to electrically connect individual fuel cells to each other, and Al_2O_3 is an insulator, while Cr_2O_3 is a semiconductor [27]. Therefore, stainless steels, which are defined as steels with a minimum Cr content of about 10 wt%, are the material of choice for interconnects.

Different types exist within the stainless-steel class, and these are classified according to their crystalline structure. The two most common types are ferritic and austenitic stainless steels, which crystallize in a body-centered cubic (BCC) or face-centered cubic (FCC) structure, respectively. Due to their respective TEC, which is between $11.5 \cdot 10^{-6} K^{-1}$ and $14 \cdot 10^{-6} K^{-1}$ for ferrites [88] and between $18 \cdot 10^{-6} K^{-1}$ and $20 \cdot 10^{-6} K^{-1}$ for austenites [88], ferritic stainless steel is the favored choice, because the TEC matches better

with other fuel cell components ($\text{TEC}_{\text{SOFC}} = 10.5 - 12.5 \cdot 10^{-6} \text{ K}^{-1}$ [88]). Consequently, interconnect research is mainly focused on ferritic stainless steels (FSS) and specifically FSSs with a Cr content between 16 and 26 wt% [89]. The oxidation of FSS suggested for use as interconnect material typically obeys the parabolic rate law, and the FSS Cr_2O_3 scale grows with a k_p value between 10^{-14} and $10^{-13} \text{ g}^2 \text{ cm}^{-4}$ in air at 800°C [115–119].

Even though FSSs are the material of choice for interconnects for various reasons, such as ease of formability, TEC coefficients that match other cell parts, high electrical and thermal conductivity, and lower cost than ceramic interconnects, some issues that impact the life-time and cost of a fuel cell remain. The most obvious issue stems from the fact that humid conditions and high $p(\text{O}_2)$ partial pressures are present on the air side of the interconnect, and the interconnect contains high amounts of Cr. Cr evaporation (see Chapter 2.2.3) plays a huge role in the degradation of a fuel cell due to these conditions. Besides continuous Cr consumption, which can lead to Cr depletion, the much more problematic effect of hexavalent gaseous Cr species in a fuel cell is that it blocks the TPB in the cathode and leads to cathode poisoning and, thus, fuel cell degradation [120, 121]. It has been previously suggested that roughly one third of the entire degradation of a fuel cell can be attributed to Cr evaporation [120, 122]. Another degradation mechanism that is related to Cr is the continuously increasing electrical resistance of the interconnect caused by the continuously growing semiconductive Cr_2O_3 scale. These are the two most common degradation mechanisms for interconnects, and their mitigation is most widely researched today, however, other degradation mechanisms exist; one of them is the dual atmosphere to which the interconnect is exposed, and which can lead to breakaway oxidation.

These two main degradation mechanisms can often be mitigated to a certain extent by adding or omitting certain alloying elements to or from the interconnect material. These specifically designed alloys often perform well in Cr retention and have slow oxidation rates, however, they are more costly than commercially available materials [123]. A very common specifically designed interconnect material is Crofer 22 APU, which has a Cr content above 22 wt%. The major drawback of these specifically designed materials is their high cost. Interconnects can contribute up to 46 % of the overall material cost of a fuel cell [124] and, therefore, any reduction in material cost has the potential to decrease the overall cost of the fuel cell drastically. One common approach to reducing interconnect cost is to switch to more widely used steels, such as AISI 441 or AISI 430, which have between 16 and 20 wt% Cr [31, 49, 125–133]. Figure 2.7 shows that the reduction in manufacturing cost with a shift from Crofer 22 APU to AISI 441 is present even for large volume productions. Therefore, the material cost savings can be relayed to the overall fuel cell cost at all production volumes [26]. The drawback of these cheaper materials is that, due to their low Cr content, they are probably more suited for IT-SOFCs with an operating temperature below or equal to 700°C [49].

Minor alloying elements can result in promising properties for the interconnect material. Below important alloying elements that alter the properties of the interconnect in either direction, towards more degradation of the interconnect or less, are briefly discussed.

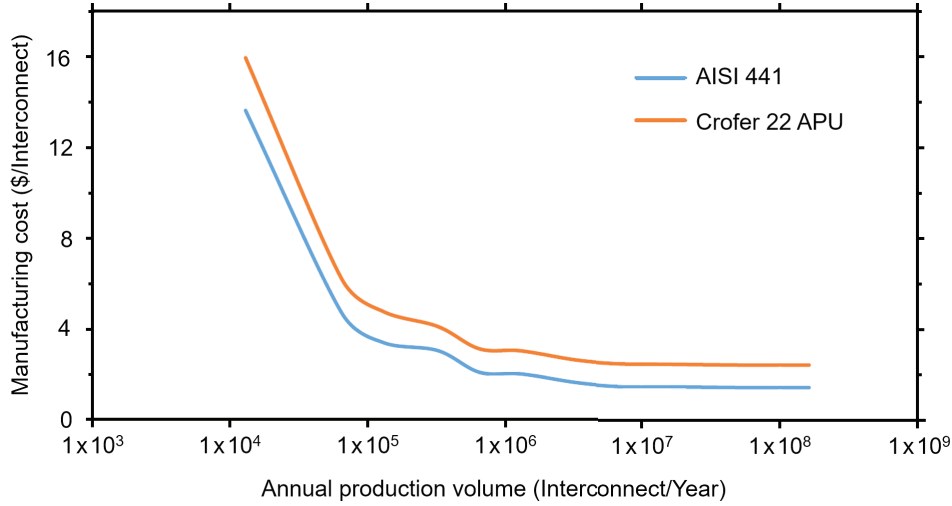


Figure 2.7: *Manufacturing cost for interconnects depending on material used and production volume. The following parameters were chosen for this study: 15 μm MCO coating, which was applied using PVD. Reconstructed from [26].*

Alloying Elements

Manganese Mn is present in most materials considered for interconnect applications as a minor alloying element in concentrations of around 0.3 to 0.5 wt% [49, 123]. The advantage of Mn in an alloy is a reduction in Cr evaporation due to the formation of a $(\text{Cr}, \text{Mn})_3\text{O}_4$ spinel as a cap layer on top of the continuously growing Cr_2O_3 scale. It has been shown that this alloy addition reduces the Cr evaporation rate by a factor of 2 to 3 [123, 134]. This reduction is not sufficient to prevent Cr poisoning of the cathode, and, instead, coatings are typically used to achieve good Cr retention rates (see Chapter 2.3.2).

Si and Nb, Mo, or W Si is present in all steels, and it is a byproduct of steel production, where it is used as a de-oxidant [135]. The presence of Si in alloys used for interconnect applications can be detrimental to the SOFC. This is because the Si oxidizes at high temperatures and forms SiO_2 . If the Si content in the material is high enough, a continuous SiO_2 layer can form. A continuous sub-scale SiO_2 layer leads to two issues due to the properties of SiO_2 . First, because SiO_2 is an electrical insulator, the resistance of the interconnect could be drastically increased [136–138] and, second, it was previously suggested that the spallation that occurs during thermal cycling of, for example, uncoated AISI 441 is due to the extremely small TEC of SiO_2 compared to the TEC of the alloy [80, 138]. Two different approaches are common to avoid both these effects. Si is avoided to a large extent in more expensive FSSs and especially steels that are specifically designed for use as interconnects, such as Crofer 22 APU, by using a costly vacuum induction melting process. An alternative approach is to bind the Si instead of preventing its presence and thus avoid the formation of SiO_2 . This is achieved by adding other alloying elements, such as Nb or Mo, which form Laves precipitates with Si in the steel. An added benefit of this approach is that Laves phases increase the hardness and the creep strength of the steel [136, 137].

Reactive Elements Reactive elements (RE) are often added to Cr_2O_3 -forming alloys used in high temperature applications. REs are known to improve oxidation resistance by increasing scale adhesion and, to a certain extent, decreasing the oxide scale growth rate. Ce, La, Hf, and Y are most commonly used, and they are added at very low concentrations, because high concentrations can lead to an adverse effect [35, 36, 90, 139–142].

The mechanism for how REs improve corrosion behavior is still being debated. One theory is that the improvement of scale adhesion is brought about by improved interfacial chemical bonding. One aspect of this interfacial chemical bonding is the "sulfur effect", which suggests that the alloying element sulfur segregates to the metal/scale interface, which might harm scale adhesion. This segregation is proposed to be hindered to a certain degree by REs, leading to an increase in scale adhesion [27, 143, 144]. However, the validity of this theory is uncertain, because oxide spallation is also found under conditions that eliminate sulfur segregation [143, 144].

The most prominent theory is that the REs change the growth direction of the oxide. It is suggested that the non-doped Cr_2O_3 scale grows predominantly outward through metal-outward diffusion, but simultaneously also some inward growth through oxygen inward diffusion occurs. Doping an oxide with REs is thought to inhibit metal-outward diffusion by segregating the REs in the oxide grain boundaries. The oxide then becomes predominantly inward growing, because the smaller oxygen anions are not affected by the presence of the REs in the grain boundaries. The growth process now occurs predominantly by oxygen inward diffusion [144–148]. This change in growth direction would not only explain the improved scale adhesion, but also the decreased oxide scale growth rate. However, *Falk-Windisch* et al. [149] have shown that this theory might not be fully applicable. Those authors could not find proof that the oxide was predominantly inward growing if a Ce coating was applied, and instead the growth mechanism still seemed to be predominantly outward growing, with only a minor increase in inward growth.

2.3.2 Protective Coatings

Besides adding alloying elements to the steel, coatings have been an effective measure to hinder Cr evaporation or decelerate Cr_2O_3 scale growth. Especially for cheap commercially available FSSs, such as AISI 441, coatings have been proven indispensable. Coatings are the norm for interconnects today.

Some important requirements must be fulfilled to be considered as a usable interconnect coating, such as good adhesion, good compatibility with other fuel cell parts, high electrical conductivity, and of course the coating must be effective in mitigating Cr evaporation, decreasing the oxide scale growth rate, or limiting other degradation processes of the interconnect. One very common coating material was discussed in Chapter 2.3.1; reactive elements that increase oxide scale adhesion and have been shown to decrease oxidation rate. Instead of adding them directly to the alloy, which would result in expensive and specifically designed steels, the same effect can be achieved by adding a thin reactive element coating to the steel surface [35, 36]. If an RE coating is applied, similar rules for adding REs to the alloy apply; the coating thickness should not be too thick, otherwise an adverse effect could occur [142].

Spinel or perovskite oxide coatings are often suggested to increase the Cr retention of interconnects. While perovskite oxides coatings have high electrical conductivities and are compatible with other fuel cell parts, their adhesiveness to steel and their effect on Cr retention rates are often poor. Additionally, thick perovskite coatings must be applied to achieve a reduction in oxidation rate [44, 150–152]. In contrast, spinel coatings excel at Cr retention and are, therefore, considered state-of-the-art. The $(\text{Mn},\text{Co})_3\text{O}_4$ (MCO) coating has particularly shown excellent Cr retention rates while also being a decent semi-conductor with sufficiently high electron conductivity at 800 °C (see Table 2.3.3) [33, 34, 153, 154]. Besides applying this coating directly as an oxide via powder-based methods, such as electrophoretic deposition [155], spray coating [156], or screen printing [157], the coating can also be applied via a conversion route [37, 152]. For this route, the steel is coated with a metal, which is oxidized during high temperature exposure. To achieve the MCO coating, the steel is coated solely with Co, which rapidly oxidizes to form Co_3O_4 at high temperatures. The ensuing outward diffusion of Mn from the steel leads to the enrichment of Mn in the Co oxide and, thus, MCO is formed [37, 130, 152, 158]. The last step, the outward diffusion of Mn, is temperature dependent. While high Mn content in the outer spinel layer has been found at 850 °C, up to 26 cation% after 3000 h of exposure [37] at 650 °C, *Falk-Windisch* et al. [159] have measured only 2 to 3 cation% in the outer Co spinel under the same conditions and for the same material, Co-coated Sanergy HT. Instead, a Mn- and Cr-rich scale was found at the steel oxide interface. Even though the poor diffusivity resulted in less conductive spinels at 650 °C than at 850 °C (see Table 2.2), *Falk-Windisch* et al. [159] have shown excellent results, with area specific resistance values around 4 to 8 $m\Omega\text{ cm}^2$ and improved Cr-retention rates 650 °C than at higher temperatures. Conversion coatings have some benefits over powder-based methods: high density and thin coatings are much easier to achieve with the former. An additional advantage of this coating technique is that it can be applied in a cost-effective large-scale roll-to-roll PVD process instead of batch coating. This manufacturing process is possible because of the self-healing capabilities of the Co coating, which will be discussed below.

Today the state-of-the-art coating is considered to be a 640 nm thick Co coating on top of a 10 nm thick Ce coating [56, 57]. This coating combines the advantages of the Co coating, good Cr retention rates, with the advantages of a RE coating, improved scale adherence, and lower oxidation rates.

Self-healing Capabilities of Coatings As mentioned, large-scale roll-to-roll processes can be used to coat interconnects cost effectively. The drawback of this manufacturing process is that to use a roll-to-roll process the deformation of the interconnect into its final form must be done after the material is coated (see Figure 2.8). This stamping step is known to introduce cracks into the coating, which could negatively impact coating effectiveness. However, *Falk-Windisch* et al. [47, 48] have previously shown that even though these cracks exist, neither the Cr evaporation rates nor the mass gains are affected by the stamping. This finding means that deformed Ce/Co-coated FSS performed, within limitations, just as well as undeformed Ce/Co-coated FSS at 850 °C. The authors suggest that $(\text{Cr},\text{Mn})_3\text{O}_4$ first formed as a top layer inside the cracks, and the ensuing lateral diffusion of Co from non-cracked regions resulted in a uniform $(\text{Co},\text{Mn})_3\text{O}_4$ scale after 168 h of exposure [47, 48].

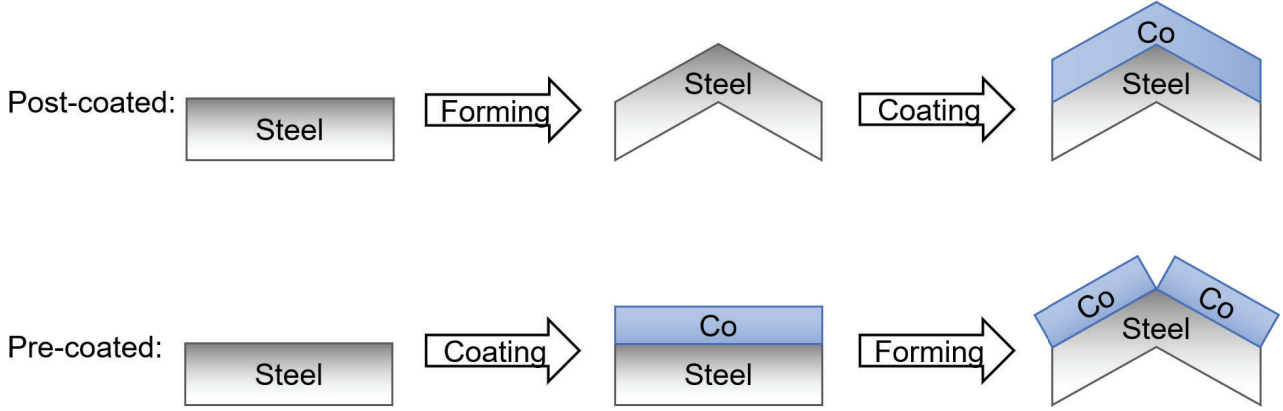


Figure 2.8: Schematic drawing of the step-wise preparation of post- or pre-coated steel. Reconstructed from [47].

2.3.3 Electrical Conductivity of Oxide Scales

An important requirement for an interconnect is high electrical conductivity. The FSS itself is highly conductive, however, the oxides that form on the interconnect, either due to continuous oxidation or due to the coating, can greatly decrease the electrical conductivity of the interconnect as a whole, which leads to ohmic losses of the fuel cell [160]. Therefore, it is important to understand how the electrical conductivity of oxides is defined, and how this degradation can be evaluated experimentally using area specific resistance (ASR).

The electrical conductivity (σ_{total}) of an oxide scale is defined as the sum of the ionic and electronic charge carriers, according to Equation 2.25,

$$\sigma_{total} = \sigma_{ionic} + \sigma_{electronic} = \sigma_{total} (t_{ionic} + t_{electronic}), \quad (2.25)$$

where σ_{ionic} and $\sigma_{electronic}$ are the respective conductivities, which are defined by Equations 2.26 and 2.27 with the transport numbers t_{ionic} or $t_{electronic}$ [27].

$$\sigma_{ionic} = \sigma_{total} \cdot t_{ionic}, \quad (2.26)$$

$$\sigma_{electronic} = \sigma_{total} \cdot t_{electronic}. \quad (2.27)$$

The electronic conductivity $\sigma_{electronic}$ is defined according to Equation 2.28 as the sum of the conductivity of the electrons σ_e and electron holes σ_h .

$$\sigma_{electronic} = \sigma_e + \sigma_h = e(nv_e + pv_h), \quad (2.28)$$

where n and p are the concentrations of electrons and electron holes, respectively, and v_e and v_h are the corresponding electron and electron hole mobilities [27]. Similarly, the total ionic conductivity σ_{ionic} is defined as the sum of the anion and cation conductivities [27].

The temperature dependency of the overall conductivity is defined by the mobility and the concentration terms. The mobility of electrons typically decreases at higher

temperatures, while the concentration term, which is composed of the concentration of electrons and electron holes, increases. The concentration term increases to such an extent that electronic conductivity $\sigma_{\text{electronic}}$ is mainly dependent on this term at high temperatures in oxides. In contrast, the electronic conductivity in metals is mainly dependent on the mobility term at high temperatures. This leads to the fact that the conductivity of metal oxides increases with higher temperatures, while it decreases for metals. Oxides for which this is true, for example Cr_2O_3 and Co_3O_4 , are classified as semiconductors [27]. To describe the temperature dependency of the electrical conductivity of an oxide scale, the Arrhenius equation (see Equation 2.29) is used.

$$\sigma = \sigma_0 \cdot \exp\left(\frac{-E_a}{R \cdot T}\right), \quad (2.29)$$

where σ_0 is a pre-exponential factor, R is the ideal gas constant, T is the absolute temperature, and E_a is the activation energy.

Oxide scales for interconnects are typically discussed in terms of their resistance R , instead of their conductivity (see Equation 2.30).

$$R = \frac{1}{\sigma} \cdot \frac{L}{A}, \quad (2.30)$$

where σ is the conductivity, L is the oxide thickness, and A is the measured area. To achieve an area-independent value, the area specific resistance (ASR) is used to assess and compare the conductivities of exposed interconnects (see Equation 2.31).

$$ASR = A \cdot R_{\text{tot}}. \quad (2.31)$$

Conductivity of Cr_2O_3 Cr_2O_3 is an intrinsic semiconductor above 1000°C , however, it is an extrinsic semiconductor below 1000°C and, therefore, reliant on dopants or local stoichiometric defects [161, 162]. Reported conductivity values for Cr_2O_3 mirror this change in behavior. While the literature is unanimous when it comes to the conductivity of Cr_2O_3 above 1000°C , a very different situation is present below this temperature [162]. For example, at 800°C and at 1 atm, the reported conductivity varies between 0.001 and 0.05 S cm^{-1} and the reported activation energy for the conductivity varies between 0.25 and 0.82 eV for measurements conducted below 850°C [72, 80, 161, 163–168]. If Cr_2O_3 acts as an extrinsic semiconductor, which is the case below 1000°C it is also a dual semiconductor. This means that it can display n-type or p-type semiconducting behavior, depending on the temperature and the oxygen activity [169, 170]. Oxygen activity has even been known to influence the oxide morphology throughout the scale, leading to a dual morphology with a columnar external oxide and an equiaxial internal oxide as shown by *Latu-Romain* et al. [169–171] at 900°C and $p(\text{O}_2) = 10^{-12} \text{ atm}$. This duality is also mirrored in the semiconducting behavior and results in an internal n-type semiconductor, and an external p-type or n-type semiconductor. The latter is dependent on the $p(\text{O}_2)$ [169–173]. In addition to parameters such as temperature and oxygen partial pressure, dopants also play a role in the semiconducting behavior of Cr_2O_3 . The thermally grown Cr_2O_3 scales on FSSs are often doped with elements from the underlying steel, such as Fe,

Mn, or Ti. The doping effect is known to increase the conductivity of Cr_2O_3 [174, 175].

Conductivity of Spinel Spinel oxide coatings are considered indispensable as interconnect coatings, therefore, their conductivity is relevant for interconnect research. Electron conductivity in spinels is assumed to occur via a hopping mechanism between octahedral sites, meaning that good conductivity is achieved if these sites are occupied by elements that can accommodate different valence states [153]. This assumption is exemplified by Cr^{3+} containing spinels: This cation has an extremely strong preference for octahedral site occupation, and its oxidation state rarely deviates from Cr^{3+} , therefore, its low conductivity is easily explained [153, 176]. *Petric* et al. [153] have published an extensive overview of the conductivity of many different spinels (see Table 2.2) with the aim to evaluate which spinel coatings are better suited for interconnect applications. The best results have been found for Co,Mn- or Cu,Mn-containing spinels, and they are the most researched coatings for interconnects today [46, 57].

A spinel that often forms during the oxidation of an FSS is the Mn,Cr-containing spinel. As mentioned previously, Cr-containing spinels often suffer from poor electron conductivity, which explains the low conductivity of $\text{Mn}_{1.2}\text{Cr}_{1.8}\text{O}_4$. Similarly, low conductivity values have been reported for MnCr_2O_4 ($\sigma_{800^\circ\text{C}} = 0.004 \text{ S cm}^{-1}$ [177] or $\sigma_{800^\circ\text{C}} = 0.03 \text{ S cm}^{-1}$ [178]) and $\text{Mn}_{1.7}\text{Cr}_{1.3}\text{O}_4$ ($\sigma_{800^\circ\text{C}} = 0.14 \text{ S cm}^{-1}$ [177]). Especially for interconnects that rely on the formation of the $(\text{Cr,Mn})_3\text{O}_4$ spinel to mitigate Cr evaporation, this low conductivity can lead to ohmic degradation of the fuel cell. Therefore, coatings that avoid the formation of these poorly conductive spinels are preferred as interconnect coatings.

Table 2.2: Conductivity values for different transition metal spinel oxides measured at 800°C unless stated otherwise. Data taken from [153]. The conductivities are given in S cm^{-1} . The most relevant spinel conductivities for this work are marked in bold.

	Mg	Mn	Co	Ni	Cu	Zn
Al	MgAl_2O_4 $\sigma = 10^{-6}$	MnAl_2O_4 $\sigma = 10^{-3}$	CoAl_2O_4 $\sigma = 10^{-5}$	NiAl_2O_4 $\sigma = 10^{-4}$	CuAl_2O_4 $\sigma = 0.05$	ZnAl_2O_4 $\sigma = 10^{-6}$
Cr	MgCr_2O_4 $\sigma = 0.02$	$\text{Mn}_{1.2}\text{Cr}_{1.8}\text{O}_4$ $\sigma = 0.02$	CoCr_2O_4 $\sigma = 7.4$	NiCr_2O_4 $\sigma = 0.73$	CuCr_2O_4 $\sigma = 0.40$	ZnCr_2O_4 $\sigma = 0.01$
Mn	MgMn_2O_4 $\sigma = 0.97$	Mn_3O_4 $\sigma = 0.10$	CoMn_2O_4 $\sigma = 6.4$	NiMn_2O_4 $\sigma = 1.4$	$\text{Cu}_{1.3}\text{Mn}_{1.7}\text{O}_4$ $\sigma = 225 (750^\circ\text{C})$	ZnMn_2O_4
Fe	MgFe_2O_4 $\sigma = 0.08$	MnFe_2O_4 $\sigma = 8.0$	CoFe_2O_4 $\sigma = 0.93$	NiFe_2O_4 $\sigma = 0.26$	CuFe_2O_4 $\sigma = 9.1$	ZnFe_2O_4 $\sigma = 0.07$
Co		MnCo_2O_4 $\sigma = 60$	Co_3O_4 $\sigma = 6.7$			

2.3.4 The Dual Atmosphere Effect

Research focusing on interconnect materials is often carried out under simplified conditions compared to the conditions present in a solid oxide fuel cell. This is done so that certain corrosion phenomena, such as Cr evaporation or oxide scale growth, can be analyzed mechanistically without the influence of other parameters. Even though this simplification is often beneficial for examining certain phenomenon, it neglects the real conditions to which the interconnect is exposed, which could have a detrimental effect on the oxidation of the interconnect.

One very common simplification is that instead of exposing interconnect materials to a dual atmosphere, which they are subjected to in the fuel cell, they are exposed to a single atmosphere, i.e. either a fuel atmosphere or an air atmosphere. Therefore, the effect of dual atmosphere on the oxidation behavior of interconnects has been investigated for operating temperatures around or above 800 °C [179–183]. The results of those investigations were contradictory. Some researchers reported an increase in oxidation on the air-facing side in dual atmosphere (see Figure 2.9) compared to only air atmosphere, while others found no indication of a detrimental effect in dual atmosphere.

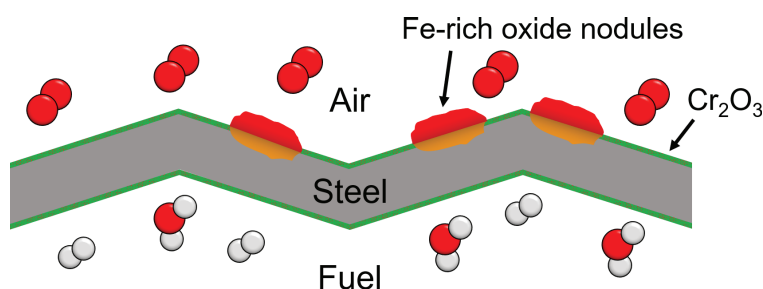


Figure 2.9: Dual atmosphere to which interconnects are exposed in a SOFC.

At 800 °C, the most detrimental effect of the dual atmosphere was reported for AISI 441 by *Yang et al.* [179] and *Gannon et al.* [182]. Those authors found the formation of iron-rich oxide scales on the air-facing surface of AISI 441 that was exposed to dual atmosphere. However, the more commonly reported finding in dual atmosphere at this temperature was an Fe-enriched spinel oxide top layer that formed on the air-facing side [180]. This Fe-enriched oxide layer had also formed on Crofer 22 APU in *Yang et al.*'s [179] study. Other authors found that a thicker oxide scale had formed on the air-facing side of samples exposed to dual atmosphere than samples exposed to single atmosphere [181, 183]. In contrast, no significant dual atmosphere effect has been reported by *Kurokawa et al.* [184] and *Alnegren et al.* [32] at temperatures above or equal to 800 °C. Except for the study by *Alnegren et al.* [32], all these studies have focused on high temperatures around or above 800 °C, although the trend nowadays is towards lower operating temperatures for SOFCs.

The lowering of the operating temperature of SOFCs could allow for the use of cheaper materials, because lower degradation rates would ensue. However, some studies have shown the opposite in simulated anode or cathode atmospheres. For a simulated anode atmosphere, for example, *Young et al.* [185] have reported higher oxidation rates between 500 °C and 600 °C than between 650 °C and 800 °C. Iron-rich oxides were the main surface

oxide at the lower temperatures, while Cr_2O_3 covered the surface of the material at higher temperatures. Similar results with the formation of Fe-rich oxides on FSS and austenitic stainless steels have been found by *Niewolak et al.* [49] at 600 °C in an anode-simulated atmosphere. In a steam atmosphere ($\text{Ar} + 50\% \text{H}_2\text{O}$) between 550 °C and 650 °C, *Zurek et al.* [186] have reported different oxidation behaviors for different FSSs with varying Cr contents between 9 and 12 wt% Cr. Those authors showed that some steels oxidized faster at higher temperatures than at the lower temperatures, and others showed the opposite behavior. *Sanchez et al.* [187] have reported that AISI 430 forms a Cr_2O_3 scale at 800 °C, but a $(\text{Fe,Cr})_2\text{O}_3$ scale at 650 °C. The reason for this anomalous corrosion behavior that both *Sanchez et al.* [187] and *Zurek et al.* [186] have suggested is that Cr diffusivity in the bulk decreases at lower temperatures and, thus, is not sufficiently high to maintain a Cr_2O_3 scale, which leads to the oxidation of Fe instead.

This anomalous temperature dependency motivated *Alnegren et al.* [31, 32] to re-examine the dual atmosphere effect at temperatures lower than 800 °C. Those authors have found that the dual atmosphere effect showed inverse temperature behavior. In *Alnegren et al.*'s [31, 32] study severe breakaway oxidation was observed on AISI 441 exposed to dual atmosphere at 600 °C, however, at 700 and 800 °C a protective oxide scale had covered AISI 441. In contrast, AISI 441 remained protective at all investigated temperatures in air-only atmosphere. Similar to the explanation that *Zurek et al.* [186] and *Sanchez et al.* [187] give on why anomalous corrosion behavior is observed in single atmosphere, *Alnegren et al.* have also suggested that the improved corrosion resistance found in dual atmosphere at higher temperatures is caused by an increase in Cr diffusivity in the bulk alloy, which then counteracts the dual atmosphere effect.

The mechanism for the dual atmosphere effect remains unclear. What is agreed upon is that hydrogen is the culprit, but it is not known where the hydrogen attacks. The role of hydrogen is corroborated by its high diffusivity through ferritic stainless steels, which is extremely fast, and rates in the mm h^{-1} range can be expected at 800 °C [184, 188, 189]. It is important to understand when breakaway oxidation occurs to understand what hydrogen could alter. The two Wagnerian criteria, $N_{\text{Cr}}^{\text{crit}1}$ (see Equation 2.23) and $N_{\text{Cr}}^{\text{crit}2}$ (see Equation 2.24), can be used for this purpose. The criteria describe below which critical Cr concentration internal oxidation (Criterion 1) or breakaway oxidation (Criterion 2) occurs. The parameters, which could be influenced by hydrogen, are the oxygen permeability $N_{\text{O}}^{(s)D_{\text{O}}}$, the Cr diffusion \tilde{D}_{Cr} , and the parabolic rate constant k_p . Different researchers have proposed or excluded different theories on what hydrogen affects. Some of these theories are discussed below.

One theory is that hydrogen influences oxygen permeability $N_{\text{O}}^{(s)D_{\text{O}}}$ (see Equation 2.23). This would lead to an increase in oxygen inward diffusion and an increase in the formation of an internal oxide, tying up the Cr and leading to Cr deficiency. This theory has been suggested and favored by *Essuman et al.* [112, 190] and *Holcomb et al.* [191], and *Bredvei Skilbred et al.* [180] have also discussed this theory.

According to *Alnegren et al.* [32] it is improbable that Cr evaporation is impacted by hydrogen, because those authors found that the dual atmosphere effect was present in dry atmosphere at 600 °C to a similar extent to that found in humid atmosphere for AISI 441. Many others have suggested that k_p is affected by hydrogen, but that hydrogen alters oxide scale growth instead of oxide evaporation. For example, *Yang et al.* [179, 192]

believe that cation diffusivity is enhanced in the oxide scale by the presence of hydrogen. According to them, this enhancement is due to the formation of hydroxides in the oxide scale. Based on the assumption that Cr_2O_3 is a p-type oxide [161] the hydroxides would be charge-balanced by Cr vacancies in the oxide. Cr vacancies would result in accelerated cation diffusion through the scale, and therefore, accelerated oxide scale growth. This acceleration would lead to an increase of the critical Cr concentration, $N_{\text{Cr}}^{\text{crit}2}$. *Yang et al.* [179, 192] argue that this is in agreement with earlier studies by *Tveeten et al.* [193], who have shown that the presence of hydrogen in Cr_2O_3 greatly enhances the Cr cation diffusivity in the oxide. Another theory that has been proposed by *Bredvei Skilbred et al.* [180] and also affects k_p is that the presence of hydrogen could form steam inside the oxide scales, which at high pressures could lead to pore formation and, thus, faster scale growth and an increase in oxygen inward diffusion. However, *Alnegren et al.* [32] did not find a difference in the protective oxide scale thickness for samples exposed to dual or single atmosphere indicating that k_p is not affected by hydrogen.

Other ideas that are not directly related to the Wagnerian criteria have also been proposed. For example, *Rufner et al.* [181] have suggested that the $p(\text{O}_2)$ could be locally altered by hydrogen on the air-facing side of the interconnect, but they also agree with the aforementioned theory by *Yang et al.* [179, 192].

There is to date an abundance of theories as to how hydrogen affects the oxidation of FSS, but there currently is no non-refutable proof for any of these theories. More research is needed to understand the dual atmosphere effect and develop mitigation strategies against it.

Materials and Methods

3.1 Materials

Two different steel grades were studied in the present thesis, Crofer 22 APU and AISI 441. The grain size of all materials used were determined by Dr. Kerem O. Gunduz using the standard E112 from ASTM [194]. Only one batch was used for Crofer 22 APU, and its composition and grain size are given in Table 3.1. For AISI 441 several different batches in different thickness were used, and their compositions and grain sizes are given in Table 3.2. The differences among the batches were minimal and were, therefore, not expected to influence the degradation properties of AISI 441 and are primarily given for the sake of completeness.

Table 3.1: Material composition of ferritic stainless steel Crofer 22 APU (EN 1.4760) in weight%.

	Fe	Cr	Mn	Si	Ti	C	S	Al	Cu	P	La
Crofer 22 APU											
Batch 173288											
Paper I	Bal.	22.92	0.38	0.01	0.06	0.004	<0.002	0.01	0.01	0.005	0.09
Thickness: 0.3 mm											
Grain Size: 22 μm											

All materials were cleaned ultrasonically in acetone and ethanol prior to exposure. The exact sample geometry and the exposure conditions for all experiments that were conducted within the scope of this work are depicted in Table 3.3. Coatings were all applied by Sandvik Materials Technology (SMT) using a proprietary physical vapor deposition (PVD) technique. If samples were ground or polished, SiC grinding paper with grit P1200 or a diamond polishing suspension with grain size $1/4 \mu\text{m}$ was used as the final finish. Further details as to why certain exposure conditions were chosen and how exposures and Cr evaporation measurements were conducted are given below and in the following chapters.

For experiments carried out within the scope of Paper I, a pre-oxidation step was implemented prior to PVD coating (see Table 3.3).

Table 3.2: Material composition of all studied AISI 441 (EN 1.4509) batches in weight%. The abbreviation ST stands for the study on surface treatments, which has not yet been published. ^{*1}Unless stated otherwise, this batch was used in 0.2 mm thickness.

	Fe	Cr	Mn	Si	Ti	Nb	Ni	C	S	N
AISI 441										
Batch A (64534)										
Paper II/IV/V/VI/ST	Bal.	17.56	0.35	0.59	0.17	0.39	0.26	0.014	0.001	0.017
Thickness: 0.2 mm & 0.3 mm ^{*1}										
Grain Size: 29 μm										
AISI 441										
Batch B (64467)										
Paper II	Bal.	17.61	0.28	0.59	0.153	0.39	0.00	0.017	0.001	0.012
Thickness: 0.2 mm										
Grain Size: 28 μm										
AISI 441										
Batch C (64313)										
Paper III/V	Bal.	17.74	0.30	0.55	0.15	0.37	0.19	0.015	0.002	-
Thickness: 0.2 mm										
Grain Size: 29 μm										
AISI 441										
Batch D (63960)										
Paper III	Bal.	17.83	0.26	0.55	0.14	0.48	0.13	0.012	0.002	0.016
Thickness: 0.2 mm										
Grain Size: 16 μm										
AISI 441										
Batch E (63960)										
Paper VI	Bal.	17.75	0.28	0.42	0.13	0.38	0.21	0.018	0.001	0.015
Thickness: 1 mm										
Grain Size: 20 μm										

3.2 Exposures

Exposure conditions for all experiments conducted within the scope of this thesis are given in Table 3.3. With the exception of Paper I and Paper II, for which all relevant exposure conditions are given in Table 3.3 and Chapter 3.2.1, further information on the exposure conditions are given in the following. For exposures where no heating rate is specified, no heating or cooling ramp was applied, and instead samples were directly inserted into the furnace at the exposure temperature and removed the same way. After exposure, all samples were analyzed using different analytical techniques, which will be described in Chapter 3.3.

Two different furnace types were used for exposures: tube furnaces or box furnaces (see Figure 3.1). Both furnace types have advantages and disadvantages and were, thus, chosen for specific experiments. The atmosphere including flow rates, humidity, and the exact temperature is easily controllable for exposures in a tube furnace (see Figure 3.1a), however, the throughput of this furnace is limited, because the hot zone is only a few

Table 3.3: Experimental matrix for all conducted experiments included in the present work. ^{*1}Definition of Cr evaporation: Tube furnace exposure with high air flow (3 % H₂O/air, 6 000 sml min⁻¹); ^{*2}Biaxial deformation by 15% was carried out by SMT, which resulted in a reduced sample thickness (0.17 mm); ^{*3}For deformed samples, additional short-term exposures were conducted for 71 h at 750 °C and for 111 h at 650 °C; ^{*4}Samples were exposed by SMT; ^{*5}Material thickness: 0.3 mm; ^{*6}Ground or polished on one side, no side, or both sides; ^{*7}Samples were ground to different thicknesses (0.1, 0.2, 0.5, and 0.7 mm); ^{*8}Material thickness: 0.2 mm for as-received and 0.3 mm for the ground or polished samples.

Material Paper	Coating Inner Outer	Geometry	Sample modification	Exposure conditions
Crofer 22 APU Paper I	Pre-oxidation 3 min 800 °C air	After Pre-ox 600 nm Co 1 500 nm Co 3 000 nm Co	15 x 15 mm as-received	500 h 600 °C tube furnace stagnant air
AISI 441 Batch A Paper II	uncoated	15 x 15 mm	as-received	500 h 650 °C/750 °C/850 °C Cr evaporation ^{*1}
AISI 441 Batch B Paper II	10 nm Ce	640 nm Co	15 x 15 mm as-received OR deformed ^{*2}	500 h ^{*3} 650 °C/750 °C/850 °C Cr evaporation ^{*1}
AISI 441 Batch C Paper III	uncoated	30 x 20 mm	as-received	1 000 h 800 °C Cr evaporation ^{*1}
AISI 441 Batch C & D Paper III	10 nm Ce	640 nm Co	30 x 40 mm as-received	up to 37 000 h ^{*4} 800 °C box furnace ^{*4} OR Cr evaporation ^{*1}
AISI 441 Batch A Paper IV	uncoated Pre-oxidation in air at 800 °C for 0, OR 20 min	Circular ∅ = 21 mm	as-received	336 h 500 to 800 °C dual atmosphere
AISI 441 Batch C Paper V	uncoated Pre-oxidation in air at 800 °C for 0, 11, 45, 180, OR 280 min	Circular ∅ = 21 mm	as-received	500 - 1 000 h 600 °C dual atmosphere
AISI 441 Batch A ^{*5} Paper V	uncoated Pre-oxidation in air at 800 °C for 180 min	Circular ∅ = 21 mm	ground OR polished ^{*6}	500 h 600 °C dual atmosphere
AISI 441 Batch A Paper VI	uncoated Pre-oxidation in air at 800 °C for 20 min	Circular ∅ = 21 mm	as-received	336 h 600 °C dual atmosphere
AISI 441 Batch E Paper VI	uncoated Pre-oxidation in air at 800 °C for 20 min	Circular ∅ = 21 mm	ground ^{*7}	336 h 600 °C dual atmosphere
AISI 441 Batch A ^{*8} Paper ST	uncoated No pre-oxidation	Circular ∅ = 21 mm	as-received OR ground OR polished	336 h 600 °C dual atmosphere

centimeters long (furnace-dependent). On the other hand, box furnaces (see Figure 3.1b) have a much larger throughput, but the other parameters, such as exact temperature and atmosphere, can vary inside the furnace, and gas flows can usually not be set. Because of these advantages and disadvantages, tube furnaces were used for most exposures and were particularly indispensable for Cr evaporation measurements (see Chapter 3.2.1), but box furnaces were used for the long-term exposures carried out by SMT within the scope of Paper III.

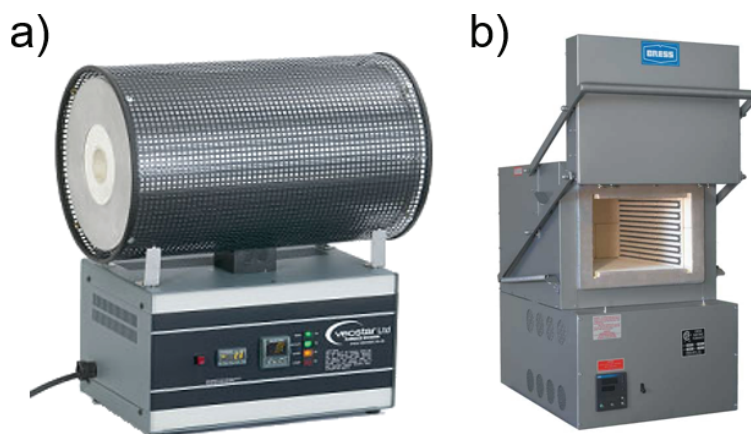
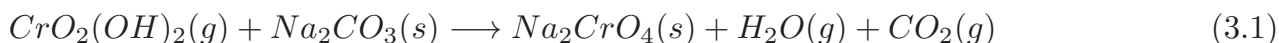


Figure 3.1: *Different furnaces used for the exposures. a) Tube furnace used for short-term exposures and Cr evaporation measurements, b) Box furnace used for long-term exposures performed by AB Sandvik Materials Technology.*

3.2.1 Cr Evaporation Measurements

The quantification of evaporating Cr species is important, because Cr evaporation is a major issue for SOFCs (see Chapters 2.2.3 and 2.3.1). Therefore, Cr evaporation measurements were carried out within the scope of this work.

Froitzheim et al. [195] have described a denuder technique that allows for the in-situ determination of Cr evaporation during an exposure. This technique is based on Reaction 3.1, and the experimental setup is shown in Figure 3.2. The flow restrictor serves to obtain a more uniform flow pattern and avoid backflow. As an additional improvement to the method, a wash bottle was added at the end of the denuder tube (marked with * in Figure 3.2). This ensured that all Na_2CrO_4 was caught.



The denuders and wash bottles were exchanged regularly throughout the exposure. Both were rinsed with de-ionized water, and the concentration of the Na_2CrO_4 solution was determined using ultraviolet-visible (UV-VIS) spectrophotometry (see Chapter 3.3.1). The total amount of evaporated hexavalent Cr species was determined from this.

Cr evaporation measurements were carried out inside tube furnaces. For optimum conditions, laboratory air with a high flow rate of $6\,000\text{ sml min}^{-1}$ was chosen to ensure kinetically controlled, and, thus, flow-independent, Cr evaporation [195]. 3 % water vapor

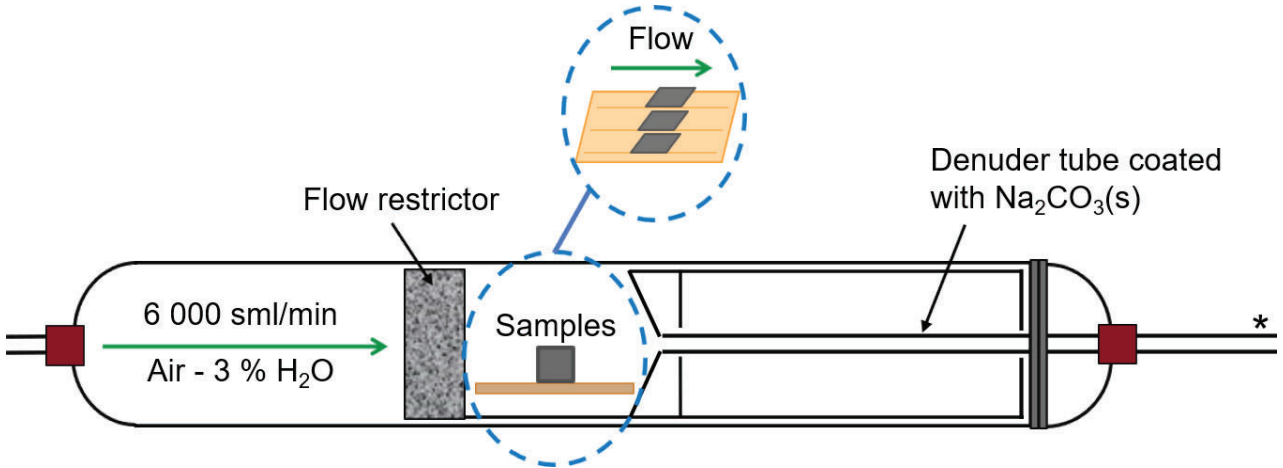


Figure 3.2: *Experimental setup for tube furnace exposures and Cr evaporation measurements based on Froitzheim et al. [195].*

was added to the air to represent worst case fuel cell operation. Humidification was achieved by passing the gas through heated water (30 °C) and, subsequently, cooling the humidified gas to 24.4 °C, which corresponds to a humidity of 3 %. The humidity was verified using a Michell Instruments Optidew Vision™ chilled mirror humidity sensor. Unless stated otherwise, three square samples (1.5 cm x 1.5 cm) for each Cr evaporation measurement were placed into the furnace according to Figure 3.2, resulting in a total surface area of 13.5 cm² excluding the edges.

3.2.2 Long-Term Exposures

Long-term exposures ($\geq 3\,000$ h) were carried out in box furnaces by SMT within the scope of Paper III. The samples, which were rectangular (3 x 4 cm), were exposed discontinuously, and the mass change was recorded regularly. Two different batches were exposed. Samples were taken out for further analysis after 7 000 h, 23 000 h, 35 000 h, and 37 000 h (see Figure 3.3). For all further steps, the samples had to be cut because the experimental setups were optimized for smaller samples. This was carried out using a low-speed saw to minimize the effect of the cutting process on the oxide scales. The samples used for Cr evaporation measurements had an overall surface area of 12 cm² excluding the edges, which is similar to the normal surface area of 13.5 cm² (see Chapter 3.2.1).

For reference, Cr evaporation measurements were conducted on unexposed uncoated and unexposed Ce/Co-coated AISI 441 for 1 000 h. The area specific resistance (ASR) was also recorded for these isothermally exposed samples and, additionally, for Ce/Co-coated AISI 441, which was exposed isothermally for 3 000 h.

3.2.3 Dual Atmosphere Exposures

A custom-made sample holder was available for dual atmosphere exposures (see Figure 3.4). The design of this holder was based on work carried out at Montana State University. Further details on the dimensions of the sample holder can be found in [181, 182, 191]. It was made of 253 MA steel, which is an austenitic stainless steel with approximately

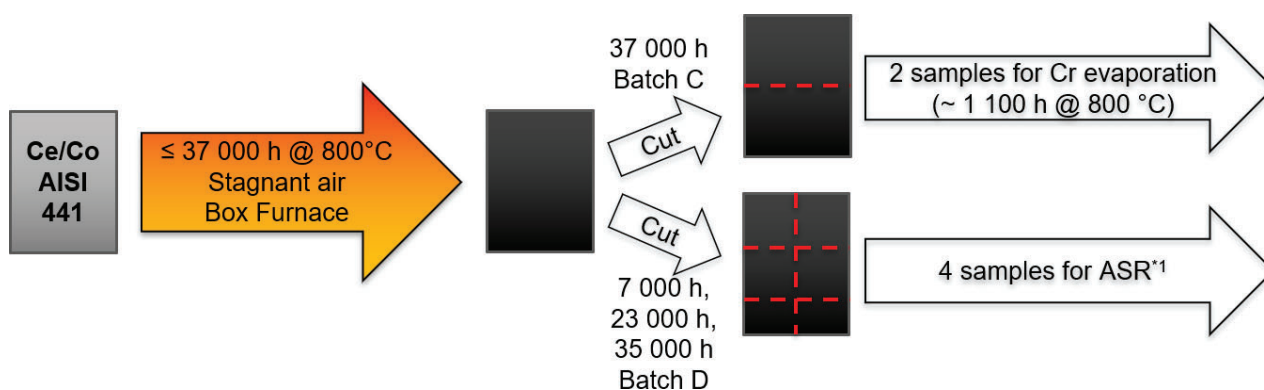


Figure 3.3: Analysis schematic for long-term exposed (≥ 7000 h) Ce/Co-coated AISI 441. The samples were cut down using a low-speed saw. ^{*1}One sample for each exposure time was chosen for subsequent SEM/EDX analysis and a BIB cross-section was prepared.

21 wt% Cr and 11 wt% Ni in addition to other alloying elements. Six samples could be exposed simultaneously, either all could be exposed to dual atmosphere, or three to single atmosphere, and three to dual atmosphere (see Figure 3.4). Humidification was achieved in the same way as for the Cr evaporation measurements, by passing gas through heated water and, consequently, cooling the gas to 24.4 °C. In this work, the heating and cooling ramp for all dual atmosphere exposures was set to 1 °C min⁻¹.

A pre-oxidation step was implemented before dual atmosphere exposure for most samples. This was carried out at 800 °C with a low humid air flow, 280 sml min⁻¹ air - 3 % H₂O. These parameters were chosen for different reasons; the temperature is close to what often occurs during the sintering process of the fuel cell, while the low flow and humidity were used to achieve a well-defined and easy to reproduce atmosphere that was not reliant on outside weather conditions. The pre-oxidation times varied from sample to sample and are stated in Table 3.3 and below. No heating rate was employed for the pre-oxidation step.

Photographs were taken of the air-facing side of the samples after exposure, or in some cases during exposure if the exposure had been interrupted. Electron microscopy, elemental dispersive x-ray spectroscopy, and ion beam milling were conducted after dismantling the samples for further analysis of the corrosion products and oxide morphology.

Temperature Study - Paper IV For the temperature study, single and dual atmosphere exposures were carried out simultaneously on either non-pre-oxidized or pre-oxidized AISI 441. The chosen exposure temperatures (see Table 3.3) were 500 °C, 550 °C, 600 °C, 650 °C, 700 °C, and 800 °C, and the furnace was calibrated using an external thermocouple to the exact temperature with the sample holder, but without the samples, before starting the exposure. This calibration was verified after the exposure had started and the final exposure temperature had been reached. The exposure was carried out for 336 h, but after 168 h a planned interruption was implemented to document the progress of oxidation.

Pre-oxidation Study - Paper V The effect of pre-oxidation on the dual atmosphere effect was examined with regard to two different factors: the length of pre-oxidation and

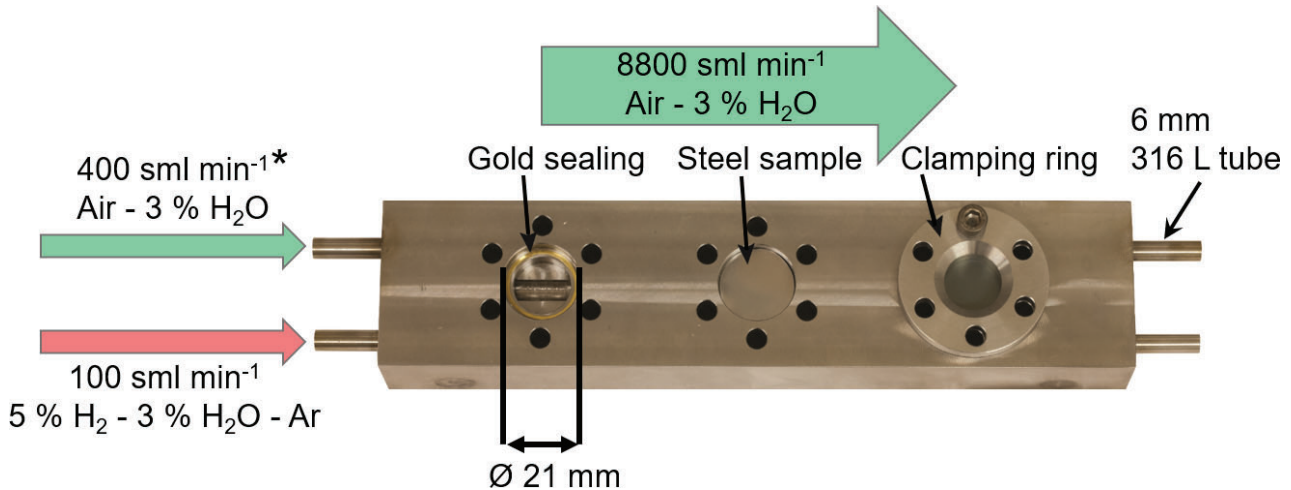


Figure 3.4: *Dual atmosphere sample holder. An additional three sample slots are on the reverse of the sample holder. * can be either 400 sml min⁻¹ air - 3 % H₂O (single atmosphere for three samples) or 100 sml min⁻¹ 5 % H₂ - 3 % H₂O - Ar (dual atmosphere for all six samples).*

the location of the pre-oxidation layer, i.e. the pre-oxidation layer on the air-facing side versus the pre-oxidation layer on the hydrogen-facing side.

Five different pre-oxidation times were chosen for the study on pre-oxidation time (see Table 3.3), ranging from 0 min to 280 min. The subsequent dual atmosphere exposure was run for 1 000 h, but to document the progress of oxidation and, if present, the progress of breakaway oxidation, the exposure was interrupted after 24 h, 168 h, 500 h, and 730 h, and photographs were taken. Repeat exposures were conducted up to 500 h, and the results matched well and were reported in [196].

To study the effect of pre-oxidation location on the dual atmosphere effect, AISI 441 samples were first pre-oxidized for 180 min and, subsequently, the pre-oxidation layer was removed from either the air-facing side or the hydrogen-facing side by grinding to grit P1200 or by polishing to 1/4 μm with Diamond paste. Samples that were ground or polished on both sides or on no side were used as reference samples. The final thickness was 0.2 mm for all tested samples. The scheme for how the samples were prepared can be found in Figure 3.5. Two sets of exposures were carried out: one for samples that were ground and one for samples that were polished. The exposures were run for 500 h with no interruption for the ground samples and one interruption after 168 h for the polished samples. The latter exposure was interrupted, because it was uncertain how long the pre-oxidized reference sample would last under these conditions, i.e. with a polished surface.

Thickness Study - Paper VI To study if the thickness of AISI 441 influences the dual atmosphere effect, 1 mm thick samples were ground down to four different thicknesses: 0.1 mm, 0.2 mm, 0.5 mm, and 0.7 mm. The final finish was grit P1200. The samples were then pre-oxidized for 20 min and, subsequently, exposed for 336 h with one interruption after 168 h to take photographs of the air-facing side.

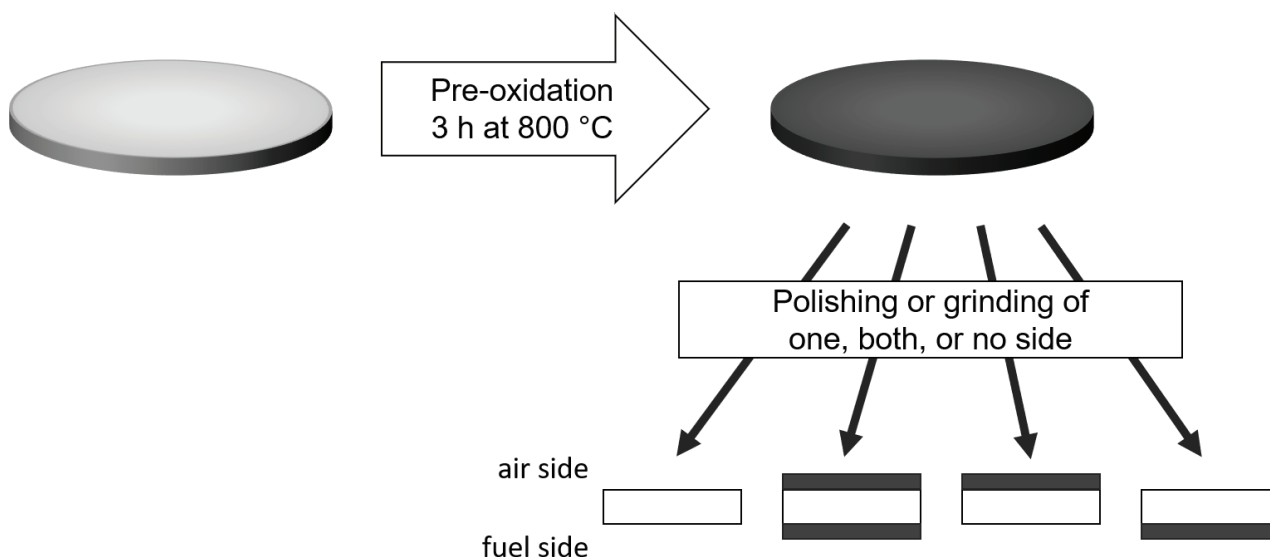


Figure 3.5: Scheme for pre-oxidation location experiment based on [197]. AISI 441 samples were first pre-oxidized for 3 h at 800 °C in air, and then the oxide layer was removed either by grinding (grit P1200) or by polishing (1/4 μm Diamond Paste).

Surface Treatment Study AISI 441 samples were ground to grit P1200, polished to diamond paste 1/4 μm , or left as-received on both sides. Dual atmosphere exposure was then conducted for 336 h with one interruption after 168 h. No pre-oxidation step was implemented.

3.3 Analytical Methods

Within the scope of this thesis, different analytical tools were used after, and in certain cases before, exposure of FSS samples. Apart from gravimetry and Cr evaporation, all other analytical techniques used are described in more detail below and the specifics on the instruments that were used are given.

Different analytical techniques were chosen depending on what was of interest within the scope of each study. The following techniques were used: spectrophotometry, area specific resistance (ASR) measurements, x-ray diffraction (XRD), broad ion beam milling (BIB), focused ion beam milling (FIB), scanning electron microscopy (SEM), energy dispersive x-ray spectroscopy (EDX), and scanning transmission electron microscopy. Table 3.4 gives an overview of which analytical techniques were applied for which study.

3.3.1 Spectrophotometry

The denuder technique described in Chapter 3.2.1 results in solutions containing hexavalent chromate, which exists in seven different forms CrO_4^{2-} , $\text{Cr}_2\text{O}_7^{2-}$, HCrO_4^- , H_2CrO_4 , HCr_2O_7^- , $\text{Cr}_4\text{O}_{13}^{2-}$, and $\text{Cr}_3\text{O}_{10}^{2-}$. Depending on the pH of the solution, different chromate ions or molecules are preferentially formed. At pH levels over 9 CrO_4^{2-} is nearly exclusively ($\geq 99.6\%$) formed [198]. Therefore, in the present work, the pH of all

Table 3.4: Analytical techniques used for each study. Cr evaporation measurements required the use of spectrophotometry.

Paper	Analytical Techniques Used
Paper I	ASR, XRD, BIB, SEM/EDX
Paper II	Spectrophotometry, BIB, FIB, SEM/EDX, STEM/EDX
Paper III	Spectrophotometry, ASR, BIB, SEM/EDX
Paper IV	BIB, SEM/EDX, FIB, STEM/EDX
Paper V	BIB, SEM/EDX
Paper VI	BIB, SEM/EDX
Paper ST	BIB, SEM/EDX

chromate containing solutions was checked with pH paper. In rare cases where the pH was too acidic, a few drops of NaOH were added to adjust it.

Solutions containing hexavalent chromate ions and/or molecules have in common that they absorb light regardless of their pH value. This property can be used to determine the concentration of chromate in the solution with spectrophotometry. However, the pH value does determine at what wavelength the absorption maxima are found. Two maxima are present at pH 9, one at 275 nm and another one at 371 nm. The latter value was employed to determine the chromate concentration in the present work, and this wavelength is within the ultraviolet spectrum.

Spectrophotometry can be used for all light-absorbing molecules. Figure 3.6 shows the working principle of this analytical technique. The collimator lens bundles the light, and a specific wavelength is chosen using the monochromator and the adjunct slit. The intensity of this light drops while passing through the to-be-examined solution, if the solution contains light-absorbing molecules. The relationship between the intensity of the incident light beam I_0 and the intensity of the light beam after having passed through the sample I_t can be expressed by the Beer-Lambert law (see Equation 3.2).

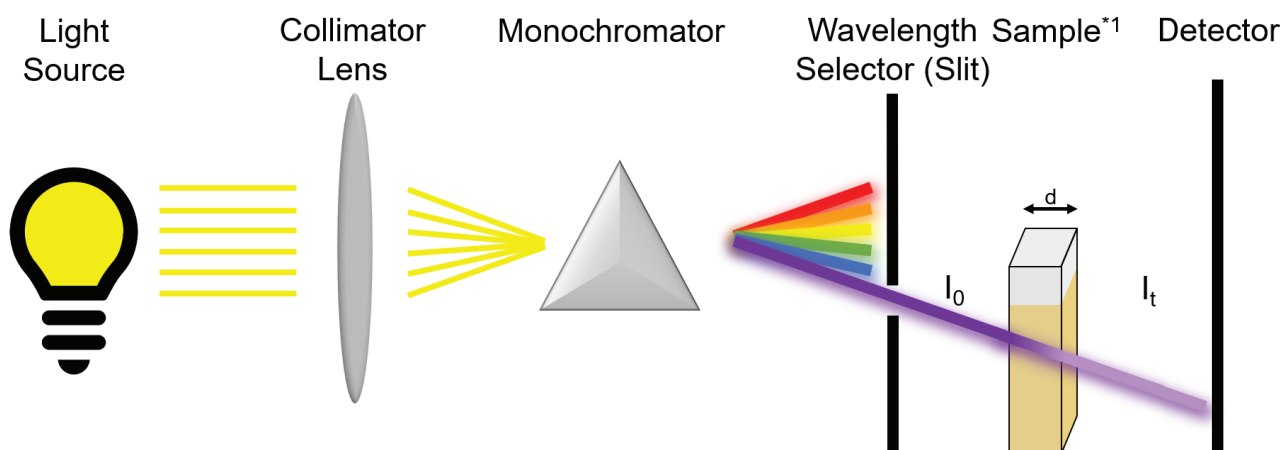


Figure 3.6: Schematic drawing of a Spectrophotometer with I_0 as the intensity of the incident light beam, I_t is the intensity of the light beam after passing through the sample, and d is the thickness of the cuvette. ^{*1}Cuvette containing sample solution.

$$A = \log_{10} \frac{I_0}{I_t} = \varepsilon_\lambda \cdot c \cdot d, \quad (3.2)$$

where A is the absorbance, ε_λ is the wavelength-dependent molar absorption coefficient, and d is the path length through the sample (cuvette thickness). In the present work, the coefficient ε_λ was determined by constructing a calibration curve using Merck chromate standard solution, which was diluted to different concentrations. A Thermo Scientific Evolution™ 60S UV-Visible spectrophotometer was used.

3.3.2 Area Specific Resistance

One important factor that influences the efficiency of a solid oxide fuel cell is the resistance of an interconnect, and this factor is influenced by the growth of oxide on the interconnect. This was discussed in detail in Chapter 2.3.3.

To analyze the resistance of the interconnect, the present work used a NORECS ProboStat™ (Norway) connected to a Keithley 2400 source meter. The setup is depicted in Figure 3.7. In addition to the wire Pt electrodes, which are shown in Figure 3.7ii, Pt was also applied directly to the samples to improve contact. For this purpose, the samples were first sputter coated with a roughly 100 nm thick Pt layer using a Quorum 150 sputter coater and then painted with a Pt paste (Metalor 6926) (see Figure 3.8). To remove the binder of the Pt paste, the samples were subsequently dried at 150 °C for 10 min and then sintered at the exposure temperature, which is shown in Table 3.3, for 1 h. Only ex-situ ASR measurements were conducted in this work, because *Grolig et al.* [80, 129] have previously shown that the Pt affected the overall resistance of the interconnect during in-situ measurements. All measurements were conducted in DC mode and with a current of 100 mA cm⁻². The ASR was measured at the exposure temperature and during the cooling down phase in increments of 25 or 50 °C until 450 °C. Measurements during the cooling down phase were done to confirm semi-conducting behavior, which validated that the oxide scale was being measured and that a short-circuit had not occurred. The ASR values herein are always stated and discussed for one side of the interconnect. For further information about these measurements, the reader is referred to [80, 129].

3.3.3 X-Ray Diffraction

X-ray diffraction can be used to characterize crystalline products. In addition to information about the structure of the examined material, the technique is also utilized to identify phases and phase compositions amongst other properties.

The working principle of an x-ray diffractometer is shown in Figure 3.9a [101, 199]. The incoming x-ray beam hits the surface of a sample. The x-ray beam is diffracted if it hits an atom, or rather the electron of an atom, otherwise it penetrates deeper into the sample until it hits an atom. The diffraction can occur in all directions, however, if the examined material is crystalline and highly structured, diffraction will occur into preferred directions, and constructive interference of the x-ray waves will be observed. The diffracted beams are in phase, if constructive interference is present, and this results

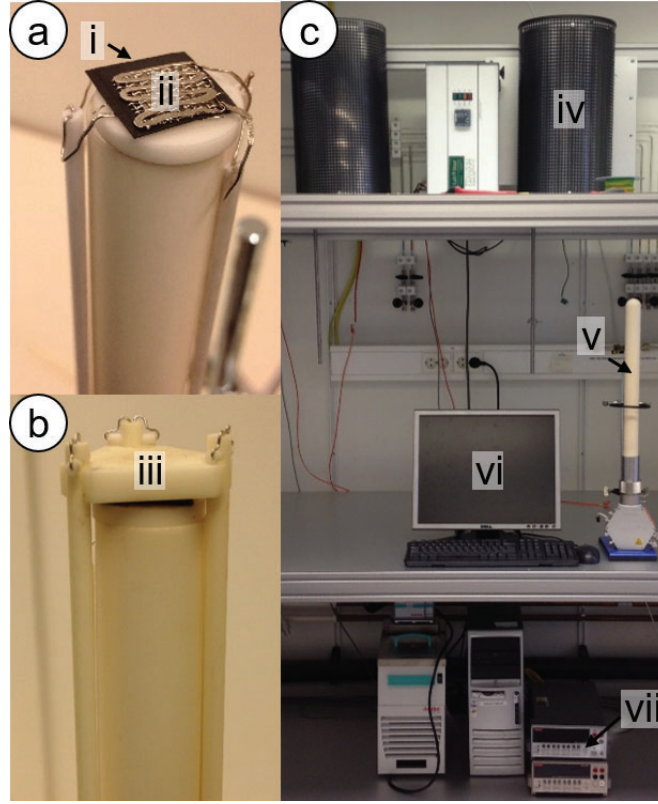


Figure 3.7: ASR setup. a) Mounted sample (i) with the Pt electrodes (ii), b) the top plate (iii) mounted on top of the sample, c) the entire setup, including furnaces (iv), closed ProboStat™ (v), computer with LabVIEW Program (vi), and Keithley 2400 source meter (vii) [80].

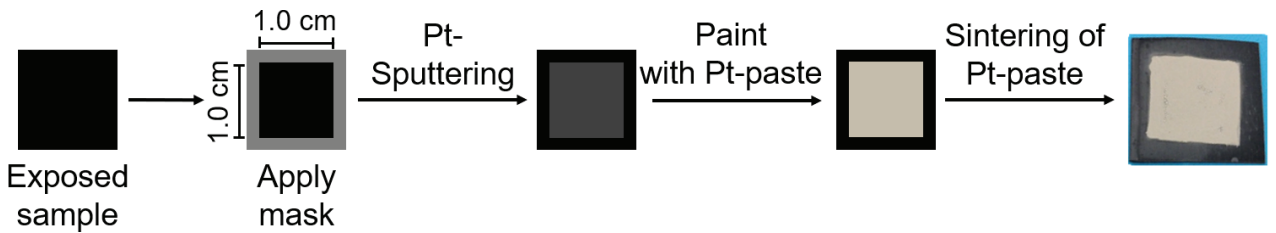


Figure 3.8: Schematic drawing of the electrode preparation process conducted prior to ASR measurement [80].

in sufficiently high intensity that can be recorded by the detector. Bragg's law [200] (see Equation 3.3) describes when constructive interference occurs.

$$n\lambda = 2d_{hkl} \sin \theta_{hkl}, \quad (3.3)$$

where n is an integer, λ is the x-ray beam wavelength, and d_{hkl} and θ are the parameters shown in Figure 3.9a.

A D5000 diffractometer with $\text{CuK}\alpha$ radiation ($\lambda = 1.54178 \text{ \AA}$) was used to record all XRD diffractograms within the scope of this thesis. The measurements were conducted in Bragg-Brentano geometry (see Figure 3.9b) and over the angular range $20^\circ \leq 2\theta \leq 70^\circ$. XRD was used solely to analyze the phase compositions of thermally grown oxides.

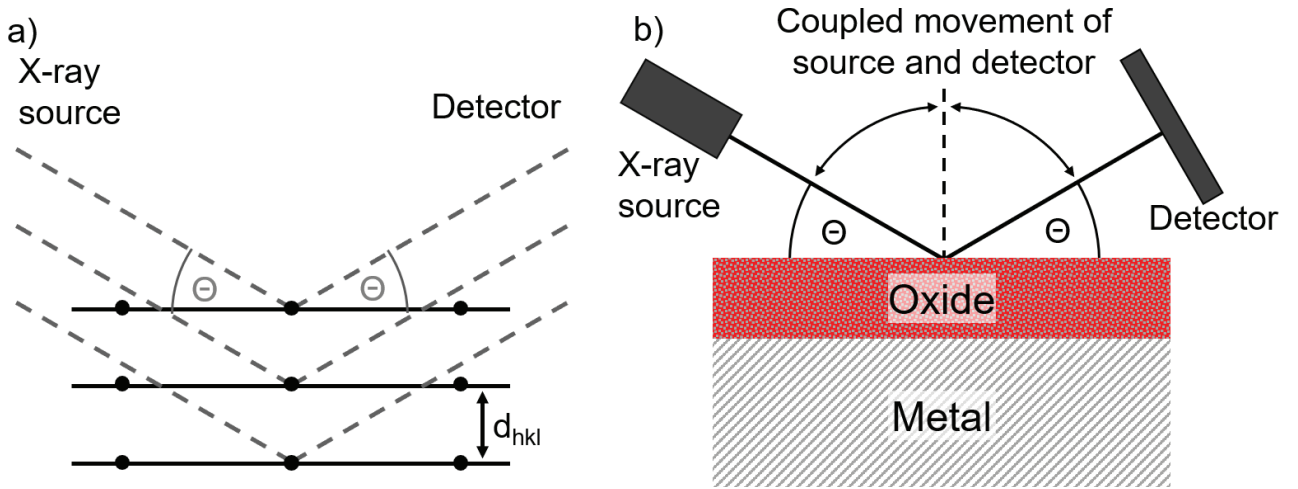


Figure 3.9: Schematic drawing of a) Bragg's law and b) Bragg-Brentano geometry.

3.3.4 Ion Beam Milling

Ion beam milling instead of mechanical preparation was used to prepare cross-sections that were subsequently analyzed using SEM/EDX or STEM/EDX. This was done to minimize impact on the thermally grown oxides. The ion beam milling process works by having heavy ions, such as Ga^+ or Ar^+ , hit the sample surface and slowly sputter the surface layer atoms away layer by layer. Two different ion beam mills were used in this thesis, FIB and BIB, and both were used for different purposes. The BIB mill has the advantage of preparing a broad cross-section that can be up to 2 mm wide, thus, giving a better overview of the sample. In contrast, focused ion beam milling is used for narrow cross-sections, typically around 10 to 20 μm wide. This technique is often used when small features are of interest. More details about both milling techniques are given below, including specifics on the instruments used.

Broad Ion Beam Milling The working principle of the BIB mill used herein is shown in Figure 3.10. The ion source was Ar^+ .

For broad ion beam milling, the samples were first cut in half with a low-speed saw, perpendicular to the rolling direction to ensure that a representative area was prepared.

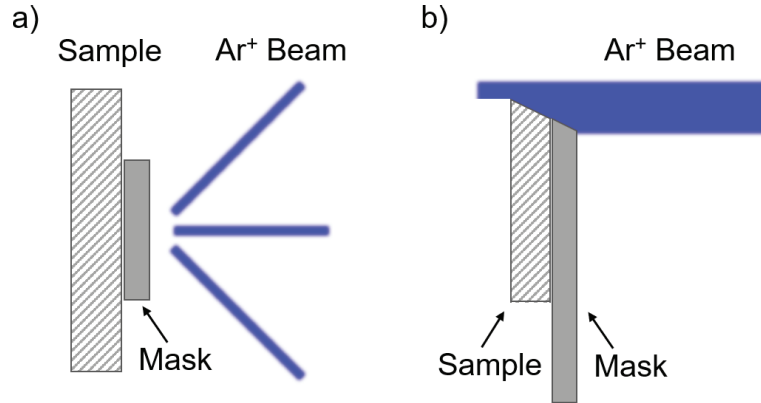


Figure 3.10: *Schematic drawing of the BIB used in this thesis. Three Ar^+ beams milled the sample. A) shows the top-view of the BIB, and b) shows the side view during the milling process. The drawing is based on [201].*

Then the to-be-milled sample was sputter coated with a thin Au layer to achieve better contrast and increase conductivity for electron microscopy. Subsequently, a Si wafer was glued onto the sample directly on the to-be-milled edge. The sample was mounted onto a BIB sample holder using silver paste and placed into the instrument. The mill used in this thesis was a Leica EM TIC 3X, and milling was achieved using 6.5 to 8 kV.

Focused Ion Beam Milling FIB milling uses Ga^+ ions to achieve highly polished cross-sections. It is a technique that can also be used for imaging, similar to electron microscopy. However, in contrast to electron microscopy, FIB imaging leads to the destruction of the sample. Today, FIB mills are typically integrated into an SEM, allowing for milling and imaging of the sample without moving from instrument to instrument. The two columns inside a FIB/SEM, the FIB and the SEM columns, are at a 52° angle to each other. In addition to imaging detectors, for secondary electrons and ions and backscattered electrons (description see Chapter 3.3.5), the FIB/SEM used in this thesis (FEI Versa3D LoVac DualBeam) was equipped with a Ga liquid ion metal source, an omniprobe, and a gas injection system, which was used for Pt deposition.

FIB milling was used to prepare thin lift-outs for further STEM analysis, because this drastically reduced the interaction volume (see Figure 3.12d) and, thus, avoided interfering with the EDX signal coming from below the surface. Figure 3.11 illustrates how these lift-outs, also called lamellas, were prepared. The Pt deposition acted as a protection against beam damage caused during the milling process.

3.3.5 Electron Microscopy

Electron microscopy is commonly used for imaging and analyzing the microstructure of samples, however, often additional detectors included in the microscope can be used for compositional or even structural information. The benefit of electron microscopy in contrast to optical microscopy is a much higher resolution. The two types of electron microscopes, SEM and STEM, used in this thesis are described in more detail below.

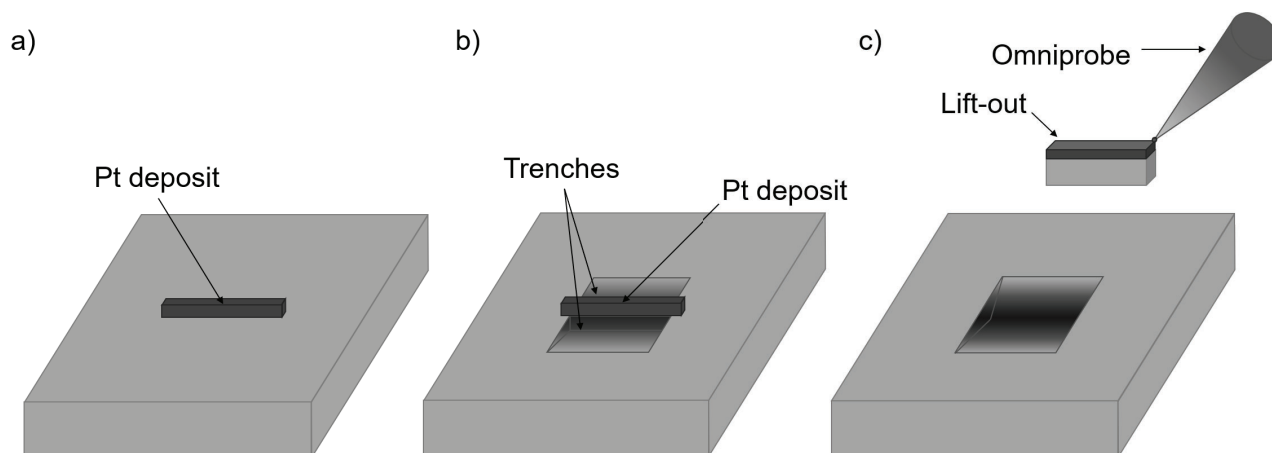


Figure 3.11: *Schematic drawing of how FIB lift-outs were achieved. First the to-be-lift-out area was sputter coated with a thick Pt layer (a), then trenches were milled next to the coated area (b), and finally the lift-out was attached to the omniprobe with Pt deposition and lifted out of the material (c). Subsequently, the lamella was attached to a Cu grid (not shown here) via Pt deposition.*

Scanning Electron Microscopy/Energy Dispersive X-Ray Spectroscopy SEM is used in the field of high temperature corrosion to analyze the microstructure of thermally grown oxides and/or microstructural changes within a material. SEMs are also typically equipped with an energy dispersive x-ray detector, which can also extract compositional data from the material. The reason for being well suited for imaging thermally grown oxides is that the high resolution of this technique can easily visualize even thin oxide scales. The resolution of this technique is highly dependent on the instrument, the detector, and the accelerating voltage used in each case, but resolutions down to 1 nm are possible. SEM works by detecting the interaction between accelerated electrons and the surface and near-surface atoms of the to-be-analyzed samples. Different emissions occur depending on the type of interaction, which can be detected using different detectors [101, 202, 203]. Three different SEM signals are frequently analyzed and were used within the scope of this thesis. These signals are described in more detail below. In addition to the generation process of these different signals, which is shown in Figure 3.12a-c, their interaction volume (see Figure 3.12d) is also important to know, because the interaction volume is not the same for the different signals, and misinterpretation of the results can occur if this difference in volume is not accounted for.

The analysis in the present thesis was conducted using three different SEMs:

- A Zeiss Ultra 55 FEG-SEM equipped with an Oxford Inca EDX system was primarily used to analyze cross-sections due to its high spatial resolution (1 nm at 15 kV).
- A FEI Quanta200 ESEM was used for top-view and EDX analysis. Its EDX detector, the Oxford X-max 80 EDX, had a higher resolution than the one included with the Zeiss microscope. However, the imaging resolution of the FEI microscope was worse at 2.1 nm for a 15 kV accelerating voltage than that of the Zeiss microscope.
- A FEI Versa3D LoVac DualBeam was utilized for the FIB milling, which was

discussed in Chapter 3.3.4.

All microscopes were equipped with a secondary electron detector and a backscattered electron detector.

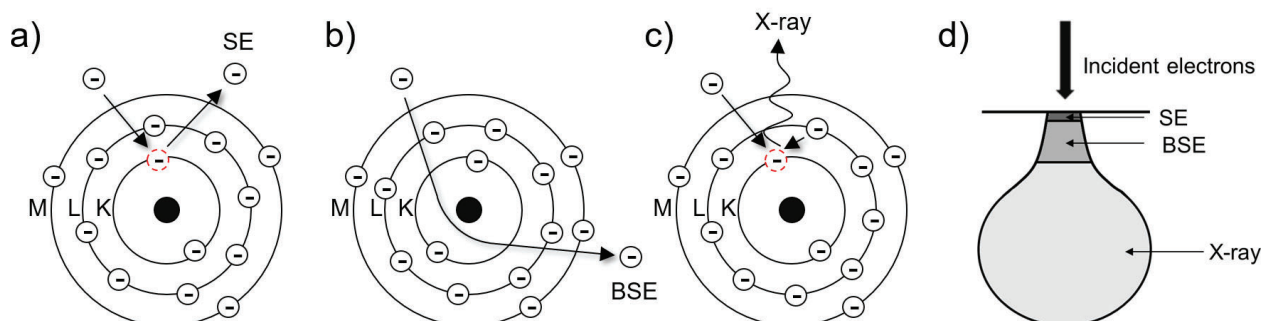


Figure 3.12: Schematic drawing of how different SEM signals are produced (a-c) and their respective interaction volume (d). The three SEM signals are a) secondary electrons, b) backscattered electrons, and c) x-ray radiation [101, 202, 203]

Secondary Electrons Inelastic scattering of incoming electrons on a weakly bound electron ejects that electron from the shell (see Figure 3.12a) [204]. This ejected electron is called a secondary electron (SE). The energy of an SE ranges from 1 to 20 eV (and can go up to 50 eV in some cases), which is lower than the other signals discussed in this context. The low energy means that only SEs, which are generated at the surface or close to the surface, can escape the material and be detected. SEs are highly surface sensitive (see Figure 3.12d) and, therefore, their detection results in very high-resolution micrographs, which convey surface topography information [202].

Backscattered Electrons Backscattered electrons (BSE) are electrons that stem from an incoming electron beam but are scattered elastically on the atomic nuclei (see Figure 3.12b). Because these electrons get scattered at the nucleus, and heavier atoms have a larger nucleus, the number of scattered BSEs for heavier atoms increases. This leads to more signal being detected for heavier atoms than for lighter atoms and, thus, compositional information can be derived from the backscattered signal. The energy of BSEs depends on two factors: the energy of the incident beam and how long the electron travelled through the sample. The latter factor leads to a decrease in energy due to inelastic scattering of the travelling electrons. In general, the energy of BSE ranges between zero keV and the incident beam energy, however, most BSE electrons retain at least half of the incident beam energy even for materials that are only weak elastic scatterers [205]. The interaction volume for the BSE is greater than that for the SE due to the much higher energy of former (see Figure 3.12d). Therefore, BSEs have poorer spatial resolution and, thus, image resolution than SE.

Energy Dispersive X-Ray Spectroscopy Energy dispersive x-ray emission occurs when the incident electron beam scatters inelastically on an electron in the atom shell.

This electron is then ejected and leaves a vacancy behind. By relaxing an electron from an outer shell into that vacancy, an x-ray photon with a specific energy is set free (see Figure 3.12c). The photon energy is dependent on the energy difference between the excited state and the relaxed state of the atom, which is given by the energy difference between the participating shells. As this energy difference is atom dependent, the photon energy is too, and detailed compositional information can be extracted from the signal [206]. In contrast to electrons, x-ray radiation penetrates a material much easier, and this results in an increased interaction volume for EDX (see Figure 3.12d) and, thus, a drastically reduced resolution. This can be an obstacle in cases where only the surface is to be analyzed, and consequently, FIB lamellas are prepared for such cases. The reduced thickness of lamellas artificially results in a reduced interaction volume.

Scanning Transmission Electron Microscopy Transmission electron microscopy (TEM) has an even higher spatial resolution (1 Å) than SEM and can easily resolve tiny microstructural features. The crystal structure of the material to-be-analyzed can also be determined with TEM if the material is crystalline. The reason for this is that in contrast to SEM, TEM detects the electrons that transmit through the samples. A simplified explanation of this process is that some of these electrons are diffracted according to Bragg's law (see Equation 3.3) [207]. Because the electrons are transmitted through the material in a TEM, the material must be electron transparent, and high incident beam energies around 200 keV are required. To achieve electron transparent samples, very thin samples around 100 nm are needed and FIB milling (see Chapter 3.3.4) is employed to prepare lift-outs and thin down samples sufficiently. All TEM work in this thesis was carried out by Dr. Vijayshankar Asokan on the FEI Titan 80-300, which was equipped with an Oxford X-sight EDX detector. The imaging was achieved in scanning TEM (STEM) mode and using a High-Angle Annular Dark-field (HAADF) detector. In addition to imaging, this detector also provides compositional information, because heavier atoms result in a brighter signal.

Results and Discussion

4.1 Nano-Coatings and their Influence on Corrosion Properties

Chapter 2.3.2 stressed the importance of coatings and discussed which corrosion phenomena can be mitigated by which coating. Co spinel coatings were mentioned as highly effective at decreasing Cr evaporation and RE coatings were introduced as a way to improve oxide scale adhesion during cycling and to decelerate oxide scale growth. The current state-of-the-art coating is a 10 nm thick Ce coating below a 640 nm thick Co coating. The oxidation behavior and resulting properties of coated interconnects are analyzed in the following. The main focus is on the Ce/Co coating or derivatives thereof.

4.1.1 Co Coating Thickness and Its Influence on Area Specific Resistance

Interconnects are required to be highly electron conductive, and this conductivity might be negatively affected by the coating. Therefore, countless publications focus on increasing the conductivity of the coating, for example, by adding dopants [39–45, 74, 208–210]. These studies, however, neglect to analyze if the impact of the coating on the resistance of an interconnect is significant, especially with regard to the continuously growing Cr_2O_3 underneath the coating. The conductivities of Cr_2O_3 and different spinels were discussed in Chapter 2.3.3. The conductivity of the former is significantly lower, by orders of magnitude, than the conductivity of Co- or Cu-containing spinels. One example, which is often used due to its good Cr retention property, is the Co_3O_4 spinel. Even though pure Co_3O_4 is a moderately good electron conductor with $\sigma_{\text{Co}_3\text{O}_4} = 6.7 \text{ S cm}^{-1}$ at 800 °C [153], its conductivity is still greater by a factor of 100 than the highest reported conductivity for Cr_2O_3 ($\sigma_{\text{Cr}_2\text{O}_3} = 0.05 \text{ S cm}^{-1}$ [162]). This large difference in conductivity has raised the question if the conductivity of the coating even matters, or if its impact on the overall conductivity of the interconnect is negligible compared to the impact of thermally grown Cr_2O_3 .

To answer this question, Crofer 22 APU was pre-oxidized and subsequently PVD coated with three different Co coating thicknesses, 600 nm, 1 500 nm, and 3 000 nm. The pre-oxidation was implemented to avoid the formation of an $(\text{Co,Cr,Fe})_3\text{O}_4$ layer (see Paper I). It has been suggested by *Falk-Windisch* et al. [159, 211] that a $(\text{Co,Cr,Fe})_3\text{O}_4$

layer forms, because of inter-metallic diffusion during the initial stages of oxidation. This inter-metallic diffusion is prevented by the presence of a thin oxide between the alloy and the metallic coating. After applying the Co coating, the samples were exposed to air for 500 h at 600 °C. These exposure parameters were expected to result in a very thin Cr_2O_3 scale (below 100 nm), in contrast to fairly thick and non-doped Co_3O_4 scales (1.2-5.7 μm according to the PBR [100]). This ratio in thickness should lead to a worst-case scenario. The ASR of all samples was measured after exposure. Different ASR values would be expected for different coating thicknesses if the conductivity of a coating significantly impacts the resistance of an interconnect.

Microstructural Analysis Similar oxidation behavior was found for all pre-oxidized Co-coated Crofer 22 APU samples with the formation of a thin Cr_2O_3 scale below a thick Co_3O_4 scale (see Figure 4.1). The thickness of the Cr_2O_3 scale was the same for all samples, 35-45 nm. In contrast, the Co_3O_4 thickness after exposure was in agreement with the PBR ratio for Co (PBR = 1.98, see Table 2.1 [104]) and resulted in 1.2 μm , 2.8 μm , and 5.7 μm for the 600 nm, 1 500 nm, and 3 000 nm thick Co coatings, respectively. EDX analysis confirmed the purity of the Co_3O_4 scale, with negligible levels of Mn, Fe, and Cr. The Co_3O_4 scale on some of the 3 000 nm Co-coated samples suffered from spallation (see Figure 4.1d).

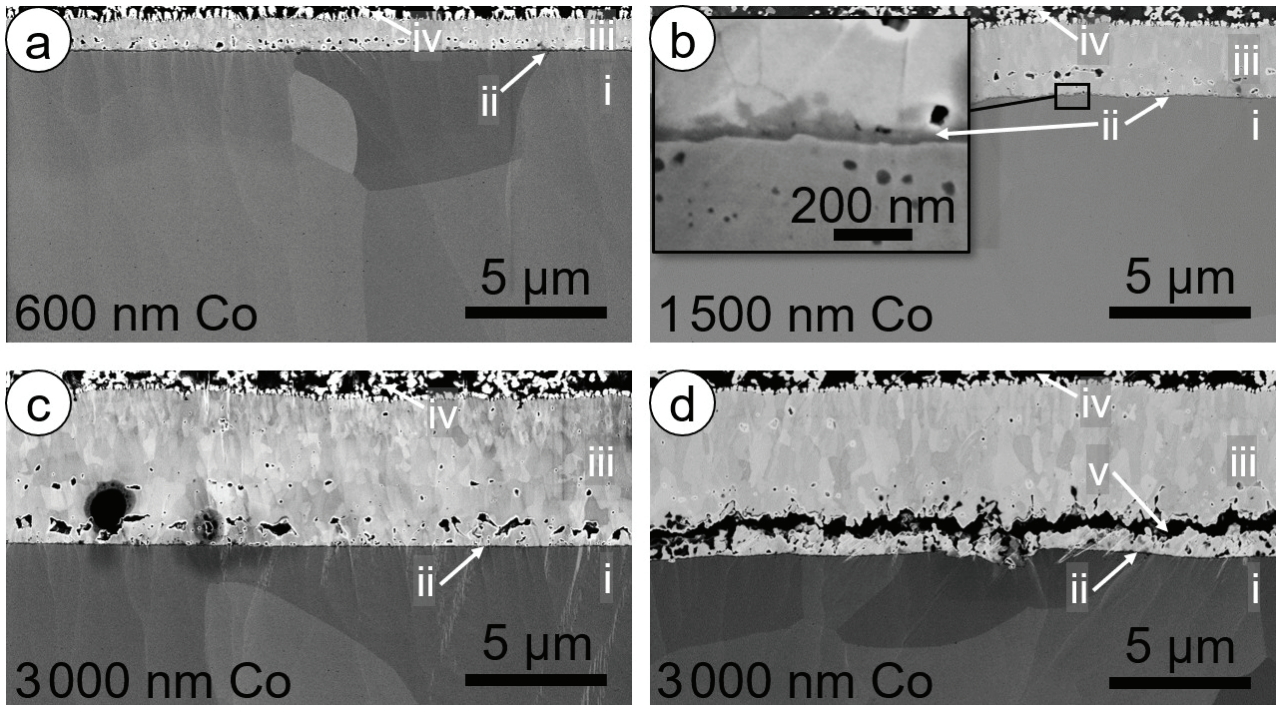


Figure 4.1: SEM micrographs of BIB milled cross-sections of Co-coated Crofer 22 APU exposed for 500 h at 600 °C. All samples were pre-oxidized for 3 min and subsequently Co-coated with three different thicknesses: a) 600 nm Co coating, b) 1 500 nm Co coating, c) and d) 3 000 nm Co coating. Some samples showed signs of spallation for the latter thickness, (d), while others did not, (c). The phases were identified as follows: i) steel substrate, ii) Cr_2O_3 , iii) Co_3O_4 , iv) Pt electrode, and v) spallation crack.

Area Specific Resistance The area specific resistance values for Co-coated Crofer 22 APU were between 8 and 12 mΩ cm² for all coating thicknesses and were, thus, independent of coating thickness (see Figure 4.2).

The error bars of the ASR values were minimal for non-spalled samples, but they were significant for spalled samples. The reduced contact caused by spallation and the difference in the extent of spallation between different samples (see Figure 4.1) can explain the large spread of the ASR values for the spalled samples and the higher ASR values for the spalled samples in contrast to the non-spalled samples (see Figure 4.2).

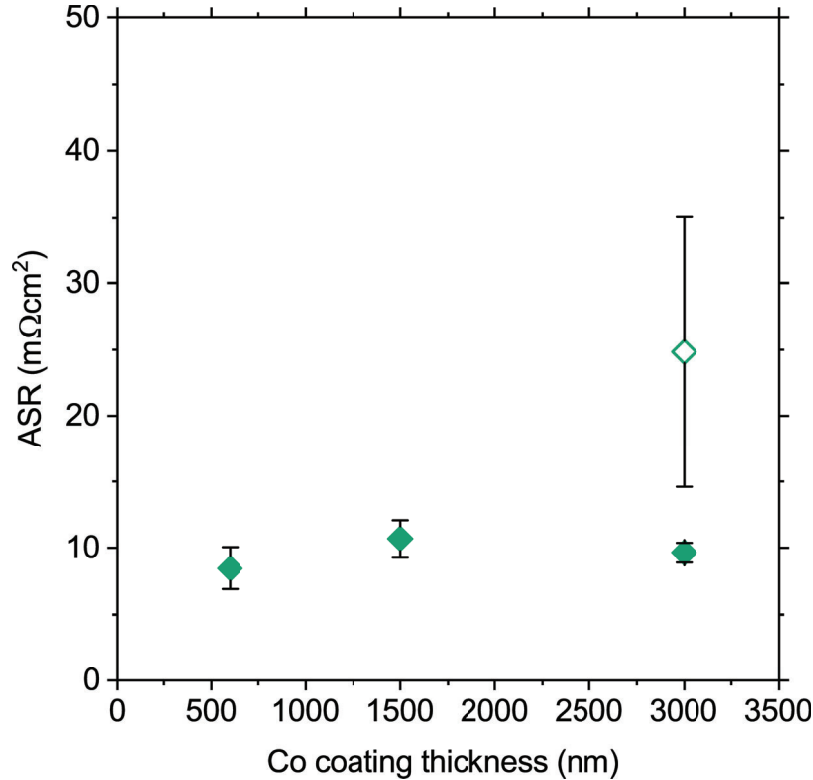


Figure 4.2: Area specific resistance of Co-coated Crofer 22 APU exposed for 500 h at 600 °C. Empty symbols indicate samples that showed signs of spallation. Error bars indicate standard deviations.

Theoretical calculations confirmed that the conductivity of the coating does not contribute significantly to the overall ASR value of the interconnect. Equations 2.29, and 2.30 from Chapter 2.3.3 were used for these calculations. The literature values for the conductivities and the activation energies of Co₃O₄ and Cr₂O₃ employed in these calculations and the calculated resistance R for each oxide at 600 °C can be found in Table 4.1. The spread in literature values for the conductivity and activation energy of Cr₂O₃ was large. The value reported by Park et al. [167] was used herein, as their values are very similar to the average values found over different publications [72, 80, 161, 163–168]. Equation 4.1 was used to calculate the theoretical ASR with the conductivity values shown in Table 4.1.

$$ASR_{cal} = A \cdot [R_T(Co_3O_4) + R_T(Cr_2O_3)], \quad (4.1)$$

where A equals 1. The calculated ASR values were $1.69 \text{ m}\Omega \text{ cm}^2$ for the 600 nm Co-coated Crofer 22 APU, and $2.16 \text{ m}\Omega \text{ cm}^2$ for the 3000 nm Co-coated Crofer 22 APU with the contribution of the Co_3O_4 to the overall ASR of these samples being 8 % and 28 %, respectively. Even though 28 % sounds non-negligible, it should be stressed that the situation with such a thin Cr_2O_3 scale is an extreme scenario, and the ratio between the thickness of an oxidized coating and Cr_2O_3 is skewed in the other direction, i.e. the Cr_2O_3 scale will be thicker than the Co_3O_4 scale after long exposure times and/or at higher temperatures. The theoretically calculated ASR values were in good agreement with the experimental values, especially given that the spread in the literature values for Cr_2O_3 is extremely large.

Table 4.1: Literature values and calculated values for the conductivity and corresponding resistance of Co_3O_4 and Cr_2O_3 . E_a and $\sigma_{800^\circ\text{C}}$ correspond to literature values, $\sigma_{600^\circ\text{C}}$ was calculated using Equation 2.29, L represents the average thickness of the observed oxide layer obtained from the cross-sections (Figure 4.1), and $R_{600^\circ\text{C}}$ was calculated according to Equation 2.30 with the area $A = 1 \text{ cm}^2$.

	E_a (eV)	$\sigma_{800^\circ\text{C}}$ (S cm^{-1})	$\sigma_{600^\circ\text{C}}$ (S cm^{-1})	L (nm)	$R_{600^\circ\text{C}}$ ($\text{m}\Omega$)
Co_3O_4	0.79 [212]	6.7 [153]	0.94	1 200	0.13
				5 700	0.60
Cr_2O_3	0.46 [167]	0.008 [167]	0.0026	40	1.56

In general, it was found that the conductivity of the coating only marginally affects the overall ASR value of an interconnect despite extreme conditions, i.e. relatively thick coating compared to an extremely thin Cr_2O_3 scale. It is suggested that coating conductivity can be disregarded in most practical applications, and instead, research should focus on decelerating Cr_2O_3 scale growth.

4.1.2 Self-healing Capabilities of Ce/Co Coating at Intermediate Temperatures

In Chapter 2.3.2, the self-healing capability of the Ce/Co coating was discussed. This capability has to-date only been reported at 850°C [47, 48]. The trend towards lower operating temperatures for SOFCs warranted a re-investigation of the self-healing capability at 650 and 750°C , because the self-healing process is diffusion dependent and, therefore, temperature dependent.

For this investigation, Ce/Co-coated AISI 441 was deformed biaxially after the coating had been applied using PVD. Exposure and Cr evaporation measurements were then carried out at 750 and 650°C .

Cr evaporation Rate A slight difference between the initial oxidation rates of deformed and non-deformed Ce/Co-coated AISI 441 was found at 750°C (see Figure 4.3a). This difference vanished after 71 h of exposure, and the rate for both materials was then stable around $1.2 \cdot 10^{-5} \text{ mg cm}^{-2} \text{ h}^{-1}$. The initial decline for the deformed Ce/Co-coated AISI 441

samples was much more significant at 650 °C, and the initial Cr evaporation rate was even higher than the initial rate of the deformed material at 750 °C. However, the Cr evaporation rate declined even at 650 °C, and the Cr evaporation rates for deformed and non-deformed material fluctuated around $3.3 \cdot 10^{-6} \text{ mg cm}^{-2} \text{ h}^{-1}$ after 360 h. These results strongly suggest that self-healing occurs at 650 °C and 750 °C, even though the process decelerates at those temperatures in contrast to 850 °C, where the healing process was complete after 24 h [47, 48].

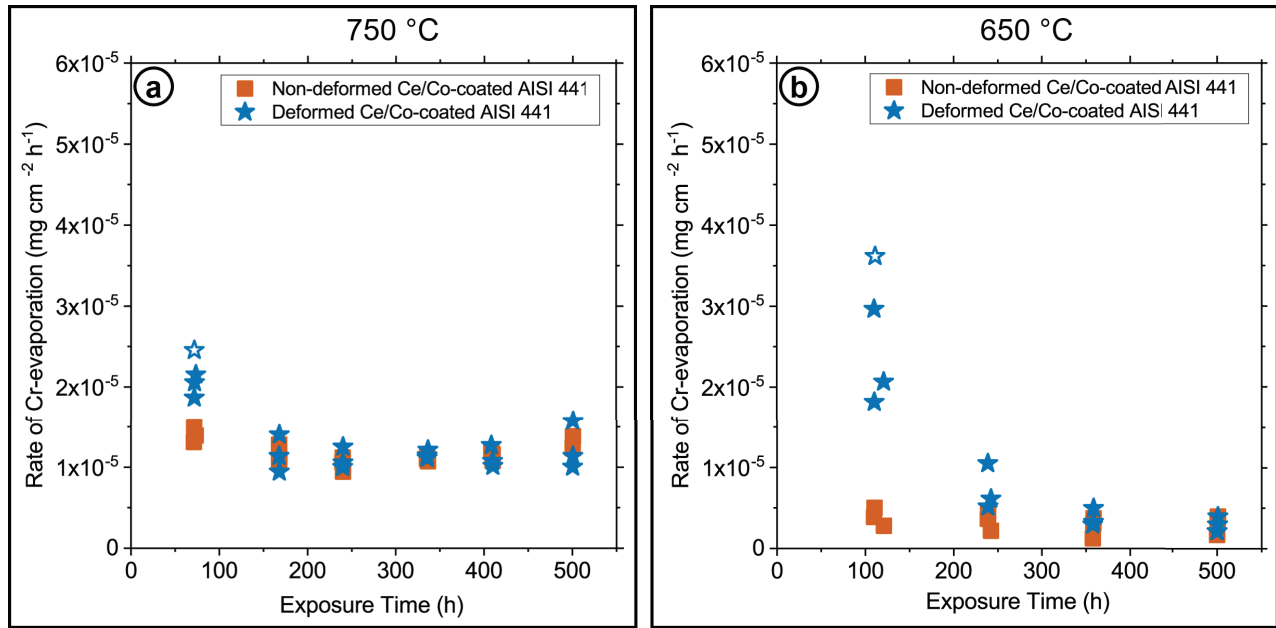


Figure 4.3: Cr evaporation rate for deformed and non-deformed Ce/Co-coated AISI 441 samples that were exposed at 750 °C (a) or 650 °C (b). Empty symbols mark samples that were removed from the furnace after 71 h or 111 h of exposure at 750 °C or 650 °C, respectively.

Microstructural Analysis After 500 h of exposure at 750 °C, deformed Ce/Co-coated AISI 441 showed almost homogeneous Co coverage of the entire sample surface in the EDX maps, even though the cracks were still visible in the top view SEM micrograph (see Figure 4.4a). This discrepancy can be easily explained by the penetration depth of the EDX in comparison to the depth of the SE used for top view imaging (see Figure 3.12). In contrast, the cracks were still visible in the EDX maps after 500 h of exposure at 650 °C, however, it seemed as if small quantities of Co had diffused into these cracks (see Figure 4.4b). Fe-rich oxide nodules were only found for the deformed Ce/Co-coated AISI 441 samples exposed at 650 °C (see Figure 4.4b arrow). These nodules were analyzed using BIB milled cross-sections and EDX maps and consisted of four oxide layers, which from the top to the bottom layer were: a thin (0.4 μm) relatively pure Co₃O₄ layer with less than 10 at% Fe, a (Co,Fe)-rich oxide (~1.5 μm), a relatively pure Fe oxide and finally Cr₂O₃ with 10 to 20 at% Fe and up to 3 at% Mn incorporations (see Paper II). The latter two layers varied in thickness throughout the nodule. Because the nodules were covered in a top Co-rich oxide with no Cr content, they were not expected to negatively impact the

Cr evaporation rate. This was confirmed by the evaporation rate, which after a certain time interval was the same for deformed and non-deformed material, even though only the former showed the presence of Fe-rich nodules (see Figure 4.3, Figure 4.4 and Paper II).

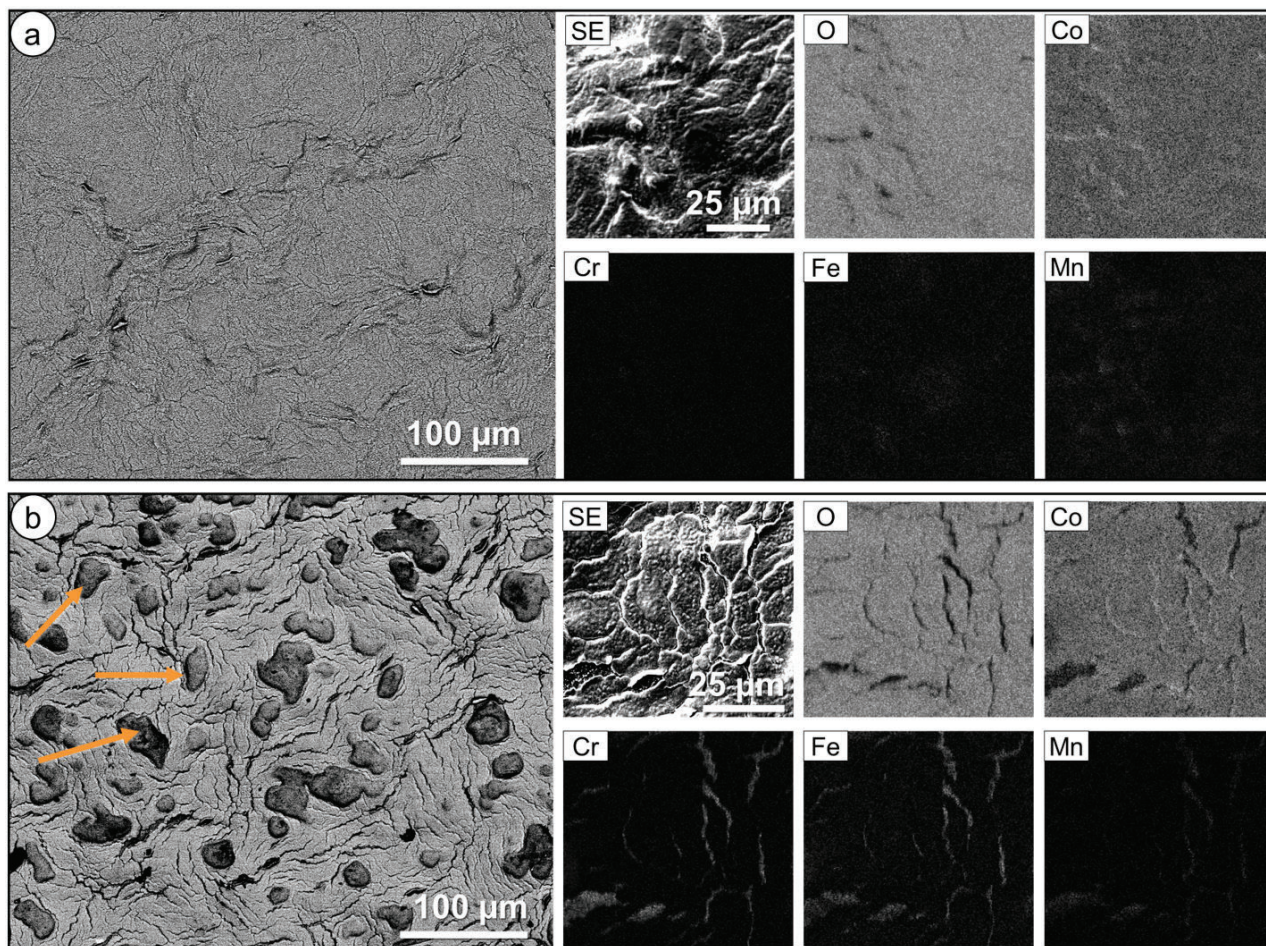


Figure 4.4: SEM micrographs and quantitative EDX maps (at %) for biaxially deformed Ce/Co-coated AISI 441 samples that were exposed for 500 h in humid air either at 750 °C (a), or at 650 °C (b).

After only 71 h at 750 °C, a relatively thick Co-oxide scale, ranging between 300 and 400 nm, had formed on top of the crack (see Figure 4.5). The Co oxide was made up of 20 to 30 cationic% Mn and 7 cationic% Fe, whereas the Co oxide in the non-cracked area showed high purity with only 5 cationic% Mn and less than 3 cationic% Fe. The high Mn content in the Co-rich oxide that covered the cracked area is in agreement with what Falk-Windisch et al. [47, 48] reported. Those authors have suggested that this high Mn content is due to the initial formation of a $(\text{Cr,Mn})_3\text{O}_4$ spinel on top of the cracked area. Only the subsequent lateral diffusion of Co into the cracked area was found to lead to continuous Co enrichment of the scale. A Cr_2O_3 scale had formed below the Co-rich oxide in both the non-cracked and the cracked regions. This Cr_2O_3 scale was slightly thinner in the cracked region (~ 230 nm) than in the non-cracked region (~ 280 nm), which might be due to the fact that a substantial amount of Cr, up to 40 cationic%, was found in

the Co-rich spinel of the former. A seemingly continuous Ce layer was detected in the non-cracked regions, but not in the cracked regions.

The formation of a relatively thick Co-rich oxide on top of cracked regions after as little as 71 h of exposure verified the conclusion drawn from the behavior of the Cr evaporation rate, namely that the self-healing process at 750 °C is complete sometime before 71 h of exposure.

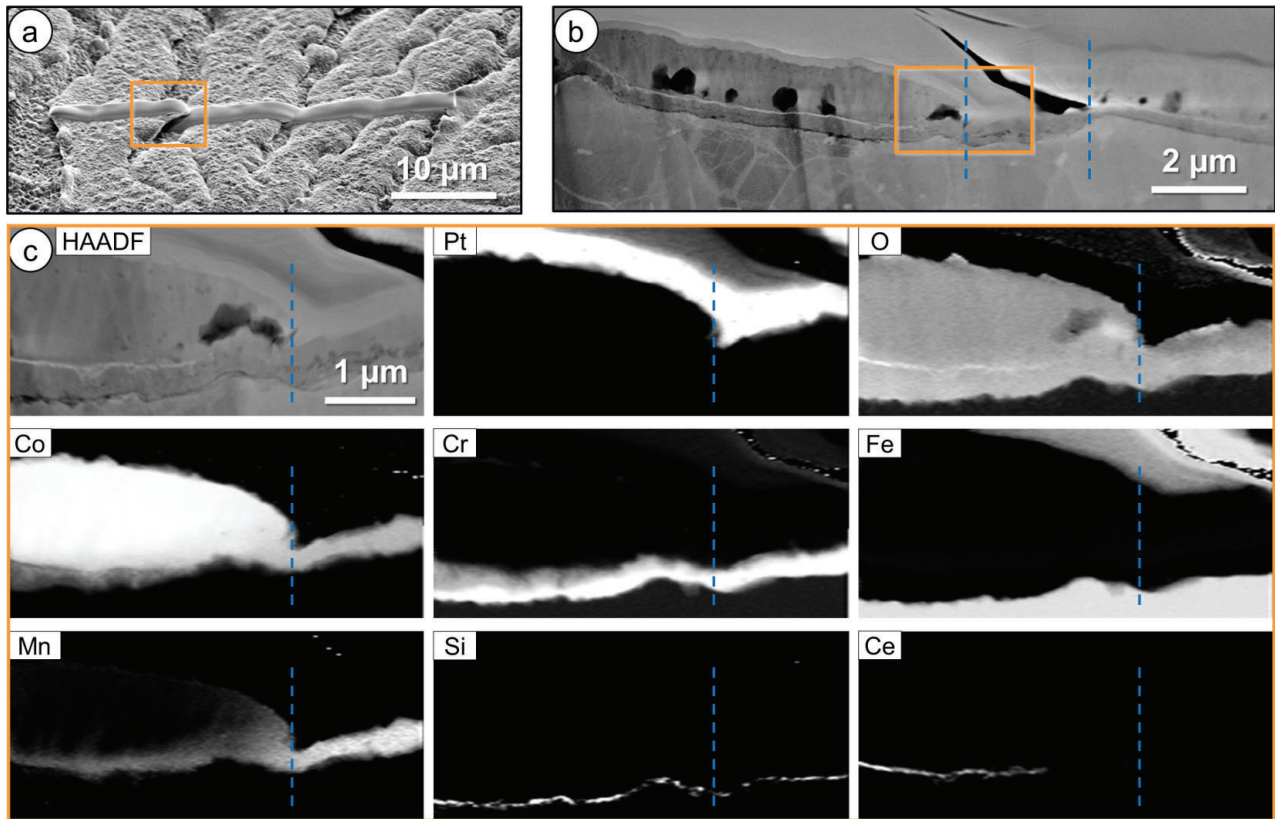


Figure 4.5: *Electron microscopy of a biaxially deformed Ce/Co-coated AISI 441 sample that was exposed to air for 71 h at 750 °C. The crack marked by the orange box was investigated with STEM/EDX. A) SEM micrograph with Pt deposited on the area chosen for the FIB lift-out; b) HAADF micrograph of lift-out, with the area inside of the blue dashed lines marking the cracked area; c) HAADF image and corresponding EDX maps in at%. The cracked area is on the right side of the blue dashed line, and the non-cracked area is on the left side of the line.*

The healing process was not yet completed after 111 h of exposure at 650 °C, according to the Cr evaporation data. However, a very thin Co-rich oxide was found in the cracked area (~ 30 nm) with up to 30 cationic% Co, 35 to 40 cationic% Fe, and between 5 to 30 cationic% Cr (see Figure 4.6). A Cr-rich oxide scale had formed below this Co-rich oxide. The exact composition of this Cr-rich oxide could not be determined accurately, because of the thinness of this scale (around 20 nm). Similar as to the sample analyzed at 750 °C, no strong Ce signal was detected in the cracked regions at 650 °C, whereas a Ce signal was clearly visible in the non-cracked regions. The absence of Ce in cracked regions could explain the formation of the Fe-rich oxide nodules found at 650 °C. *Falk-Windisch*

et al. [159, 211] have previously shown that Fe-rich oxides form at 650 °C if no Ce layer is present to prevent intermetallic diffusion in the initial stages of oxidation. This strongly suggests that the formation of Fe-rich oxide nodules occurred in the present work, because the cracks appeared not to contain Ce, or not sufficiently high levels of Ce.

The presence of a thin Co-rich oxide after 111 h of exposure at 650 °C confirmed the Cr evaporation data, which showed a steep decline in the rate of evaporation after 111 h. This indicates that the healing process was underway. The Cr evaporation data (see Figure 4.3) in combination with the SEM top view data collected after 500 h of exposure (see Figure 4.4) showed that self-healing at a temperature as low as 650 °C does occur, even though the process is much slower than at 850 °C.

Nevertheless, the Cr evaporation rate for deformed Ce/Co-coated AISI 441 samples was much lower than that of the uncoated material, even in the initial phases (see Paper II). Consequently, the Cr evaporation of deformed Ce/Co-coated AISI 441 should not play a role in the fuel cell degradation caused by cathode poisoning.

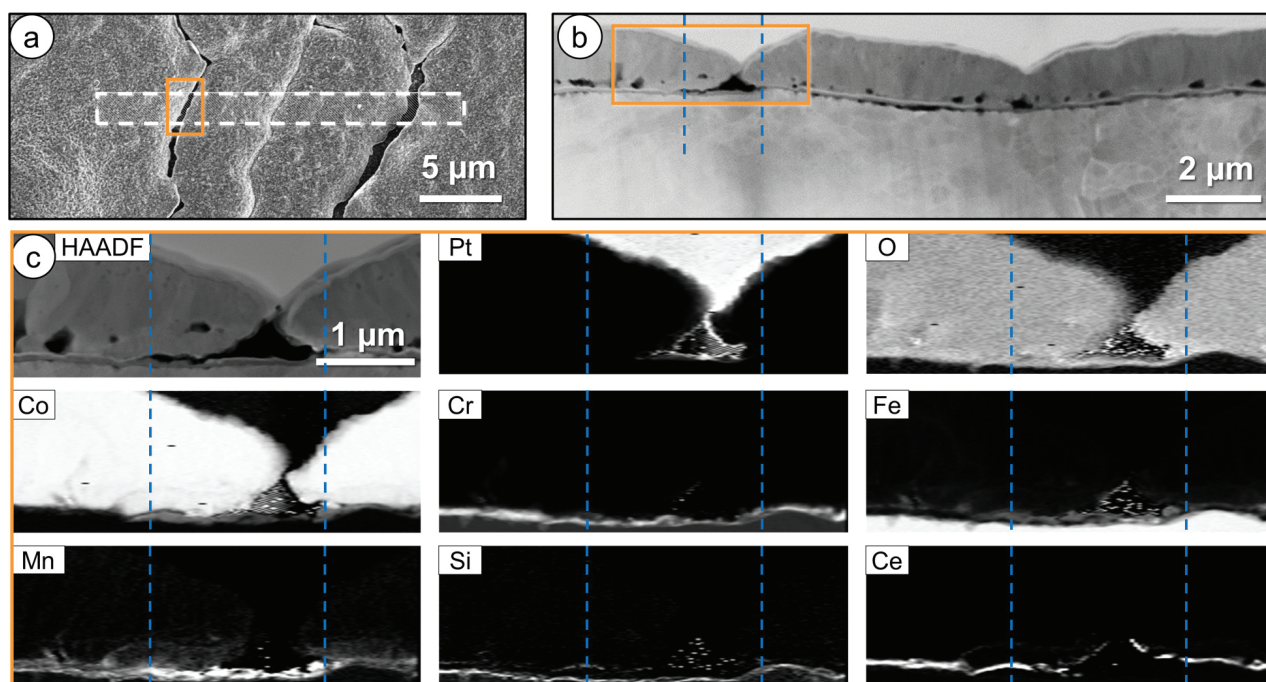


Figure 4.6: *Electron microscopy of a biaxially deformed Ce/Co-coated AISI 441 sample that was exposed to air for 111 h at 650 °C. The crack marked by the orange box was investigated with STEM/EDX. A) SEM micrograph with the area chosen for the FIB lift-out marked by the dashed white box; b) HAADF micrograph of lift-out. The area inside of the blue dashed lines marks the cracked area; and c) HAADF image and corresponding EDX maps in at%.*

The self-healing process still occurs at temperatures as low as 650 °C, even though the process is slower than at 850 °C. This means that economic roll-to-roll manufacturing processes for coated interconnects can be used without negatively influencing fuel cell degradation.

4.1.3 Long-Term Stability of Ce/Co-Coated AISI 441

The two main issues to overcome on the interconnect level to achieve wide-spread commercialization of SOFCs are the limited life-time due to material degradation and high material cost. As discussed previously (see Chapters 2.3.1 and 2.3.2) the former can be improved by coatings that mitigate the oxidation of the FSS, for example, the state-of-the-art coating Ce/Co [56, 57], and the latter issue can be addressed by the use of cheaper materials, such as AISI 441, instead of expensive steels, such as Crofer 22 APU. The Ce/Co coating has been shown to excel at Cr retention and improved oxidation resistance for exposure lengths up to 3 000 h [33–36, 154]. However, very little work has to-date been carried out on the long-term stability ($> 3\,000$ h) of coated interconnects. Therefore, the present work analyzes the long-term stability of Ce/Co-coated (10 nm Ce/640 nm Co) AISI 441. For this purpose AB Sandvik Materials Technology exposed the material discontinuously for up to 37 000 h at 800 °C in a box furnace. Subsequent analysis was carried out at Chalmers.

Gravimetric Analysis The mass gain for Ce/Co-coated AISI 441 was near parabolic even up to 37 000 h of exposure at 800 °C (see Figure 4.7). A slight difference was found between the two different batches, which could be due to batch variations. The initial increase in mass gain to 0.21 mg cm^{-2} can be attributed to the oxidation of the Co coating and is in agreement with previously published work on the same coating [58, 130]. This also explains why the mass gain of uncoated material is lower than that of the coated material. The mass gain of isothermally tube furnace exposed Ce/Co-coated samples was similar to the mass gain of discontinuous box furnace exposed samples after 1 000 h of exposure, however, a notable difference was found after 3 000 h of exposure, which could be due to the thermal cycling the latter samples experienced.

Microstructural Analysis The microstructure of Ce/Co-coated AISI 441 was the same for the three exposure lengths, 7 000 h, 23 000 h, and 35 000 h, (see Figure 4.8). A thermally grown Cr_2O_3 layer had formed below a roughly $2.2\text{ }\mu\text{m}$ thick $(\text{Co,Cr,Mn})_3\text{O}_4$ spinel. The thickness of the Cr_2O_3 layer varied between different exposure times, which is in agreement with the gravimetric analysis, but the thickness of this layer also varied significantly within each sample (see Table 4.2).

Table 4.2: Thickness of the $(\text{Co,Cr,Mn})_3\text{O}_4$ spinel and the thermally grown Cr_2O_3 layer that formed on Ce/Co-coated AISI 441, which was exposed for 7 000 h, 23 000 h, and 35 000 h to air at 800 °C. All values are given in μm .

Exposure Time	$(\text{Co,Cr,Mn})_3\text{O}_4$ thickness (μm)				Cr_2O_3 thickness (μm)			
	Min	Max	Avg.	Std. Dev.	Min	Max	Avg.	Std. Dev.
7 000 h	1.5	2.6	2.0	0.6	4.5	9.8	6.5	1.9
23 000 h	0.7	3.4	2.2	1.1	7.0	15.6	10.9	3.0
35 000 h	2.7	3.1	2.9	0.2	10.9	18.1	14.9	2.8

The Cr content of the steel, which is an important factor when discussing the long-term

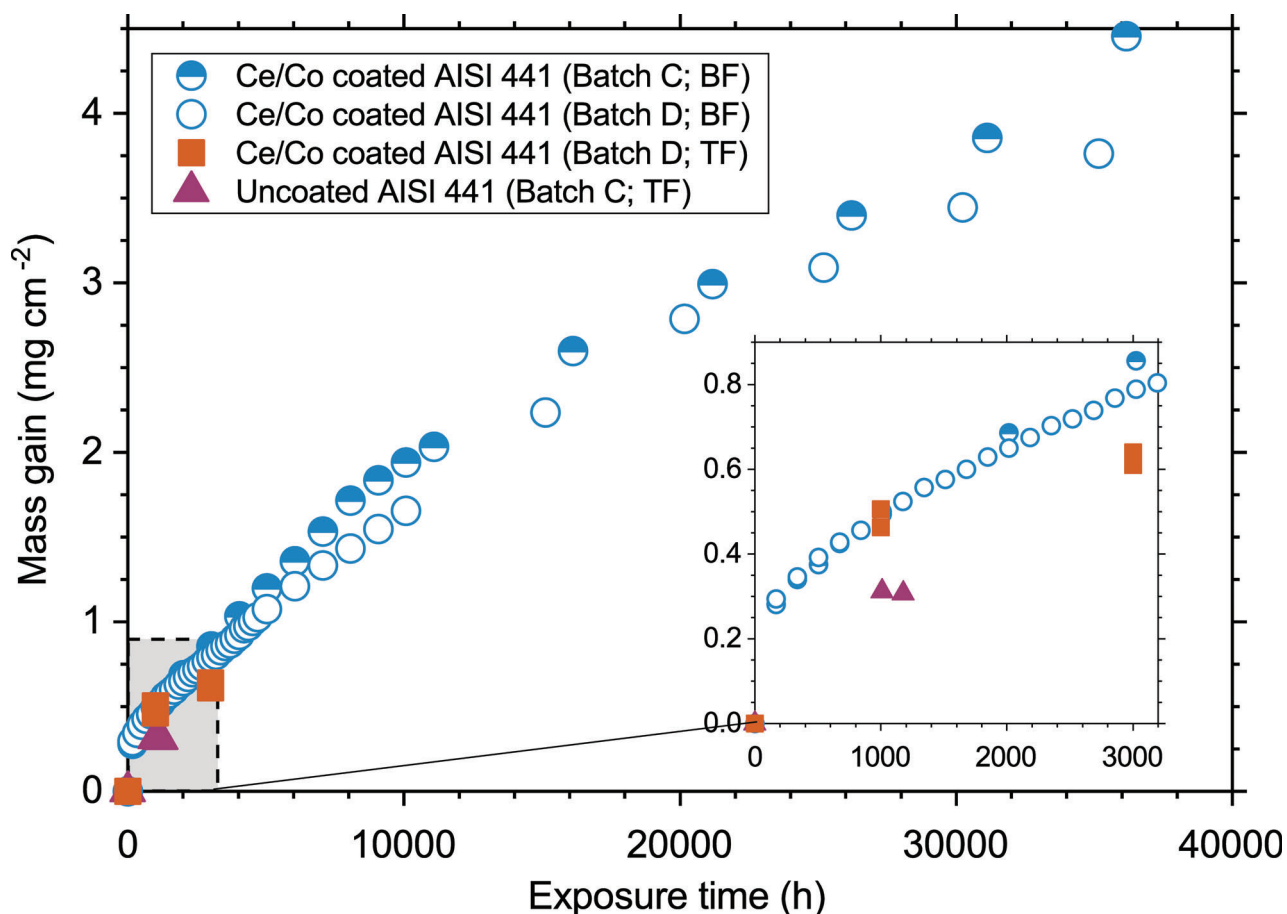


Figure 4.7: Mass gain for AISI 441 exposed up to 37 000 h at 800 °C. Different AISI 441 batches were exposed and are specified in the legend. Samples were exposed either discontinuously in box furnaces (BF) by Sandvik Materials Technology or isothermally in tube furnaces (TF) at Chalmers. The mass gain values recorded for box furnace exposed samples were averaged over a range of samples, whereas all short-term tube furnace exposed samples ($\leq 3\,000$ h) are specific values measured for one sample. The overall exposure time for Ce/Co-coated AISI 441 batch C was 37 000 h. These samples were used for subsequent Cr evaporation measurements. The overall exposure time for Ce/Co-coated AISI 441 batch D was 35 000 h. These samples were used for subsequent ASR measurements.

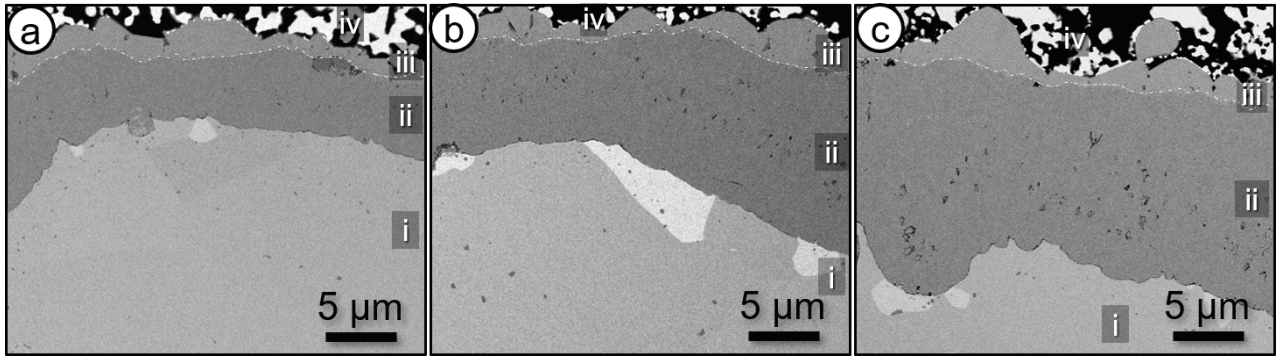


Figure 4.8: Backscattered SEM micrographs for BIB milled cross-sections of Ce/Co-coated AISI 441 that was exposed to air at 800 °C for 7000 h (a), 23 000 h (b), and 35 000 h (c). The ASR of these samples was measured prior to preparing each cross-section. The phases were identified with EDX analysis and XRD as i) steel substrate, ii) Cr_2O_3 , iii) $(\text{Co,Cr,Mn})_3\text{O}_4$, and iv) Pt-electrode.

stability of a FSS, had dropped from 17.8 wt% before exposure to 16.5 wt% after 7 000 h of exposure, 13.8 wt% after 23 000 h of exposure, and 11.8 wt% after 35 000 h of exposure. The substantially lower Cr content after 35 000 h might signal imminent material failure. However, the material lasted for at least another 3 000 h (see Cr evaporation data). A thicker Ce coating could be applied to decrease Cr consumption further [213].

Cr Evaporation Low Cr evaporation rates for Ce/Co-coated AISI 441 were found even after 37 000 h of exposure (see Figure 4.9) in comparison to the rate for uncoated AISI 441. The average rate of the latter was $1.8 \cdot 10^{-4} \text{ mg cm}^{-2}\text{h}^{-1}$, while it was $2.5 \cdot 10^{-5} \text{ mg cm}^{-2}\text{h}^{-1}$ for Ce/Co-coated AISI 441 exposed in a box furnace for 37 000 h, and $9.9 \cdot 10^{-6} \text{ mg cm}^{-2}\text{h}^{-1}$ for Ce/Co-coated AISI 441 exposed in a tube furnace for 1 000 h. The difference between the Cr evaporation rate of the two Ce/Co-coated materials that were exposed for different time lengths can be explained by the fact that long-term exposed samples had to be cut down for the Cr evaporation measurements, resulting in an uncoated and unexposed edge. This unexposed edge could result in slightly elevated Cr evaporation rates for pre-exposed Ce/Co-coated AISI 441 compared to unexposed Ce/Co-coated AISI 441. The steep decline for pre-exposed Ce/Co-coated AISI 441 was attributed to an accumulation of Cr in the Co_3O_4 scale during the stagnant air exposure in the box furnaces. This accumulated Cr evaporated in the first 100 hours of tube furnace exposure under high humid air flow. The Cr-evaporation rate stabilized after the complete removal of the accumulated Cr.

Area Specific Resistance Similar to mass gain, the ASR values also showed near parabolic behavior for Ce/Co-coated AISI 441, even up to 35 000 h of exposure (see Figure 4.10a), and the ASR values were extremely low after long-term exposure. The parabolic behavior of the ASR can easily be explained by the fact that the mass gain was due to the continuous grown Cr_2O_3 scale, which was the main contributor to the ASR (see Paper I). Similar to Paper I, the theoretical ASR could also be calculated for these oxide scales, however, due to the large variation not only in conductivity (see Chapter 2.3.3) but also in oxide scale thickness (see Table 4.2), the results of these calculations differed

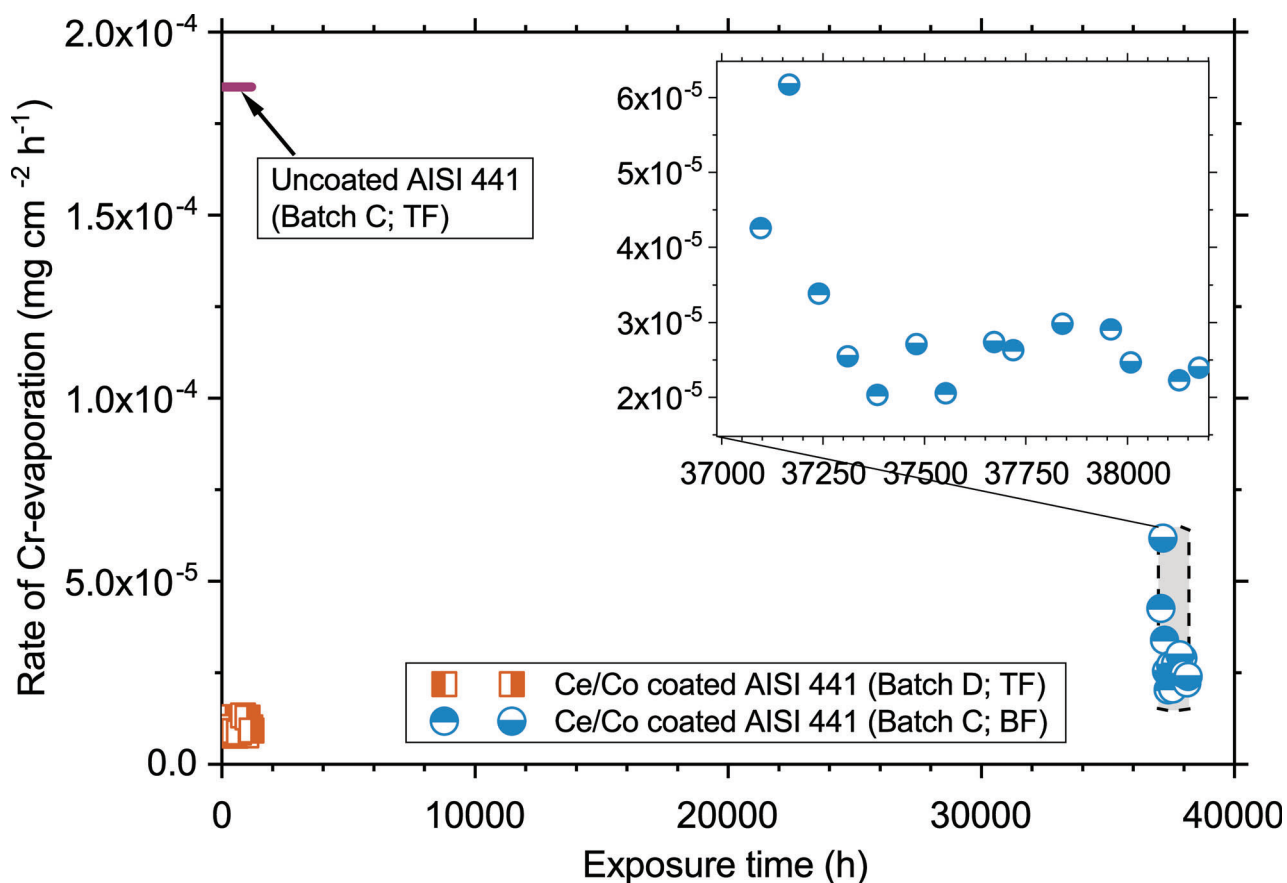


Figure 4.9: *Cr* evaporation rate as a function of time for uncoated AISI 441 or Ce/Co-coated AISI 441 exposed to air for up to 38 100 h at 800 °C. Different AISI 441 batches were used and are specified in brackets. Samples were exposed either discontinuously for 37 000 h in box furnaces (BF) by Sandvik Materials Technology or isothermally in tube furnaces (TF) at Chalmers. All *Cr* evaporation measurements were carried out in tube furnaces. Rates for uncoated AISI 441 were averaged over the exposure.

by several orders of magnitude: some matched well with the experimentally measured values, and others were much higher (see Paper III). In addition to the variation found in literature values and oxide thickness, doping effects through Fe or Mn contamination, as well as an oxygen partial pressure gradient through the oxide scale can greatly alter and specifically enhance the conductivity of an oxide scale. Both factors were present within thermally grown oxide scales and, thus, the conductivity of a pure Cr_2O_3 might not be representative for the conductivity of thermally grown Cr_2O_3 . Nevertheless, the good reproducibility of the experimentally measured ASR values over a large set of samples with relatively small error bars and their parabolic behavior strongly suggest high accuracy for the reported ASR measurements. The credibility of these ASR values can be verified by the behavior of the ASR during cooling (see Figure 4.10b). The linear behavior verified semi-conducting behavior, which is described by Equation 2.29. The average activation energy of all conducted measurements within the scope of this investigation was found to be 0.51 eV (slope of the straight line in Figure 4.10a). This experimental value is in good agreement with the median literature value, found over many different publications, for the activation energy of the conductivity of Cr_2O_3 below 850 °C (see Chapter 2.3.3).

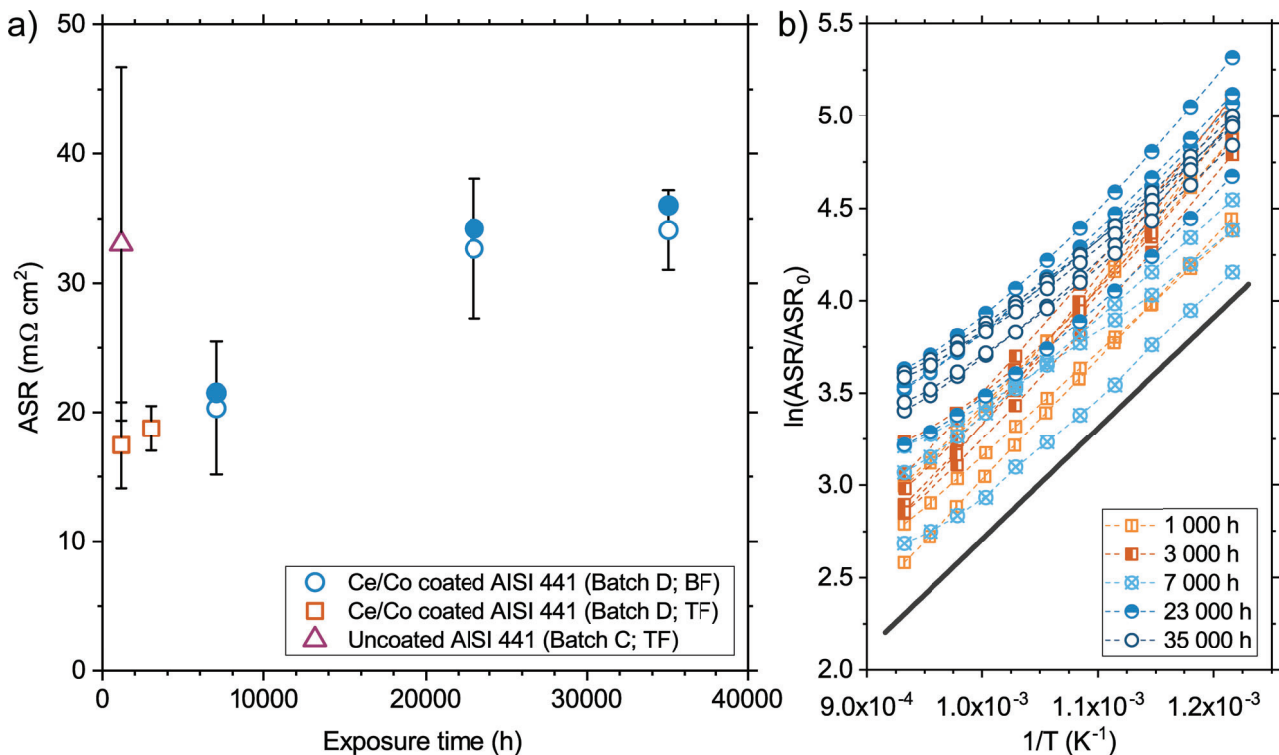


Figure 4.10: a) ASR as a function of exposure length for uncoated or Ce/Co-coated AISI 441 that was exposed to air up to 35 000 h at 800 °C. Different AISI 441 batches were used and are specified in brackets. Samples were exposed either discontinuously in box furnaces (BF) by Sandvik Materials Technology or isothermally in tube furnaces (TF) at Chalmers. Empty symbols indicate average values with their respective standard deviation (error bars). Filled symbols indicate samples that were used for microstructural analysis. b) Arrhenius plot for the ASR of all Ce/Co-coated AISI 441 samples. The slope of the grey line depicts the average activation energy.

The long-term stability of Ce/Co-coated AISI 441 was confirmed in this investigation with regard to good Cr retention even after 38 000 h of exposure at 800 °C, low ASR values after 35 000 h of exposure, and near parabolic mass gain throughout the entire period of exposure. However, low Cr content after 35 000 h (11.8 wt%) indicates that material failure might occur soon, but Ce/Co coated AISI 441 remained protective even after 38 100 h of exposure.

4.2 The Dual Atmosphere Effect

Detailed information on the dual atmosphere effect is given in Chapter 2.3.4. To investigate the dual atmosphere effect, different parameters and how they affected the formation of breakaway corrosion on the air-facing side were examined: the exposure temperature, the importance of pre-oxidation, and the influence of material thickness and surface treatment. By understanding the influence of these parameters on the dual atmosphere effect, the difference found in the literature for the severity and even existence of the dual atmosphere effect is explained, and conclusions are drawn on the dual atmosphere mechanism.

4.2.1 Temperature Dependence

Previous work by *Alnegren* et al. [31, 32] has shown that the dual atmosphere effect for AISI 441 is severe at 600 °C, and no significant effect was found at 700 and 800 °C. However, temperatures below 600 °C were not examined by those authors, and it remains unclear if the dual atmosphere effect was also present below 600 °C. The previous work by *Alnegren* et al. [31, 32] also disregarded the potential influence of a pre-formed oxide scale on the dual atmosphere effect. Therefore, the present research examined exposures of pre-oxidized and non-pre-oxidized AISI 441 to dual or single atmosphere for 336 h at 500 °C, 550 °C, 600 °C, 650 °C, 700 °C, and 800 °C. By explaining the results with the Wagnerian theory (see Chapter 2.2.4), conclusions on the mechanism of the dual atmosphere effect could be drawn.

Protective behavior in single atmosphere was found for all temperatures and regardless if a pre-oxidation step was implemented or not. For further analysis of single atmosphere exposed samples, the reader is referred to [31, 32]. Only dual atmosphere exposed samples will be discussed below.

Non-pre-oxidized AISI 441 Non-pre-oxidized AISI 441 that was exposed to dual atmosphere for 336 h showed protective behavior only at 500 °C; an Fe-rich oxide scale covered the entire surface of AISI 441 at all other temperatures (see Figure 4.11). The surface morphology of this Fe-rich oxide scale changed from whiskers at 600 °C and 650 °C to undulated porous oxide at higher temperatures.

The cross-sections for non-pre-oxidized and dual atmosphere exposed samples suggested that the thickest oxide scale had formed at 600 °C, however, there seemed to be little difference between samples exposed at 550 °C or 600 °C (see Figure 4.12). The phases were identified using EDX (see Paper IV) and previous knowledge [31, 32]. An internal oxidation zone (IOZ) was formed at and below 600 °C, and this zone is believed to be

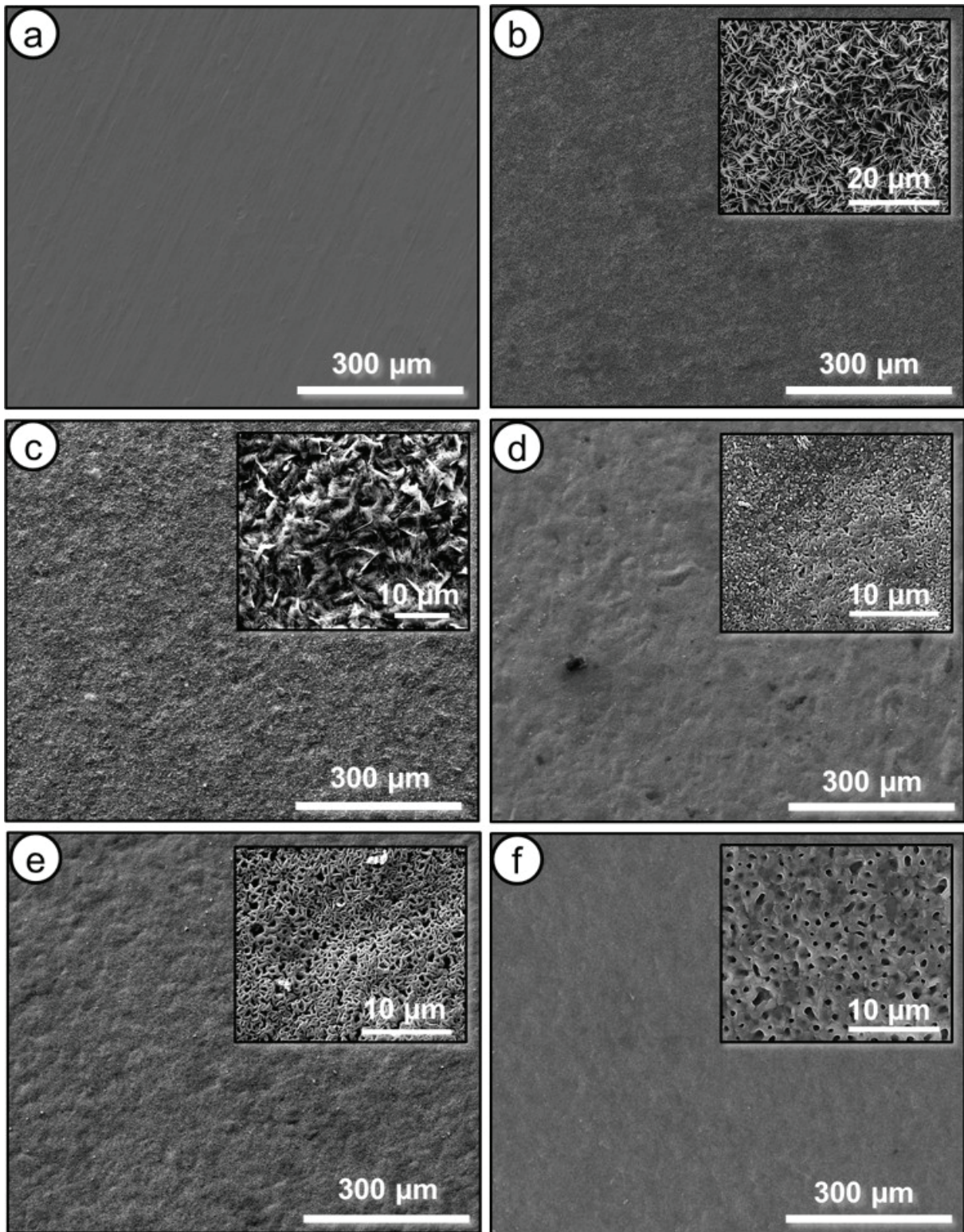


Figure 4.11: *SEM micrographs of the air-facing side of AISI 441 exposed to dual atmosphere for 336 h at a) 500 °C, b) 550 °C, c) 600 °C, d) 650 °C, e) 700 °C, and f) 800 °C. All samples were non-pre-oxidized. Except for a, which was covered in a protective oxide scale, all other samples were covered in Fe-rich oxide.*

a mixture between unreacted metal, and Cr_2O_3 [31]. Cr_2O_3 agglomerates had formed within the IOZ, and to some extent, a thin Cr_2O_3 scale had formed between the IOZ and the steel substrate. No IOZ was found at temperatures above 600°C , and instead, a continuous and increasingly thicker Cr_2O_3 scale had formed between the steel substrate and the $(\text{Cr,Fe})_3\text{O}_4$ at higher temperatures.

Pre-oxidized AISI 441 Pre-oxidized AISI 441 that was exposed to dual atmosphere for 336 h was completely covered in Fe-rich oxide at 600°C , while only protective oxide was found on the entire sample surface at 500°C and 800°C . The surface was partially covered in Fe-rich oxide nodules at the intermediate temperatures, 550°C , 650°C , and 700°C , and partially covered in a protective oxide scale (see Figure 4.13). The nodules were smaller and fewer at 550°C than at 650°C and 750°C . This showed that the dual atmosphere effect was most severe at 600°C .

The microstructure of the Fe-rich oxides for pre-oxidized samples (see Figure 4.14) resembled that of the non-pre-oxidized samples (see Figure 4.12), and phases were again identified using EDX maps (see Paper IV) and previous knowledge. Similar to the non-pre-oxidized samples, the pre-oxidized samples also showed the presence of IOZ and agglomerated Cr_2O_3 below the $(\text{Cr,Fe})_3\text{O}_4$ scale and sporadically a thin discontinuous Cr_2O_3 layer between the steel substrate and the IOZ at 550°C and 600°C . However, with the exception of the sample exposed at 600°C , all other pre-oxidized samples had large areas that were covered by a protective oxide scale. This protective oxide scale consisted of a $(\text{Cr,Mn})_3\text{O}_4$ scale on top of a Cr_2O_3 scale. The duality of the protective oxide scale was clearly differentiated for temperatures at and above 650°C but was too thin at 550°C .

The results showed that 600°C is the temperature at which the most severe dual atmosphere effect is found. No dual atmosphere effect was found at 500°C . However, the dual atmosphere effect was present at the opposite end of the temperature scale, 800°C , but only for non-pre-oxidized samples. This indicates that the dual atmosphere effect was present at 800°C , but that it could be impeded by the presence of a pre-formed protective oxide scale. These results are in agreement with *Alnegren et al.* [32], who have reported no dual atmosphere effect for pre-oxidized AISI 441 at 800°C . However, those authors did not examine non-pre-oxidized AISI 441.

The effect of pre-oxidation on the dual atmosphere effect can partly explain the discrepancy in the literature. This discrepancy will only be discussed in full in Chapter 4.2.5.

Solving the Dual Atmosphere Mechanism The temperature study can shine some light on the dual atmosphere mechanism. As mentioned in Chapter 2.3.4, this mechanism is to-date unclear, and the only consensus in the literature is that hydrogen is to blame. However, the effects of hydrogen are unknown. The following discussion aims to solve this and is in large part based on the Wagnerian theory discussed in Chapter 2.2.4 and Equations 2.23 and 2.24. These equations define the critical Cr content that is needed to maintain a protective oxide scale. Fe will be preferentially oxidized and breakaway oxidation will occur below this content.

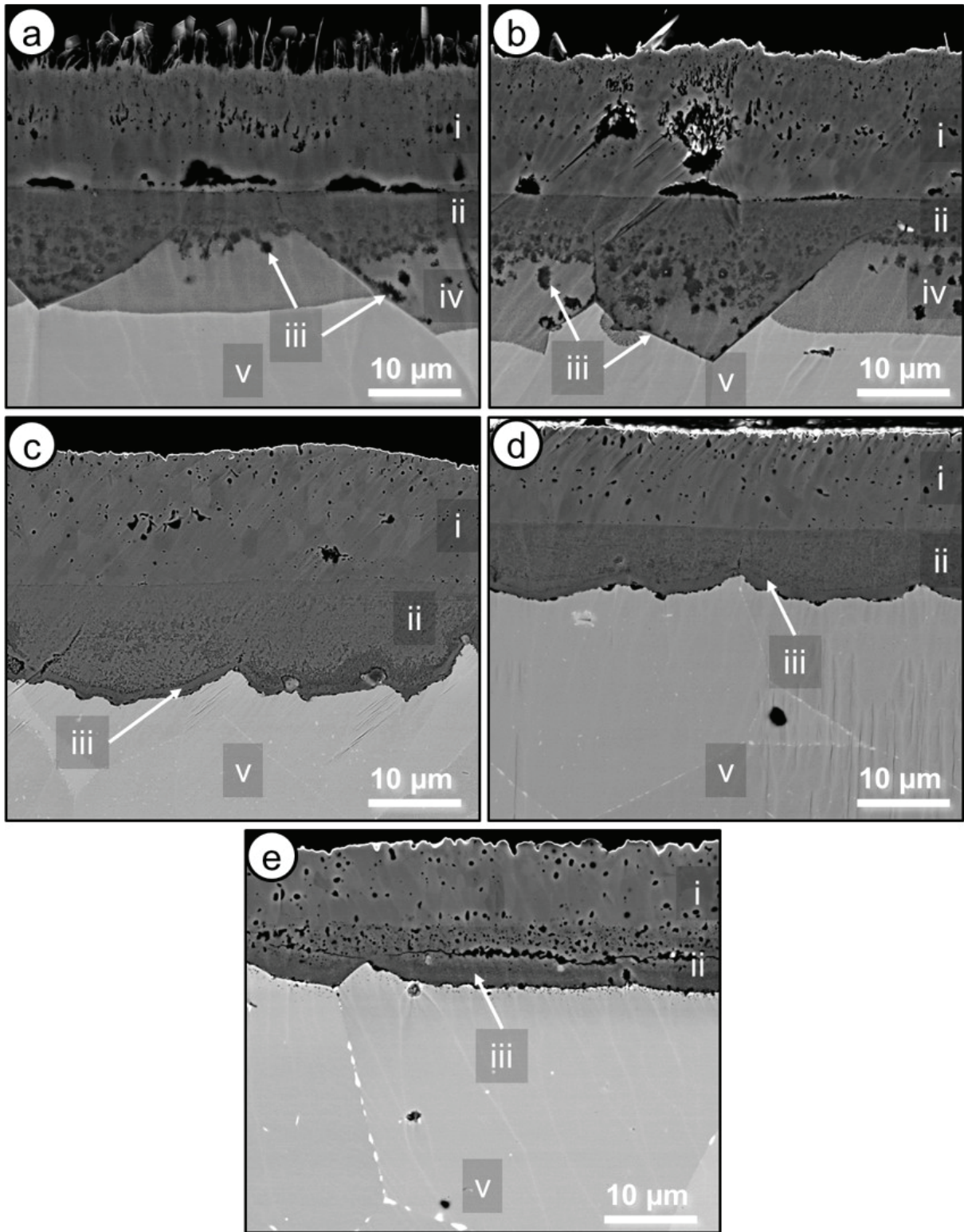


Figure 4.12: Backscattered SEM micrographs for BIB milled cross-sections of the air-facing side of AISI 441 exposed to dual atmosphere for 336 h at a) 550 °C, b) 600 °C, c) 650 °C, d) 700 °C, and e) 800 °C. All samples were non-pre-oxidized. Using EDX and previous knowledge, the phases were identified as i) Fe_2O_3 , ii) $(\text{Cr,Fe})_3\text{O}_4$, iii) Cr_2O_3 , iv) IOZ, and v) steel substrate.

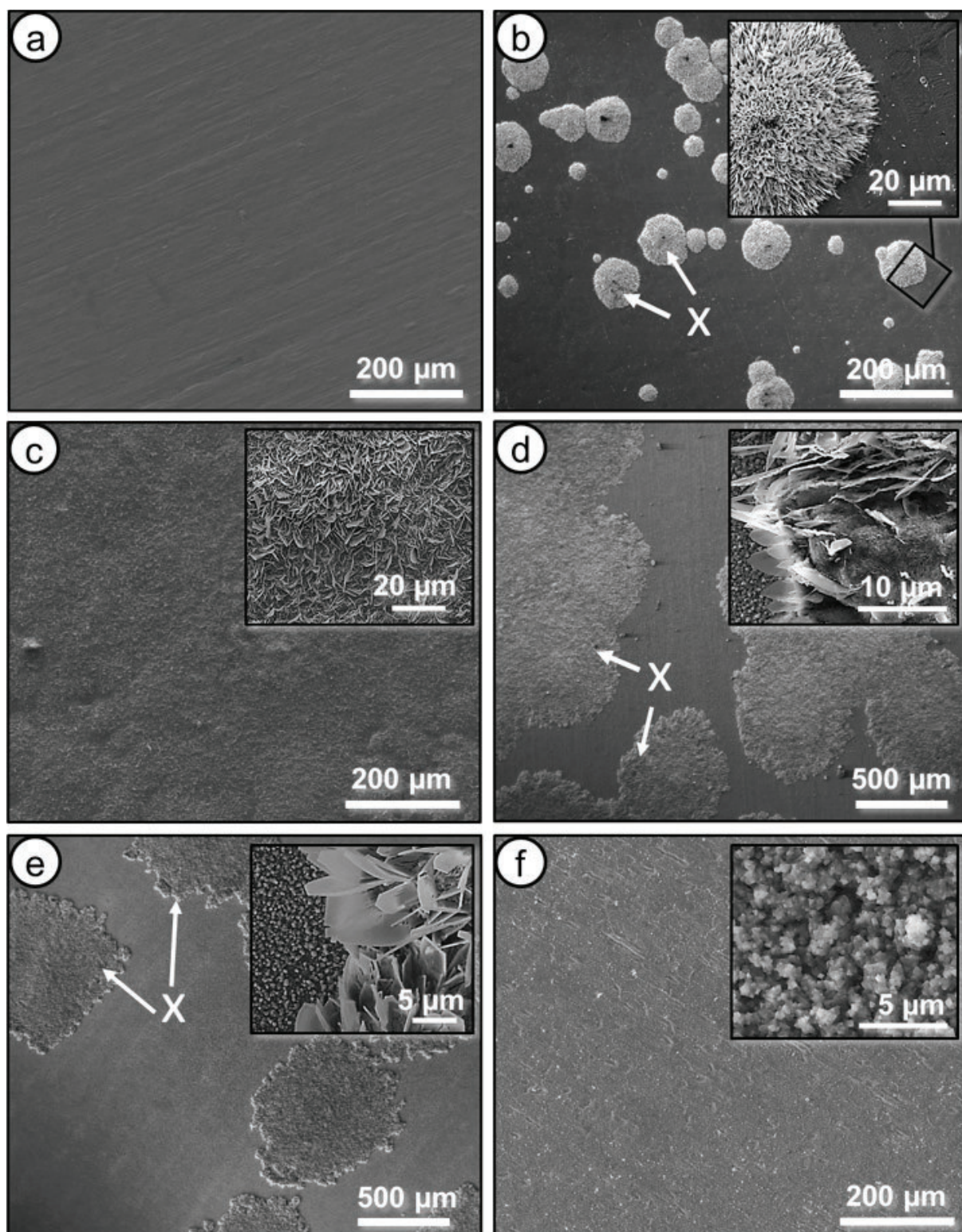


Figure 4.13: SEM micrographs of the air-facing side of AISI 441 exposed to dual atmosphere for 336 h at a) 500 °C, b) 550 °C, c) 600 °C, d) 650 °C, e) 700 °C, and f) 800 °C. All samples were pre-oxidized for 20 min prior to dual atmosphere exposure. a) and f) were covered with a protective oxide scale, c) was covered with an Fe-rich oxide scale, and the other samples had both Fe-rich oxide nodules (marked with X) and a protective oxide scale.

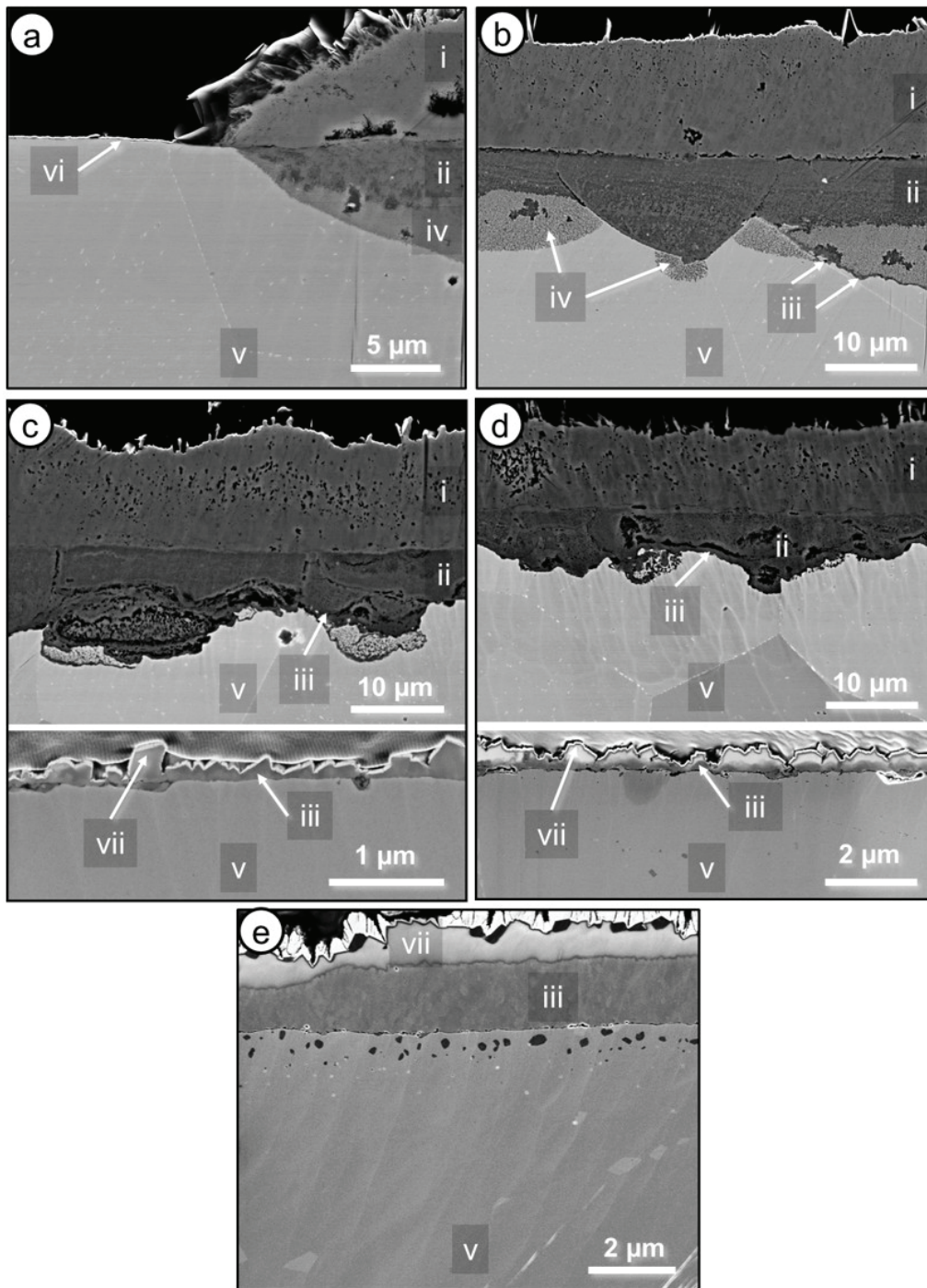


Figure 4.14: Backscattered SEM micrographs for BIB milled cross-sections of the air-facing side of AISI 441 exposed to dual atmosphere for 336 h at a) 550 °C, b) 600 °C, c) 650 °C, d) 700 °C, and e) 800 °C. All samples were pre-oxidized for 20 min prior to dual atmosphere exposure. Two micrographs are shown for samples c) and d), which both had large areas that were covered by a protective oxide scale and large areas that were covered by Fe-rich oxide scale. Using EDX and previous knowledge, the phases were identified as i) Fe_2O_3 , ii) $(\text{Cr},\text{Fe})_3\text{O}_4$, iii) Cr_2O_3 , iv) IOZ, v) steel substrate, vi) protective oxide scale, and vii) $(\text{Cr},\text{Mn})_3\text{O}_4$.

It was assumed that N_{Cr}^{crit1} (see Equation 2.23) can be used to describe non-pre-oxidized samples, because this parameter describes a case with no preformed oxide scale. On the other hand, N_{Cr}^{crit2} (see Equation 2.24) describes when a preformed oxide scale fails and can, therefore, be used for pre-oxidized samples. For the present system, e.g. the oxidation of Fe-Cr alloy, N_{Cr}^{crit1} and N_{Cr}^{crit2} were calculated using Equations 2.23 and 2.24, respectively. The calculated values predict at which minimum Cr concentration protective behavior of the alloy can be expected. For these calculations, literature values were chosen for the parameters $N_O^{(s)}$, D_O , \tilde{D}_{Cr} , and k_p (see Table 4.3). Paper IV discusses why certain literature values for these parameters were chosen over others, which will not be discussed here. The literature values for $N_O^{(s)}$ and D_O reported by *Takada et al.* [214, 215] were used. The Cr diffusion reported by *Williams et al.* [216] was chosen for \tilde{D}_{Cr} , and the k_p values were taken and extrapolated from *Falk-Windisch et al.* [117].

Table 4.3: Literature values required to calculate N_{Cr}^{crit1} and N_{Cr}^{crit2} according to Equations 2.23 and 2.24, respectively.

T (°C)	$N_O^{(s)}$ [214, 215]	D_O (m ² s ⁻¹) [214, 215]	\tilde{D}_{Cr} (m ² s ⁻¹) [216]	k_p (m ² s ⁻¹) [117]	N_{Cr}^{crit1}	N_{Cr}^{crit2}
500	$3.6 \cdot 10^{-8}$	$2.9 \cdot 10^{-13}$	$9.7 \cdot 10^{-20}$	$1.2 \cdot 10^{-23}$	0.127	0.007
550	$9.5 \cdot 10^{-8}$	$6.5 \cdot 10^{-13}$	$7.0 \cdot 10^{-19}$	$1.4 \cdot 10^{-22}$	0.116	0.009
600	$2.3 \cdot 10^{-7}$	$1.3 \cdot 10^{-12}$	$4.0 \cdot 10^{-18}$	$1.3 \cdot 10^{-21}$	0.106	0.011
650	$4.9 \cdot 10^{-7}$	$2.5 \cdot 10^{-12}$	$1.9 \cdot 10^{-17}$	$5.2 \cdot 10^{-20}$	0.099	0.013
700	$9.9 \cdot 10^{-7}$	$4.5 \cdot 10^{-12}$	$8.0 \cdot 10^{-17}$	$1.0 \cdot 10^{-18}$	0.092	0.015
800	$3.3 \cdot 10^{-6}$	$1.2 \cdot 10^{-11}$	$9.0 \cdot 10^{-16}$	$5.5 \cdot 10^{-17}$	0.082	0.021
900	$8.9 \cdot 10^{-6}$	$2.7 \cdot 10^{-11}$	$6.7 \cdot 10^{-15}$	$3.7 \cdot 10^{-16}$	0.074	0.027

It should be noted that the equation used for the non-pre-oxidized samples (see Equation 2.23) underestimates the actual Cr content needed to avoid Fe oxidation. This is due to the fact that the equation was formulated based on the assumption that only Cr would form a thermodynamically stable external oxide scale, and the equation describes at what critical Cr concentration a switch from internal oxidation to external oxidation occurs [108]. *Gesmundo et al.* [217] have shown that the critical Cr content is higher if Fe can also form a thermodynamically stable external oxide scale. These conditions are prevalent in dual atmosphere and, therefore, the calculated $N_{Cr}^{crit1}(cal)$ is lower than the actual $N_{Cr}^{crit1}(act)$. Nevertheless, the behavior of N_{Cr}^{crit1} (see Table 4.3) is in agreement with the rather high activation energy of Cr diffusivity, on average 210 kJ mol⁻¹ [216]. This results in an inverse temperature dependency, and, thus, lower temperatures require more Cr content than higher temperatures. This behavior was found in all non-pre-oxidized samples in the present study, which showed an inverse behavior between 600 °C and 800 °C. This inverse behavior can be detected by the decrease in the thickness of the entire oxide scale, including the IOZ from 600 °C to 800 °C. Additionally, internal oxidation of Cr was detected in the IOZ at 550 °C and 600 °C, but not at higher temperatures.

The behavior of N_{Cr}^{crit2} in contrast, was the reverse of the behavior of N_{Cr}^{crit1} , but the increase in the N_{Cr}^{crit2} with increasing temperature was much less pronounced than the

change that occurred for N_{Cr}^{crit1} . Similar to N_{Cr}^{crit1} , the calculation of N_{Cr}^{crit2} is also based on the assumption that only Cr would form a thermodynamically stable external oxide scale. However, under most exposure conditions, Fe can also form a thermodynamically stable external oxide scale, and this results in an increase in the N_{Cr}^{crit2} . Studies [138, 218, 219] have shown that the calculated N_{Cr}^{crit2} is often underestimated by 8 to 10 wt% and, therefore, this correction factor can be implemented on top of the N_{Cr}^{crit2} calculated in Table 4.3. Because the activation energy for oxide scale growth ($E_A(k_p) = 261 \text{ kJ mol}^{-1}$ [220]) is very similar to that of Cr diffusion ($E_A(D_{Cr}) = 210 \text{ kJ mol}^{-1}$ [216]), N_{Cr}^{crit2} is very weakly temperature dependent.

The key to solving the mechanism of the dual atmosphere effect is understanding which parameter in Equations 2.23 and 2.24 is affected by hydrogen. In theory, three parameters can be altered by the presence of hydrogen: the oxygen permeability $N_O^{(s)} D_O$, the Cr_2O_3 growth rate k_p , and the Cr diffusivity \tilde{D}_{Cr} .

One popular theory on the mechanism of the dual atmosphere effect is the increase in oxygen permeability caused by the presence of hydrogen, which, according to *Essuman et al.* [190], is caused by interstitial hydrogen atoms expanding the Fe lattice and, thus, increasing oxygen diffusivity. However, theoretical considerations carried out in the present work showed that this is not plausible. For breakaway oxidation to occur at 600°C and 700°C , hydrogen would have to increase oxygen permeability by at least a factor of 3 or 4 to increase N_{Cr}^{crit1} above the Cr content of AISI 441 (just below 18 wt%). This massive increase in oxygen permeability would lead to a doubling of the IOZ thickness, which has not been reported [138, 221].

Similar considerations can be applied to k_p with an even more obvious result. Even if k_p is increased by an order of magnitude, N_{Cr}^{crit2} will remain below 18 wt%. Additionally, neither *Alnegren et al.* [32] nor *Bredvei Skilbred et al.* [180] have seen an increase in oxide scale thickness between dual and single atmosphere.

These considerations strongly suggest that the only plausible parameter that hydrogen could influence is Cr diffusion. Even though *Ani et al.* [222] have shown that hydrogen does not affect Cr diffusion, their study was carried out on coarse-grained material and, thus, focused on lattice diffusion and neglected the contribution of grain boundary diffusion. Grain boundary (GB) diffusion is more relevant at lower temperatures than at higher ones, and lattice diffusion becomes more relevant at higher temperatures (see Chapter 2.2.3). This could explain the inverse temperature behavior found for the dual atmosphere effect. If hydrogen had blocked the grain boundary diffusion paths, the effect would be more pronounced at lower temperatures than at higher temperatures.

The effects of hydrogen on Cr diffusion can again be verified by theoretical considerations. If \tilde{D}_{Cr} is decreased by only a factor of five for the non-pre-oxidized samples (Criterion 1; see Equation 2.23), breakaway oxidation would occur. For the pre-oxidized samples (Criterion 2; see Equation 2.24), a decrease in \tilde{D}_{Cr} by approximately two orders of magnitude would lead to the formation of breakaway oxidation. Even though that appears to be a significant decrease, it is approximately the difference between $D_{GB}(600^\circ\text{C})$ and $D_{GB}(700^\circ\text{C})$.

These considerations have not yet been experimentally proven. However, the theoretical considerations discussed above, show that it can be excluded that hydrogen affects the oxygen permeability or the oxide scale growth rate. Instead it is near certain that hydrogen

affects the Cr diffusion along the grain boundaries.

Nevertheless, even though this explains the inverse temperature effect observed from 600 °C to 800 °C, the theory presented here does not elucidate why no dual atmosphere effect was found at 500 °C, and why less breakaway oxidation had formed at 550 °C than at 600 °C. One suggestion for this is that the purity of the Cr₂O₃ scale at lower temperatures is not as important to maintain protective behavior of the oxide scale. The miscibility of Cr₂O₃ and Fe₂O₃ often leads to the inclusion of increased amounts of Fe into the Cr₂O₃ scale with decreased exposure temperature. *Segerdahl et al.* [223] have found that a near pure Fe₂O₃ scale had formed at 500 °C on 11 wt% Cr-containing steel without resulting in a non-protective, i.e. fast growing, oxide scale. This result strongly suggests that the protective behavior found at 500 °C, and to a lesser extent and 550 °C, in dual atmosphere is because less Cr is needed to maintain a protective oxide scale at these temperatures than at higher ones. This means that the Cr diffusion was substantially decreased by the presence of hydrogen even at 550 and 500 °C. However, much less Cr was required to maintain the protective behavior of AISI 441 at those temperatures.

4.2.2 Pre-oxidation and its Influence on the Dual Atmosphere Effect

The preceding chapter showed that pre-oxidation influences the dual atmosphere effect. This can be relevant for real applications, as fuel cells are typically sintered in air before their first start-up, meaning a pre-oxidation step is the norm. Therefore, the beneficial effect of a pre-oxidation step will be discussed in the following with regard to two different parameters: pre-oxidation time, i.e. do longer pre-oxidation times delay the onset of breakaway oxidation, and pre-oxidation location, i.e. does the beneficial effect result from the pre-oxidation scale on the fuel-facing side or the air-facing side.

Pre-oxidation Time A correlation between the pre-oxidation time and the onset of breakaway oxidation was found for AISI 441 in dual atmosphere (see Figure 4.15). This dependence was expressed by longer pre-oxidation times that led to a delay in the formation of breakaway oxidation. Accelerated testing could be, within limitations (e.g. PVD coatings might need longer pre-oxidation times to fully oxidize), possible with shorter pre-oxidation times.

In addition to visual inspection, scanning electron microscopy also confirmed that longer pre-oxidation times resulted in greater corrosion resistance against the dual atmosphere effect (see Figure 4.16). The air-facing side of non-pre-oxidized and 11 min pre-oxidized AISI 441 samples was covered in a thick Fe-rich oxide after 1 000 h of exposure. Iron-rich nodules had formed on samples pre-oxidized for 45 and 180 min, but large areas remained covered in protective oxide. Very few isolated and tiny Fe-rich oxide nodules were found on the surface of AISI 441 pre-oxidized for 280 min.

The microstructure of the Fe-rich oxide that had formed on the air-facing side of some samples was like the microstructure found for the Fe-rich oxide that had formed on the AISI 441 sample pre-oxidized for 20 min, which was exposed to dual atmosphere at 600 °C for 336 h (see Figure 4.14b). The AISI 441 sample pre-oxidized for 11 min (see Figure 4.17), for example, showed the formation of a roughly 37 μm thick breakaway

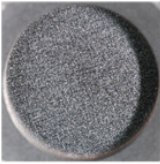
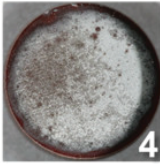
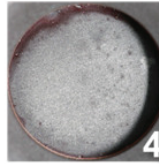
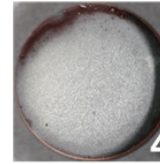
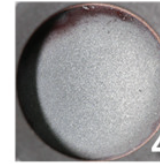
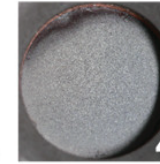
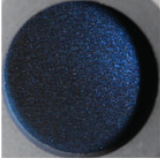
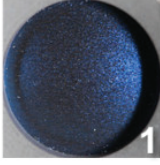
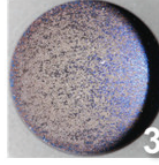
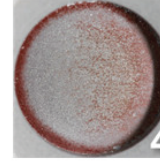
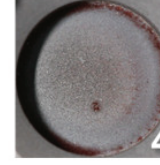
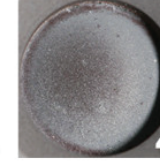
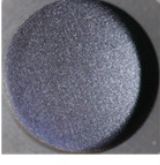
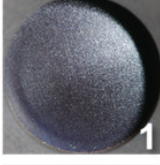
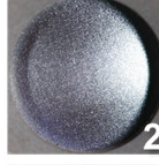
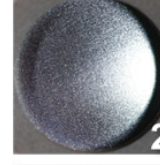

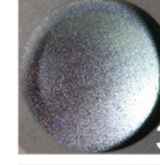
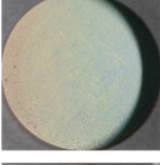
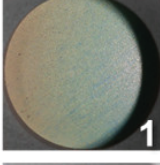
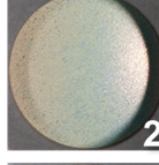
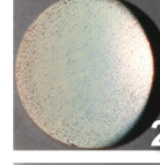
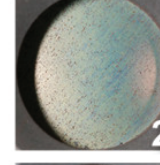
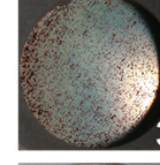
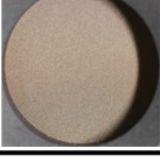
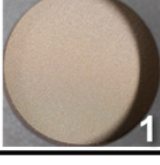
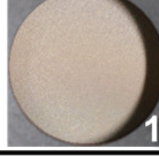
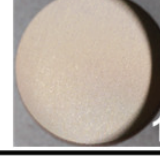
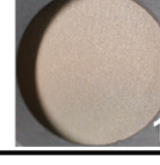
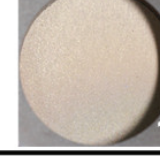
$t_{\text{pre-oxidation}} \backslash t_{\text{exposure}}$	0 h	24 h	168 h	500 h	730 h	1 000 h
0 min						
11 min						
45 min						
180 min						
280 min						

Figure 4.15: Photographs of the air-facing side of AISI 441 taken during discontinuous dual atmosphere exposure at 600 °C. The numbers at the bottom of each picture rate the progress of corrosion. They are defined as follows: 1 = only protective behavior present, 2 = mostly protective behavior present, 3 = mostly corroded surface, and 4 = completely corroded surface.

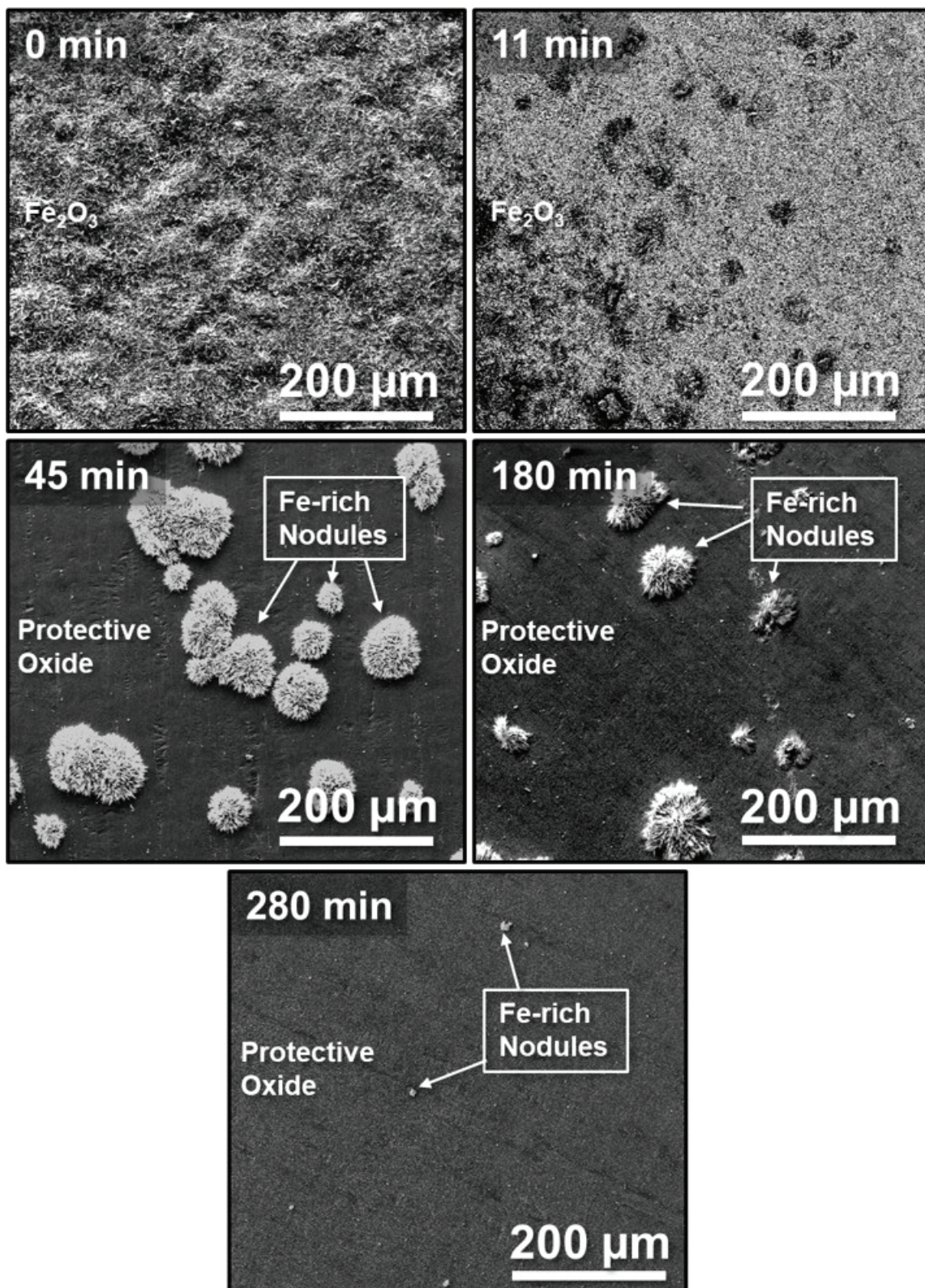


Figure 4.16: SEM micrographs of the air-facing surface of AISI 441 exposed to dual atmosphere for 1000 h at 600 °C. Five different pre-oxidation times were employed: 0 min, 11 min, 45 min, 180 min, and 280 min.

oxidation layer after 1 000 h of dual atmosphere exposure. This layer consisted of a top hematite layer below which a mixed $(\text{Fe,Cr})_3\text{O}_4$ spinel had formed with an IOZ under the spinel. More detailed microstructural investigations on the iron-rich nodules formed on the air-facing side in dual atmosphere can be found in Paper IV, Paper V, and [31, 32, 224].

A thick Fe-rich oxide had also formed on the hydrogen-facing side for some samples, in addition to the air-facing side, namely for the non-pre-oxidized and 11 min pre-oxidized samples (see Figure 4.17). Further research is required to analyze this oxide and its implications. Longer pre-oxidation times than 11 min all resulted in a protective Cr-rich oxide scale on the hydrogen-facing side, even after 1 000 h of dual atmosphere exposure.

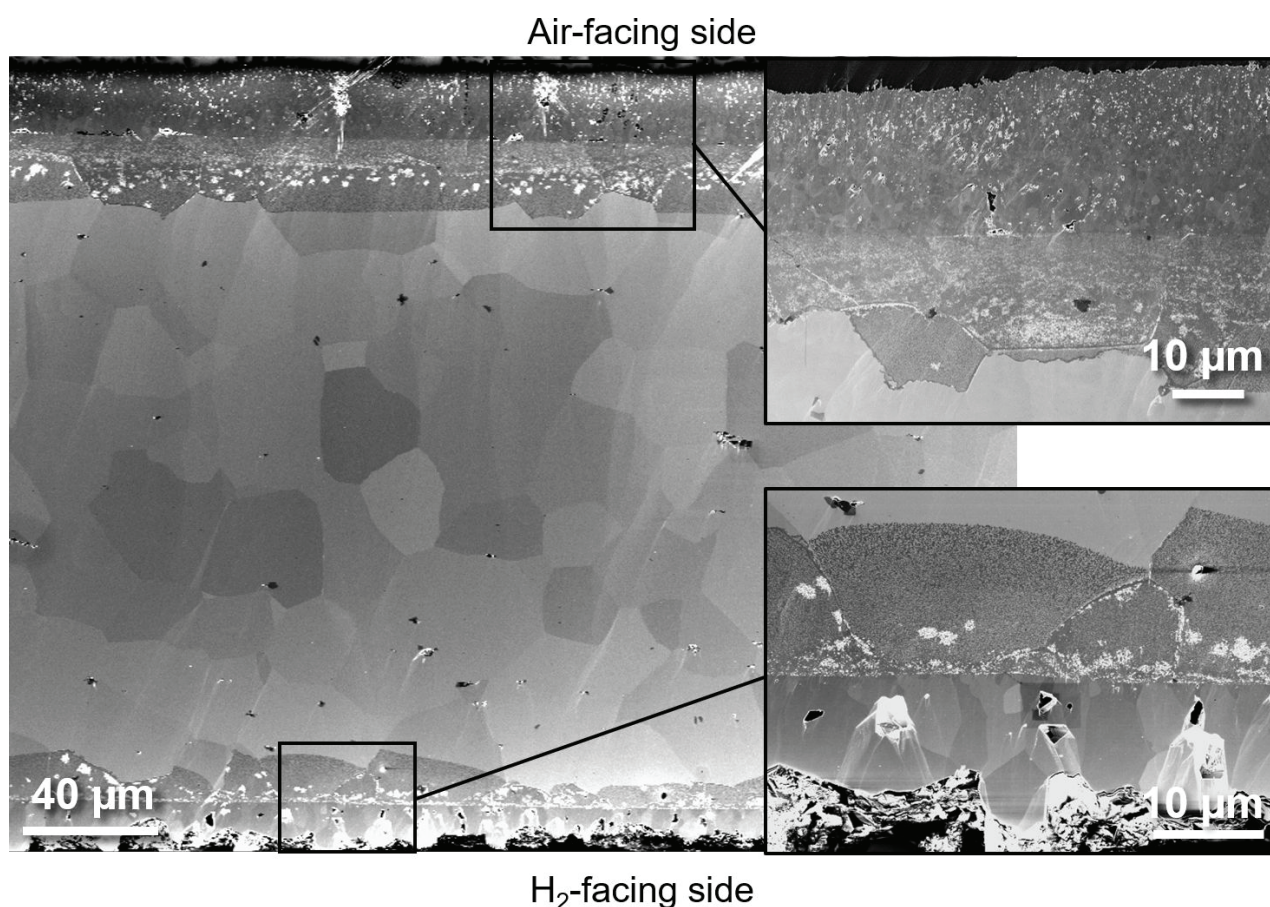


Figure 4.17: SEM micrograph of the BIB milled cross-section of AISI 441 that was pre-oxidized for 11 min and, subsequently, discontinuously exposed to dual atmosphere for 1 000 h at 600 °C.

The 5 h pre-oxidized AISI 441 sample still showed protective behavior after 1 000 h of exposure. However, a separate study conducted within the scope of this work showed that this material had formed a substantial amount of Fe-rich oxide nodules on the surface of the samples after 3 000 h (see Figure 4.18 and Figure 4.19a). This suggests that even though longer pre-oxidation times delay the onset of breakaway oxidation, longer pre-oxidation times do not prevent breakaway oxidation.

The one-sided Ce/Co-coated AISI 441 sample that was pre-oxidized for 5 h showed

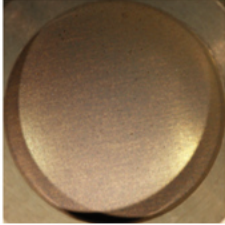
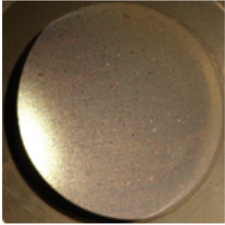
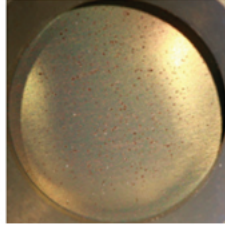
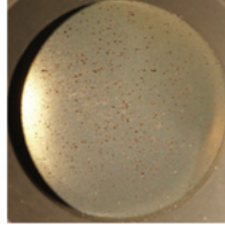
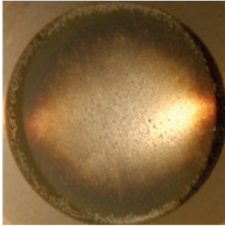
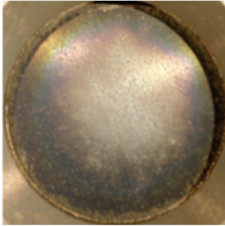
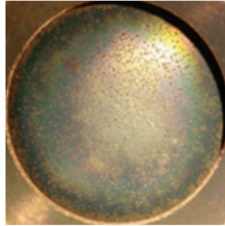
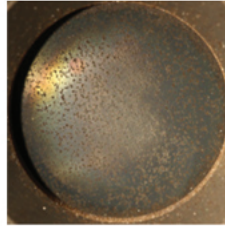
t_{exposure} Material	500 h	1 000 h	2 000 h	3 000 h
AISI 441				
Ce/Co coated AISI 441*				

Figure 4.18: Photographs of the air-facing side of uncoated AISI 441 and one-sided (air-side) Ce/Co-coated AISI 441. Both samples were pre-oxidized for 5 h at 800 °C using a heating ramp of 1 °C min⁻¹ and subsequently exposed to dual atmosphere discontinuously for 3 000 h at 600 °C.

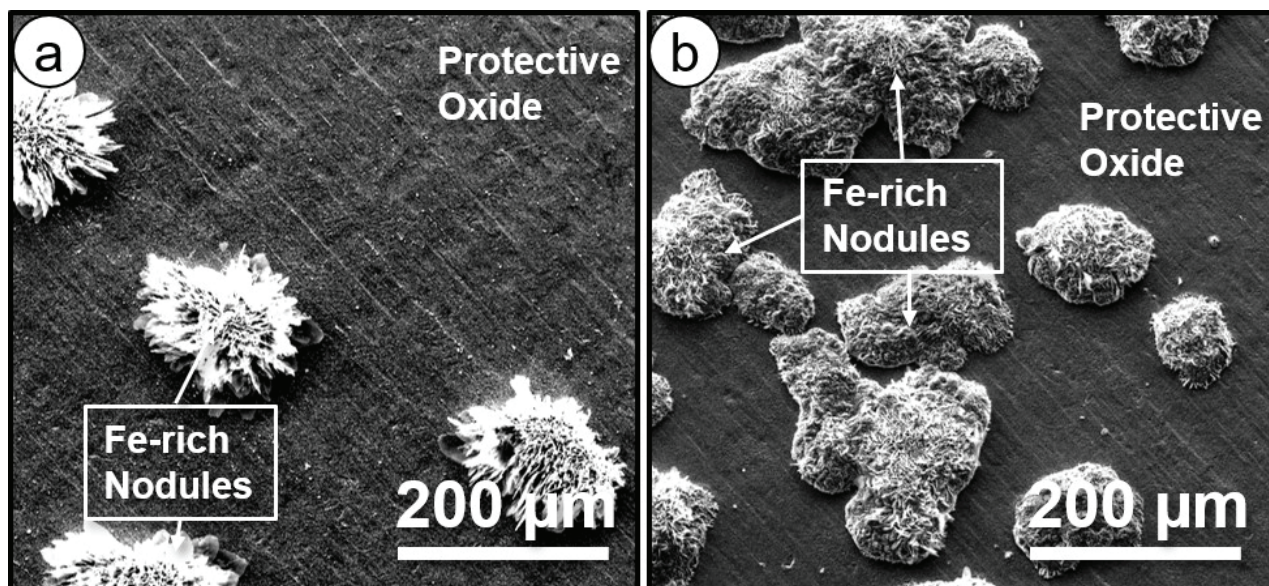


Figure 4.19: SEM micrographs of the air-facing side of uncoated AISI 441 (a) and one-sided (air-side) Ce/Co-coated AISI 441. Both samples were pre-oxidized for 5 h at 800 °C using a heating ramp of 1 °C min⁻¹ and subsequently exposed for 3 000 h at 600 °C to dual atmosphere.

the formation of breakaway oxidation after 3 000 h of dual atmosphere exposure (see Figure 4.18 and Figure 4.19b). The extent of Fe-rich oxide nodules that had formed on this sample seemed to be even greater than that of the uncoated AISI 441 sample pre-oxidized for 5 h. The formation of breakaway oxidation on a Ce/Co-coated AISI 441 sample verified that an increase in Cr evaporation caused by hydrogen diffusing through the material is not the cause of the dual atmosphere effect. This theory had already been partially excluded by *Alnegren* et al. [32], who have shown that the dual atmosphere effect also occurs under dry conditions. The present work strengthens that claim, because an oxidized Co coating should mitigate Cr evaporation (see Chapter 2.3.2). Nevertheless, breakaway oxidation had still formed on the Ce/Co-coated AISI 441 that was pre-oxidized for 5 h, to a similar or even greater extent than for the uncoated material, which was exposed under the same conditions.

Pre-oxidation Location The beneficial effect of pre-oxidation was demonstrated in the previous chapter. However, what remained unclear from this work was if the beneficial effect is due to the oxide layer present on the air-facing side, which leads to a decelerated oxidation rate, or if it is due to the oxide layer on the fuel-facing side, which mitigates hydrogen ingress into the alloy. The latter theory was proven true (see Figure 4.20 and 4.21). It was found that the pre-oxidation layer on the hydrogen-facing side acts as a barrier against hydrogen ingress. No breakaway oxidation on the air-facing side had formed on samples that had a pre-oxidation scale on the hydrogen-facing side, regardless if the material had been polished or ground. This is in agreement with *Kurokawa* et al. [184, 189], who have shown that hydrogen permeation through Cr_2O_3 is substantially lower than through ferritic stainless steels. Those authors reported a 94 % decrease in hydrogen permeation for a 760 nm thick oxide scale (on one side of an alloy) compared to the bare alloy.

These results suggest that a hydrogen barrier coating on the hydrogen-facing side of the interconnect should mitigate the dual atmosphere effect, and, consequently, this is the next step on the application level. Research related to nuclear fusion and hydrogen-based energy sectors focuses on hydrogen permeation barriers; oxides, nitrides, and pure metals often have good hydrogen permeation barrier properties [225].

4.2.3 Influence of Material Thickness

It was shown that Cr_2O_3 is an effective barrier against hydrogen permeation, however, the question that remains, is if also the steel itself decelerates hydrogen diffusion. The present work found that also steel has a hydrogen barrier effect, even though this effect seems to be comparatively weak (see Figure 4.22 and Figure 4.23). Thicker samples were covered to a lesser extent with Fe-rich oxide nodules than thinner samples. This effect is not due to a Cr depletion of the bulk material, because the chosen conditions, i.e. a short pre-oxidation time, 20 min, and a short dual atmosphere exposure length, 336 h, at low temperature, 600 °C, were not expected to result in a depletion of Cr in the material. Thus, the conclusion is that hydrogen diffusion is decelerated through a barrier function of the FSS. This is in agreement with *Kurokawa* et al. [184, 189], who have estimated the hydrogen permeation coefficient in iron to be 10 000 times greater than that of Cr_2O_3 .

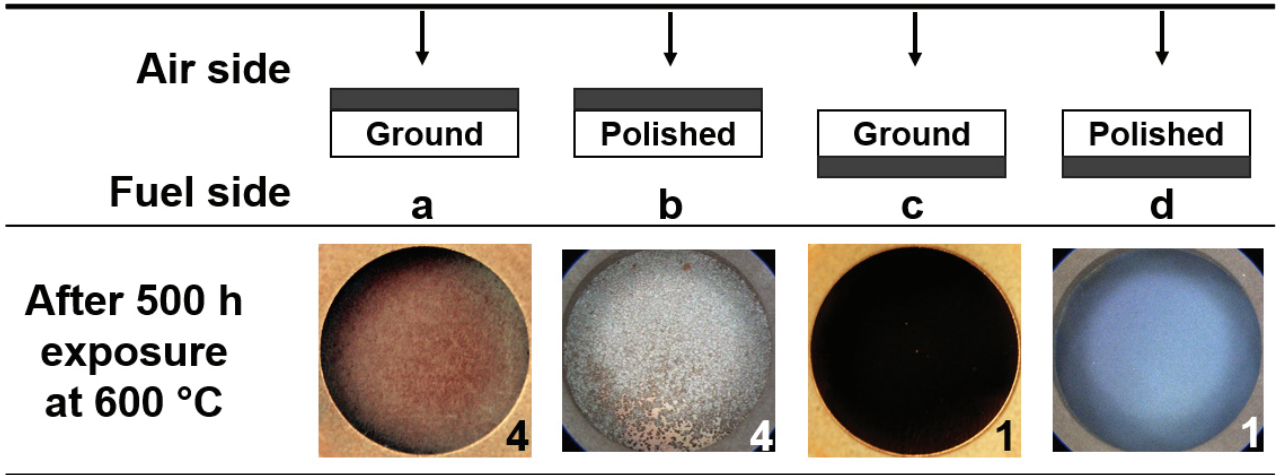


Figure 4.20: Photographs of the air-facing side of AISI 441 exposed to dual atmosphere for 500 h at 600 °C. All samples were pre-oxidized for 180 min at 800 °C in air prior to exposure, and, subsequently, the oxide layer was removed from one side of the sample. The final finish was either achieved by grinding to grit P1200 (a and c) or by polishing to 0.25 μm with diamond paste (b and d). The photographs a and c were taken with a camera, while photographs for samples b and d were taken with an optical microscope. The numbers at the bottom of each picture rate the progress of corrosion and are defined as follows: 1 = only protective behavior present, 2 = mostly protective behavior present, 3 = mostly corroded surface, and 4 = completely corroded surface.

The thickness ratio of oxide to steel in the present study was roughly around 2000 for the thinnest material and 14000 for the thickest. This is in an order of magnitude similar to the difference in the hydrogen permeation coefficient, resulting in a slight effect of FSS thickness on hydrogen permeation and, therefore, the extent of the dual atmosphere effect. Nevertheless, the pre-oxidation layer on the hydrogen-facing side was found to have much higher hydrogen barrier efficiency than the steel itself, even though the contribution of the latter was not entirely negligible.

4.2.4 Influence of Surface Treatment

The study on pre-oxidation location (see Chapter 4.2.2 and Paper V) found that grinding the air-facing surface of AISI 441 samples helped delay the onset of breakaway oxidation in dual atmosphere. The extent of this beneficial effect was shown for non-pre-oxidized samples, which were heavily corroded when left as-received or polished but remained protective when the surface was ground to grit P1200 (see Figure 4.24). The beneficial effect of grinding can be explained by how grinding affects the microstructure of steel: it introduces surface defects and leads to a significant reduction in grain size of the bulk near the steel surface (see Figure 4.24c and 4.25b). The reduction in grain size in particular, with grain sizes of 10 to 50 nm present directly below the protective oxide scale, counteracted the dual atmosphere effect. As stated in Chapter 4.2.1, the dual atmosphere effect is likely due to a reduction of Cr grain boundary diffusion if the density of grain boundaries increases significantly, as was found for ground samples, the negative effect of

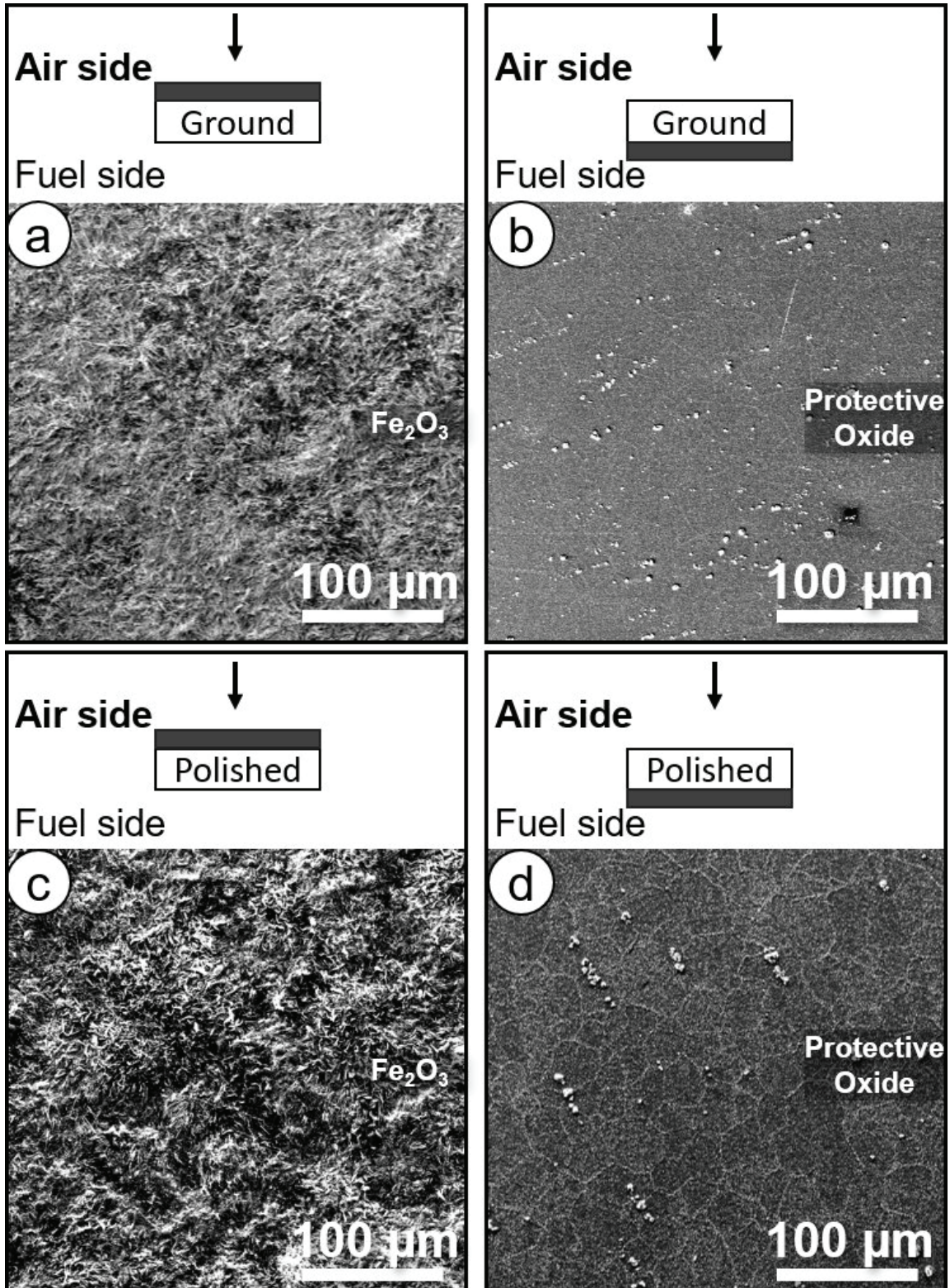


Figure 4.21: SEM micrographs of the air-facing side of AISI 441 exposed to dual atmosphere for 500 h at 600 °C. All samples were pre-oxidized for 180 min at 800 °C in air prior to exposure, and, subsequently, the oxide layer was removed from one side of the sample. The final finish was either done by grinding to grit P1200 (a and b) or by polishing to 0.25 μm with diamond paste (c and d).

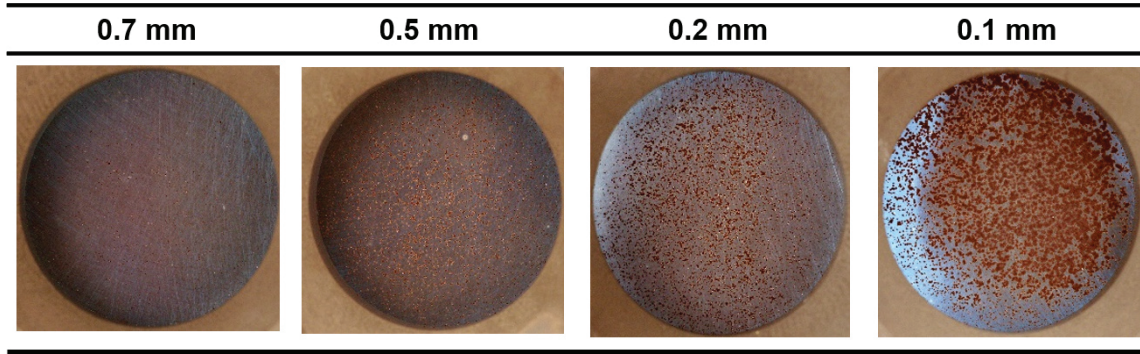


Figure 4.22: Photographs of the air-facing side of AISI 441 samples that were discontinuously exposed to dual atmosphere for 336 h at 600 °C. Prior to dual atmosphere exposure, all the samples were ground from a 1 mm thick AISI 441 steel sheet to the desired thickness with a final finish of grit P1200. The samples were subsequently pre-oxidized for 20 min.

hydrogen will be counteracted. In contrast, polished samples showed a behavior similar to as-received samples. This can be explained by the fact that for polished samples hardly any signs of recrystallization after surface treatment were observed (see Figure 4.25a). However, some areas of the surface of polished samples showed a slight deformation, which might be a remainder of the preceding grinding steps. Nevertheless, the difference in the microstructure of polished or ground samples after surface treatment and without exposure was obvious (see Figure 4.25).

The effect of surface modification on corrosion behavior has previously been discussed in different studies [49, 226, 227], and *Niewolak et al.* [49] observed the beneficial effect of grinding in particular.

4.2.5 Discrepancy in the Literature

As mentioned previously, the discrepancy in the literature on the severity of the dual atmosphere effect at 800 °C can be explained by the results of the studies carried out within this thesis. Factors that influence the dual atmosphere effect, in addition to exposure temperature, are pre-oxidation, sample thickness, and sample surface treatment.

For example, *Alnegren et al.* [32] did not find any dual atmosphere effect at 800 °C, however, the AISI 441 steel in that study had been pre-oxidized for 3 h at 800 °C. Similarly, also *Amendola et al.* [228] have implemented a pre-oxidation step prior to dual atmosphere exposure and found no breakaway oxidation after exposure. On the other hand, *Rufner et al.* [181] and *Gannon et al.* [182] have shown a dramatic dual atmosphere effect with the formation of a thick hematite scale on the surface of AISI 441, but no pre-oxidation had been carried out prior to these experiments. All the studies mentioned in this paragraph were carried out in a similar sample holder that relies on clamping and a gasket as a seal. Other studies, such as the studies carried out by *Kurokawa et al.* [189], have instead used Pyrex as a sealant and required a sealing step, which according to [184] is completed after 1.4 h. This sealing step can be compared to a pre-oxidation step and, therefore, the dual atmosphere effect was much less pronounced in those studies. Those authors also used 2 mm thick material, which could also negate the dual atmosphere effect.

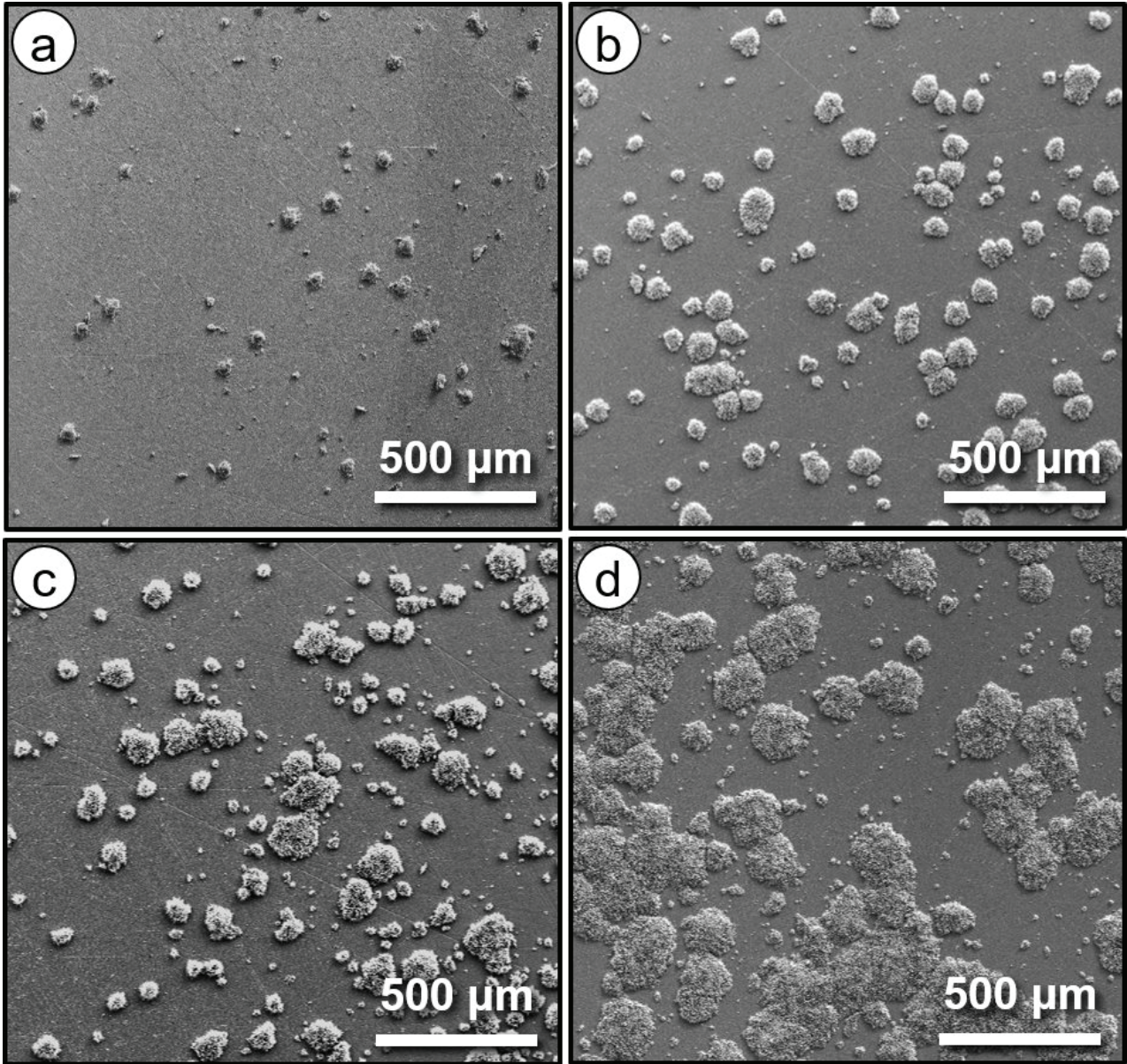


Figure 4.23: *SEM micrographs of the air-facing side of AISI 441 samples that were discontinuously exposed to dual atmosphere for 336 h at 600 °C. Prior to dual atmosphere exposure, all the samples were ground from a 1 mm thick AISI 441 steel sheet to four different thicknesses: 0.7 mm (a), 0.5 mm (b), 0.2 mm (c), and 0.1 mm (d), to a final finish of grit P1200.*

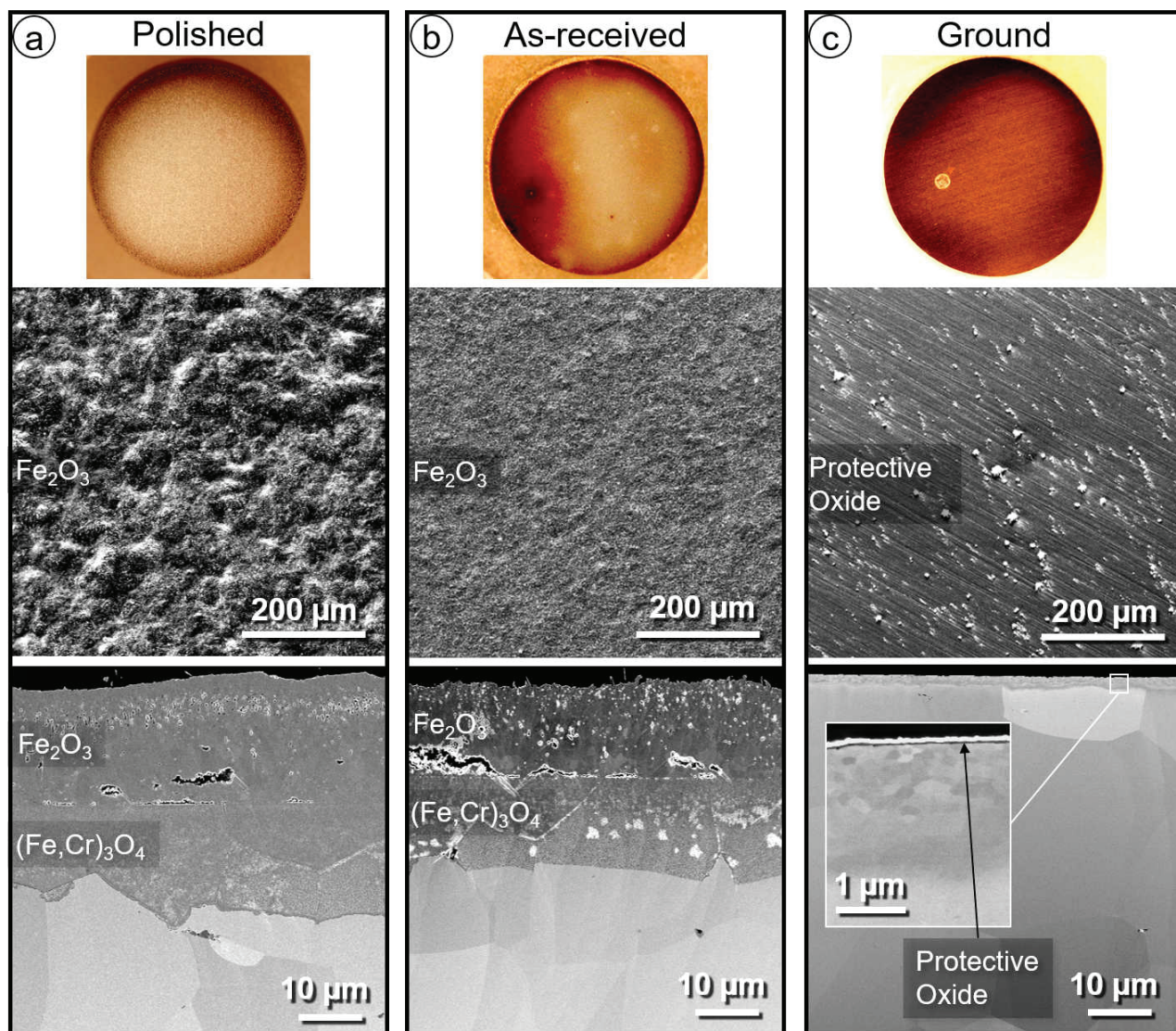


Figure 4.24: Photographs and SEM micrographs of the air-facing side in top-view and of the BIB milled cross-section of AISI 441 samples that were exposed to dual atmosphere discontinuously for 336 h at 600 °C. Prior to exposure, the samples were polished to 0.25 μm with diamond paste (a), left as-received (b), or ground to grit P1200 (c).

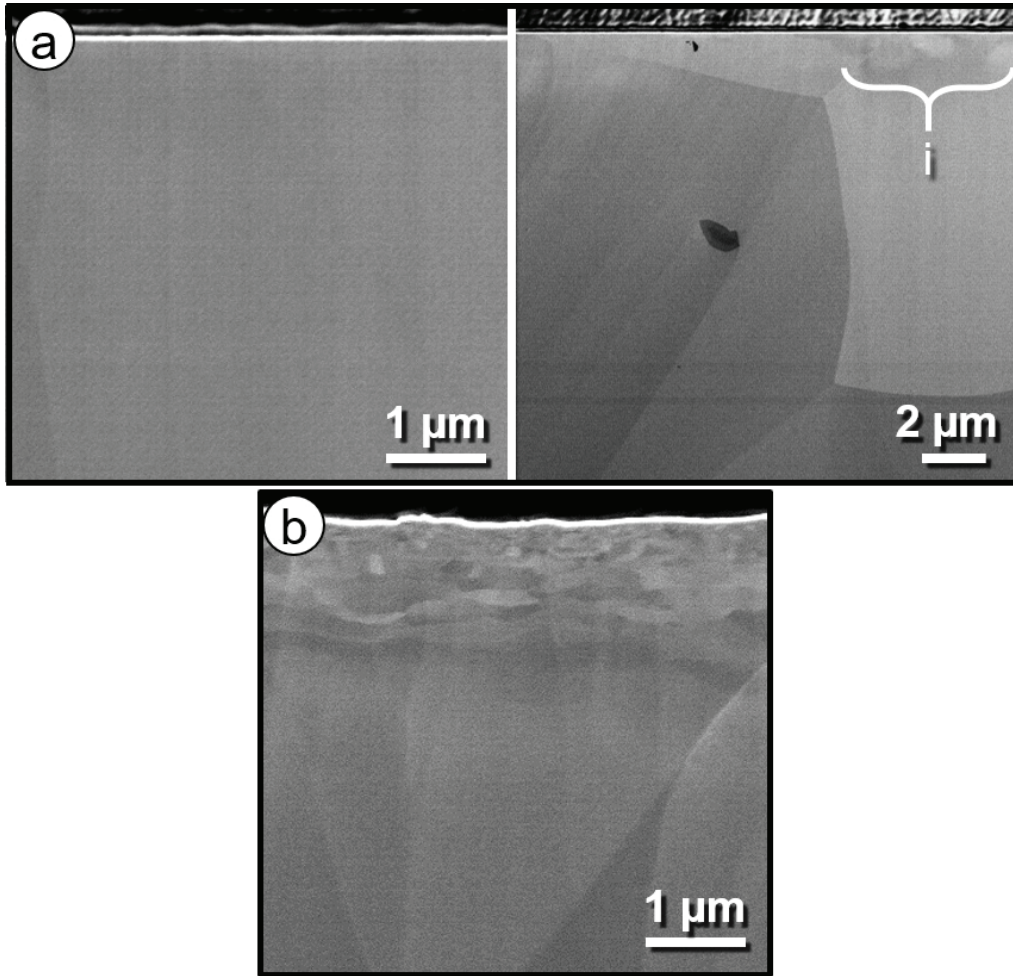


Figure 4.25: SEM micrographs of the air-facing side of unexposed AISI 441 that was either polished to $0.25\mu\text{m}$ with diamond paste (a) or ground to grit P1200 (b). Region marked with an *i* shows remainder of deformation caused by preceding grinding steps.

An added factor that could greatly influence the extent of the dual atmosphere effect is the material examined, with materials that have a higher Cr content outperforming materials with a lower Cr content. For example, *Bredvei Skilbred* et al. [180] have reported only a minor dual atmosphere effect, even though they also opted for a clamping mechanism as a sealant, however, they examined Sanergy HT with a Cr content of 22 wt% in contrast to AISI 441 (17 - 18 wt%).

Nevertheless, some questions remain, for example, why does AISI 441 perform worse than AISI 430, even though they have a similar Cr content [181]. *Gannon* et al. [229] have suggested that this might be due to minor alloying elements, specifically the presence of Niobium in AISI 441 and the absence of this alloying element in AISI 430. Further research is required to elucidate the role of minor alloying elements.

Summary

The present thesis examined the degradation of FSS interconnects with a focus on two different aspects. First, PVD coatings and their influence on the degradation and life-time of fuel cells were analyzed, and second, the dual atmosphere effect was closely investigated.

PVD coatings, specifically the state-of-the-art Ce/Co coating and derivatives thereof, were analyzed with regard to three different factors: their influence on the overall ASR value, their self-healing capabilities at temperatures below 850 °C, and their long-term stability.

By investigating a Co_3O_4 coating, it was found that even moderately well conducting coatings do not significantly impact the overall conductivity of an interconnect. Instead, the ASR values measured for Co_3O_4 -coated AISI 441 were similar, between 8 and 12 $\text{m}\Omega\text{ cm}^2$, regardless of the thickness of the Co_3O_4 layer. This confirmed that the main contributor to ASR was the thermally grown poorly conductive Cr_2O_3 scale underneath the Co_3O_4 layer. Theoretical calculations corroborated this conclusion. Therefore, research must focus on decelerating Cr_2O_3 scale growth rather than increasing the conductivity of the coating. Especially reactive elements added to the alloy, or as a coating, are known to decrease the oxide scale growth rate.

Coatings are often applied to the interconnect before shaping the interconnect into its final form. However, the reverse would be economically favorable. The drawback of first coating the interconnect and then deforming it, is that cracks are introduced into the coating. The present thesis confirmed that these cracks in the coating heal during exposure. The self-healing capabilities of Ce/Co coatings are present even at low operating temperatures (650 °C and 750 °C). Even though the decrease in temperature resulted in a much slower self-healing process than at 850 °C, the Cr evaporation rate of deformed Ce/Co-coated AISI 441 dropped to that of undeformed material after 71 h or 360 h of exposure at 750 °C or 650 °C, respectively. Co-containing spinel was found on top of cracked areas after 71 h at 750 °C and after 111 h at 650 °C. As self-healing occurred at all temperatures between 650 °C and 850 °C, the economically favorable process of large-scale roll-to-roll interconnect manufacturing could be implemented, instead of the costly batch coating process.

The longevity of the Ce/Co coating was confirmed for up to 38 100 h at 800 °C in the present work. It was found that compared to the Cr evaporation rate for uncoated AISI 441, the Cr evaporation rate for Ce/Co-coated AISI 441 had increased only slightly between 1 000 h and 38 100 h of exposure. Additionally, low ASR values, below 40 $\text{m}\Omega\text{ cm}^2$, were measured even after 35 000 h of exposure, and near parabolic behavior was found for

both ASR and mass gain values.

To summarize, the present thesis illustrated the effectiveness of a Ce/Co coating even for long life-times in air-only atmosphere and at 800 °C. It also showed that a Co coating does not negatively influence the overall ASR of an interconnect. Additionally, the coating can be applied in a cost-effective manner by using large-scale roll-to-roll manufacturing processes even for IT-SOFCs. In general, the Ce/Co coating has been researched quite extensively and not many questions remain. However, research into the interaction between Ce/Co-coated material and the electrode material is scarce. Additionally, other coatings are gaining more and more attention in research and in the industry and Cu-containing coatings might be an alternative for IT-SOFCs.

The second part of this thesis investigated the dual atmosphere effect with regard to different parameters: exposure temperature, pre-oxidation, sample thickness, and surface modification.

It was found that the dual atmosphere effect is most severe at 600 °C, and, at this temperature, the entire sample surface of non-pre-oxidized and 20 min pre-oxidized AISI 441 was completely covered in Fe-rich oxide after 336 h of exposure. The dual atmosphere effect quickly disappeared at lower temperatures, and no Fe-rich oxide had formed on AISI 441 at 500 °C. Also a decline in the severity of the dual atmosphere effect was found at temperatures above 600 °C, but this decline was much slower. At 800 °C breakaway oxidation was observed on non-pre-oxidized but not on pre-oxidized AISI 441. Three different parameters that could potentially be affected by hydrogen were identified using the Wagnerian theory. These parameters could be the cause for the dual atmosphere effect: oxygen permeability, Cr₂O₃ scale growth rate, and Cr diffusion in the material. The former two were excluded for theoretical reasons, and it was found that the only parameter that could be reasonably altered by hydrogen was the Cr diffusion. This was corroborated by the fact that a more severe dual atmosphere effect was found at 600 °C than at higher temperatures. It is suggested that hydrogen blocks grain boundary diffusion, which is the more dominant diffusion path at lower temperatures and would explain the corrosion behavior between 600 and 800 °C. The protective behavior at temperatures below 600 °C is explained by the fact that high Fe content in the oxide can be tolerated at lower temperatures without negatively affecting the protectiveness of the oxide.

Pre-oxidation was found to be a good mitigation strategy against the dual atmosphere effect, and longer pre-oxidation times resulted in an increase in corrosion resistance against the dual atmosphere effect. The reverse was also found to be valid and interesting, as it would allow for accelerated testing within limitations. It was excluded that hydrogen affects Cr evaporation on the air-facing side, because Ce/Co-coated AISI 441 had also formed Fe-rich nodules to a similar or even greater extent than uncoated AISI 441 after 3000 h of dual atmosphere exposure and with an implemented 5 h pre-oxidation step. Pre-oxidation mitigated the dual atmosphere effect because of the preformed oxide scale on the hydrogen-facing side of the sample. The preformed oxide scale acted as a hydrogen barrier. This finding suggests that hydrogen barrier coatings on the fuel-facing side of an interconnect would be a good mitigation strategy against the dual atmosphere effect and should be a research topic in the future.

It was further shown that sample thickness and sample surface condition directly influence the extent of the dual atmosphere effect. The effect of sample thickness was only

minor, but thicker samples were found to perform better under dual atmosphere conditions than thinner ones. In contrast, the effect of sample surface condition was significant, and grinding the air-facing side greatly improved the corrosion resistance of the FSS in dual atmosphere. A recrystallized area below the oxide scale was found on the ground samples. This area had evidently formed during grinding and led to extremely small grains (≤ 50 nm). The reduction in grain size is suggested to counteract the decrease in Cr grain boundary diffusion caused by hydrogen. This would be a result of increasing the grain boundary concentration of the bulk alloy at its surface. The polished material performed similar than the as-received material, and both showed heavy breakaway oxidation after 336 h of dual atmosphere exposure. This outcome was expected, because the polished material showed nearly no signs of recrystallization close to the sample surface after polishing and before dual atmosphere exposure.

To summarize the findings on the dual atmosphere effect; a new mechanism for the dual atmosphere effect was proposed and indirectly verified. It was shown that the extent of the dual atmosphere effect is greatly influenced by exposure temperature, pre-oxidation conditions, and sample surface. Sample thickness was found to have a minor effect on the dual atmosphere effect.

Further research is needed on mitigation strategies against the dual atmosphere effect. The main focus of this research should be on the fuel-facing side of the interconnect, as this side seems to be key to preventing the dual atmosphere effect. The oxide on the fuel-facing side of the FSS should be analyzed in more detail, and fuel-side coatings should be designed as hydrogen barrier coatings.

References

- [1] A. Grinsted, P. Ditlevsen, and J. H. Christensen. Normalized US Hurricane Damage Estimates Using Area of Total Destruction, 1900-2018. *Proceedings of the National Academy of Sciences* **116** (2019), 23942–23946. DOI: 10.1073/pnas.1912277116.
- [2] S. C. Lewis, S. A. Blake, B. Trewin, M. T. Black, A. J. Dowdy, S. E. Perkins-Kirkpatrick, A. D. King, and J. J. Sharples. Deconstructing Factors Contributing to the 2018 Fire Weather in Queensland, Australia. *Bulletin of the American Meteorological Society* **101** (2020), S115–S122. DOI: 10.1175/bams-d-19-0144.1.
- [3] N. Phillips and B. Nogrady. The Race to Decipher How Climate Change Influenced Australia’s Record Fires. *Nature* **577** (2020), 610–612. DOI: 10.1038/d41586-020-00173-7.
- [4] M. M. Boer, V. Resco de Dios, and R. A. Bradstock. Unprecedented Burn Area of Australian Mega Forest Fires. *Nature Climate Change* **10** (2020), 171–172. DOI: 10.1038/s41558-020-0716-1.
- [5] G. Hagedorn, P. Kalmus, M. Mann, S. Vicca, J. Van den Berge, J.-P. van Ypersele, D. Bourg, J. Rotmans, R. Kaaronen, S. Rahmstorf, H. Kromp-Kolb, G. Kirchengast, R. Knutti, S. I. Seneviratne, P. Thalmann, R. Cretney, A. Green, K. Anderson, M. Hedberg, D. Nilsson, A. Kuttner, and K. Hayhoe. Concerns of Young Protesters Are Justified. *Science* **364** (2019), 139–140. DOI: 10.1126/science.aax3807.
- [6] M. Warren. Thousands of Scientists Are Backing the Kids Striking for Climate Change. *Nature* **567** (2019), 291. DOI: 10.1038/d41586-019-00861-z.
- [7] P. Forster, V. Ramaswamy, P. Artaxo, T. Berntsen, R. Betts, D. W. Fahey, J. Haywood, J. Lean, D. C. Lowe, G. Myhre, J. Nganga, R. Prinn, G. Raga, M. Schulz, and R. Van Dorland. “Changes in Atmospheric Constituents and in Radiative Forcing”. *Climate Change 2007: The Physical Science Basis. Contribution of Working Group I to the Fourth Assessment Report of the Intergovernmental Panel on Climate Change*. Ed. by S. Solomon, D. Qin, M. Manning, Z. Chen, M. Marquis, K. B. Averyt, M. Tignor, and M. H. L. Cambridge, United Kingdom and New York, USA: Cambridge University Press, 2007, p. 135.
- [8] J.-M. Barnola, D. Raynaud, C. Lorius, and N. I. Barkov. “Historical CO₂ Record From the Vostok Ice Core”. *Trends: A Compendium of Data on Global Change*. Oak Ridge, USA: Carbon Dioxide Information Analysis Center, Oak Ridge National Laboratory, Department of Energy, 2003.
- [9] P. Tans and R. Keeling. *Mauna Loa CO₂ Annual Mean Data*. (www.esrl.noaa.gov/gmd/ccgg/trends/): NOAA/GML, Scripps Institution of Oceanography, 1st of September 2020.
- [10] D. M. Etheridge, L. P. Steele, R. L. Langenfelds, R. J. Francey, J.-M. Barnola, and V. I. Morgan. “Historical CO₂ Records From the Law Dome DE08, DE08-2, and DSS Ice Cores”. *Trends: A Compendium of Data on Global Change*. Oak

- Ridge, USA: Carbon Dioxide Information Analysis Center, Oak Ridge National Laboratory, Department of Energy, 1998.
- [11] Z. Yan, J. L. Hitt, J. A. Turner, and T. E. Mallouk. Renewable Electricity Storage Using Electrolysis. *Proceedings of the National Academy of Sciences* (2019), 12558–12563. DOI: 10.1073/pnas.1821686116.
- [12] M. A. Pellow, C. J. M. Emmott, C. J. Barnhart, and S. M. Benson. Hydrogen or Batteries for Grid Storage? A Net Energy Analysis. *Energy & Environmental Science* **8** (2015), 1938–1952. DOI: 10.1039/C4EE04041D.
- [13] A. Evans, V. Strezov, and T. J. Evans. Assessment of Utility Energy Storage Options for Increased Renewable Energy Penetration. *Renewable and Sustainable Energy Reviews* **16** (2012), 4141–4147. DOI: <https://doi.org/10.1016/j.rser.2012.03.048>.
- [14] D. G. Victor, D. Zhou, E. H. M. Ahmed, P. K. Dadhich, J. G. J. Olivier, H.-H. Rogner, K. Sheikho, and M. Yamaguc. “Introductory Chapter”. *Climate Change 2014: Mitigation of Climate Change. Contribution of Working Group III to the Fifth Assessment Report of the Intergovernmental Panel on Climate Change*. Ed. by O. Edenhofer, R. Pichs-Madruga, Y. Sokona, E. Farahani, S. Kadner, K. Seyboth, A. Adler, I. Baum, S. Brunner, P. Eickemeier, B. Kriemann, J. Savolainen, S. Schlömer, C. von Stechow, T. Zwickel, and J. C. Minx. Cambridge, United Kingdom and New York, NY, USA: Cambridge University Press, 2014, p. 123.
- [15] M. Powell, K. Meinhardt, V. Sprenkle, L. Chick, and G. McVay. Demonstration of a Highly Efficient Solid Oxide Fuel Cell Power System Using Adiabatic Steam Reforming and Anode Gas Recirculation. *Journal of Power Sources* **205** (2012), 377–384. DOI: 10.1016/j.jpowsour.2012.01.098.
- [16] T. Taner. Energy and Exergy Analyze of PEM Fuel Cell: A Case Study of Modeling and Simulations. *Energy* **143** (2018), 284–294. DOI: 10.1016/j.energy.2017.10.102.
- [17] N. P. Brandon, E. Ruiz-Trejo, and P. Boldrin. *Solid Oxide Fuel Cell Lifetime and Reliability: Critical Challenges in Fuel Cells*. 1st ed. Oxford: Elsevier, 2017. ISBN: 978-0-1280-9724-3.
- [18] I. Staffell, A. Ingram, and K. Kendall. Energy and Carbon Payback Times for Solid Oxide Fuel Cell Based Domestic CHP. *International Journal of Hydrogen Energy* **37** (2012), 2509–2523. DOI: 10.1016/j.ijhydene.2011.10.060.
- [19] A. B. Stambouli and E. Traversa. Solid Oxide Fuel Cells (SOFCs): A Review of an Environmentally Clean and Efficient Source of Energy. *Renewable and Sustainable Energy Reviews* **6** (2002), 433–455. DOI: 10.1016/S1364-0321(02)00014-X.
- [20] S. Harboe, A. Schreiber, N. Margaritis, L. Blum, O. Guillon, and N. H. Menzler. Manufacturing Cost Model for Planar 5 kWel SOFC Stacks at Forschungszentrum Jülich. *International Journal of Hydrogen Energy* **45** (2020), 8015–8030. DOI: 10.1016/j.ijhydene.2020.01.082.
- [21] US Department of Energy - Fuel Cell Technologies Office. *3.4 Fuel Cells*. Report. Multi-Year Research, Development, and Demonstration Plan - Planned Program Activities for 2011-2020: https://www.energy.gov/sites/prod/files/2017/05/f34/fcto_myrrdd_fuel_cells.pdf, 2016.

-
- [22] M. Mehrpooya, B. Ghorbani, and H. Abedi. Biodiesel Production Integrated With Glycerol Steam Reforming Process, Solid Oxide Fuel Cell (SOFC) Power Plant. *Energy Conversion and Management* **206** (2020), 112467–112484. DOI: 10.1016/j.enconman.2020.112467.
- [23] L. Niewolak, F. Tietz, and W. J. Quadackers. “Interconnects”. *High-Temperature Solid Oxide Fuel Cells for the 21st Century - Fundamentals, Design and Applications*. Ed. by K. Kendall and M. Kendall. Elsevier Ltd., 2016. DOI: 10.1016/B978-0-12-410453-2.00007-5.
- [24] DOE Contract No. DE-EE005250. *Manufacturing Cost Analysis of 1 kW and 5kW Solid Oxide Fuel Cell (SOFC) for Auxillary Power Applications*. Report. Battelle Memorial Institute, 2014.
- [25] DOE Contract No. DE-EE005250. *Manufacturing Cost Analysis of 100 and 250 kW Fuel Cell Systems for Primary Power and Combined Heat and Power Applications*. Report. Battelle Memorial Institute, 2016.
- [26] R. Scataglini, A. Mayyas, M. Wei, S. H. Chan, T. Lipman, D. Gosselin, A. D’Alessio, H. Breunig, W. G. Colella, and B. D. James. *A Total Cost of Ownership Model for Solid Oxide Fuel Cells in Combined Heat and Power and Power-Only Applications*. Report. Environmental Energy Technologies Division: Ernest Lawrence Berkeley National Laboratory Contract No. DE-AC02-05CH11231, 2015.
- [27] P. Kofstad. *High Temperature Corrosion*. London and New York: Elsevier Applied Science Publishers Ltd., 1988. ISBN: 1-85166-154-9.
- [28] B. B. Ebbinghaus. Thermodynamics of Gas Phase Chromium Species: The Chromium Oxides, the Chromium Oxyhydroxides, and Volatility Calculations in Waste Incineration Processes. *Combustion and Flame* **93** (1993), 119–137. DOI: 10.1016/0010-2180(93)90087-J.
- [29] K. Hilpert, D. Das, M. Miller, D. H. Peck, and R. Weiß. Chromium Vapor Species Over Solid Oxide Fuel Cell Interconnect Materials and Their Potential for Degradation Processes. *Journal of The Electrochemical Society* **143** (1996), 3642–3647. DOI: 10.1149/1.1837264.
- [30] E. J. Opila, D. L. Myers, N. S. Jacobson, I. M. B. Nielsen, D. F. Johnson, J. K. Olminky, and M. D. Allendorf. Theoretical and Experimental Investigation of the Thermochemistry of $\text{CrO}_2(\text{OH})_2(\text{g})$. *The Journal of Physical Chemistry A* **111** (2007), 1971–1980. DOI: 10.1021/jp0647380.
- [31] P. Alnegren, M. Sattari, J.-E. Svensson, and J. Froitzheim. Severe Dual Atmosphere Effect at 600 °C for Stainless Steel 441. *Journal of Power Sources* **301** (2016), 170–178. DOI: 10.1016/j.jpowsour.2015.10.001.
- [32] P. Alnegren, M. Sattari, J.-E. Svensson, and J. Froitzheim. Temperature Dependence of Corrosion of Ferritic Stainless Steel in Dual Atmosphere at 600–800 °C. *Journal of Power Sources* **392** (2018), 129–138. DOI: 10.1016/j.jpowsour.2018.04.088.
- [33] H. Kurokawa, C. P. Jacobson, L. C. DeJonghe, and S. J. Visco. Chromium Vaporization of Bare and of Coated Iron–Chromium Alloys at 1073 K. *Solid State Ionics* **178** (2007), 287–296. DOI: 10.1016/j.ssi.2006.12.010.

- [34] R. Trebbels, T. Markus, and L. Singheiser. Investigation of Chromium Vaporization from Interconnector Steels With Spinel Coatings. *Journal of The Electrochemical Society* **157** (2010), B490–B495. DOI: 10.1149/1.3298434.
- [35] P. Y. Hou and J. Stringer. The Effect of Reactive Element Additions on the Selective Oxidation, Growth and Adhesion of Chromia Scales. *Materials Science and Engineering: A* **202** (1995), 1–10. DOI: 10.1016/0921-5093(95)09798-8.
- [36] K. Huang, P. Y. Hou, and J. B. Goodenough. Reduced Area Specific Resistance for Iron-Based Metallic Interconnects by Surface Oxide Coatings. *Materials Research Bulletin* **36** (2001), 81–95. DOI: 10.1016/S0025-5408(01)00506-2.
- [37] J. Froitzheim, S. Canovic, M. Nikumaa, R. Sachitanand, L. G. Johansson, and J. E. Svensson. Long Term Study of Cr Evaporation and High Temperature Corrosion Behaviour of Co Coated Ferritic Steel for Solid Oxide Fuel Cell Interconnects. *Journal of Power Sources* **220** (2012), 217–227. DOI: 10.1016/j.jpowsour.2012.06.092.
- [38] A. Kruk, M. Stygar, and T. Brylewski. Mn–Co Spinel Protective–Conductive Coating on AL453 Ferritic Stainless Steel for IT-SOFC Interconnect Applications. *Journal of Solid State Electrochemistry* **17** (2013), 993–1003. DOI: 10.1007/s10008-012-1952-8.
- [39] G. Chen, X. Xin, T. Luo, L. Liu, Y. Zhou, C. Yuan, C. Lin, Z. Zhan, and S. Wang. Mn_{1.4}Co_{1.4}Cu_{0.2}O₄ Spinel Protective Coating on Ferritic Stainless Steels for Solid Oxide Fuel Cell Interconnect Applications. *Journal of Power Sources* **278** (2015), 230–234. DOI: 10.1016/j.jpowsour.2014.12.070.
- [40] V. Miguel-Pérez, A. Martínez-Amesti, M. L. Nó, A. Larrañaga, and M. I. Arriortua. The Effect of Doping (Mn,B)₃O₄ Materials as Protective Layers in Different Metallic Interconnects for Solid Oxide Fuel Cells. *Journal of Power Sources* **243** (2013), 419–430. DOI: 10.1016/j.jpowsour.2013.05.109.
- [41] S. Chevalier, G. Caboche, K. Przybylski, and T. Brylewski. Effect of Nano-Layered Ceramic Coatings on the Electrical Conductivity of Oxide Scale Grown on Ferritic Steels. *Journal of Applied Electrochemistry* **39** (2009), 529–534. DOI: 10.1007/s10800-008-9726-9.
- [42] T. Brylewski, A. Kruk, M. Bobruk, A. Adamczyk, J. Partyka, and P. Rutkowski. Structure and Electrical Properties of Cu-Doped Mn-Co-O Spinel Prepared via Soft Chemistry and Its Application In Intermediate-Temperature Solid Oxide Fuel Cell Interconnects. *Journal of Power Sources* **333** (2016), 145–155. DOI: 10.1016/j.jpowsour.2016.09.136.
- [43] Y. Xu, Z. Wen, S. Wang, and T. Wen. Cu Doped Mn–Co Spinel Protective Coating on Ferritic Stainless Steels for SOFC Interconnect Applications. *Solid State Ionics* **192** (2011), 561–564. DOI: 10.1016/j.ssi.2010.05.052.
- [44] N. Shaigan, W. Qu, D. G. Ivey, and W. Chen. A Review of Recent Progress in Coatings, Surface Modifications and Alloy Developments for Solid Oxide Fuel Cell Ferritic Stainless Steel Interconnects. *Journal of Power Sources* **195** (2010), 1529–1542. DOI: 10.1016/j.jpowsour.2009.09.069.
- [45] B.-K. Park, J.-W. Lee, S.-B. Lee, T.-H. Lim, S.-J. Park, C.-O. Park, and R.-H. Song. Cu- and Ni-Doped Mn_{1.5}Co_{1.5}O₄ Spinel Coatings on Metallic Interconnects

- for Solid Oxide Fuel Cells. *International Journal of Hydrogen Energy* **38** (2013), 12043–12050. DOI: 10.1016/j.ijhydene.2013.07.025.
- [46] K. H. Tan, H. A. Rahman, and H. Taib. Coating Layer and Influence of Transition Metal for Ferritic Stainless Steel Interconnector Solid Oxide Fuel Cell: A Review. *International Journal of Hydrogen Energy* **44** (2019), 30591–30605. DOI: 10.1016/j.ijhydene.2019.06.155.
- [47] H. Falk-Windisch, M. Sattari, J.-E. Svensson, and J. Froitzheim. Chromium Vaporization From Mechanically Deformed Pre-Coated Interconnects in Solid Oxide Fuel Cells. *Journal of Power Sources* **297** (2015), 217–223. DOI: 10.1016/j.jpowsour.2015.07.085.
- [48] H. Falk-Windisch, I. Mertzidis, J.-E. Svensson, and J. Froitzheim. Pre-Coated Ce/Co-Coated Steel: Mitigating Cr Vaporization, Increasing Corrosion Resistance at Competitive Cost. *ECS Transactions* **68** (2015), 1617–1623. DOI: 10.1149/06801.1617ecst.
- [49] L. Niewolak, E. Wessel, L. Singheiser, and W. J. Quadakkers. Potential Suitability of Ferritic and Austenitic Steels as Interconnect Materials for Solid Oxide Fuel Cells Operating at 600 °C. *Journal of Power Sources* **195** (2010), 7600–7608. DOI: 10.1016/j.jpowsour.2010.06.007.
- [50] D. J. L. Brett, A. Atkinson, N. P. Brandon, and S. J. Skinner. Intermediate Temperature Solid Oxide Fuel Cells. *Chemical Society Reviews* **37** (2008), 1568–1578. DOI: 10.1039/B612060C.
- [51] B. C. H. Steele. Material Science and Engineering: The Enabling Technology for the Commercialisation of Fuel Cell Systems. *Journal of Materials Science* **36** (2001), 1053–1068. DOI: 10.1023/A:1004853019349.
- [52] M. Linder, T. Hocker, L. Holzer, K. A. Friedrich, B. Iwanschitz, A. Mai, and J. A. Schuler. Cr₂O₃ Scale Growth Rates on Metallic Interconnectors Derived From 40,000 h Solid Oxide Fuel Cell Stack Operation. *Journal of Power Sources* **243** (2013), 508–518. DOI: 10.1016/j.jpowsour.2013.05.200.
- [53] S. M. Groß-Barsnick, Q. Fang, P. Batfalsky, L. Niewolak, L. Blum, and W. J. Quadakkers. Post-Test Characterization of Metallic Materials and Adjacent Components in an SOFC Stack After 34 000 h Operation at 700 °C. *Fuel Cells* **19** (2019), 84–95. DOI: 10.1002/fuce.201800050.
- [54] S. Fontana, S. Chevalier, and G. Caboche. Metallic Interconnects for Solid Oxide Fuel Cell: Performance of Reactive Element Oxide Coating During 10, 20 and 30 Months Exposure. *Oxidation of Metals* **78** (2012), 307–328. DOI: 10.1007/s11085-012-9308-4.
- [55] L. Mikkelsen, K. Neufeld, and P. Hendriksen. Interface Resistance Between FeCr Interconnects and La_{0.85}Sr_{0.15}Mn_{1.1}O₃. *Electrochemical Society Transactions* **25** (2009), 1429–1436. DOI: 10.1149/1.3205675.
- [56] M. Galvez Sanchez, M. Oum, S. Pandyan, A. J. Majewski, L. Troskialina, and R. Steinberger-Wilckens. *SCoReD 2:0 - Steel Coatings for Reducing Degradation*. Report. University of Birmingham, 2017.
- [57] M. Bianco, J. Tallgren, J.-E. Hong, S. Yang, O. Himanen, J. Mikkola, J. Van herle, and R. Steinberger-Wilckens. Ex-Situ Experimental Benchmarking of Solid Oxide

- Fuel Cell Metal Interconnects. *Journal of Power Sources* **437** (2019), 226900–226909. DOI: 10.1016/j.jpowsour.2019.226900.
- [58] S. Canovic, J. Froitzheim, R. Sachitanand, M. Nikumaa, M. Halvarsson, L. G. Johansson, and J.-E. Svensson. Oxidation of Co- and Ce-Nanocoated FeCr Steels: A Microstructural Investigation. *Surface and Coatings Technology* **215** (2013), 62–74. DOI: 10.1016/j.surfcoat.2012.08.096.
- [59] A. Magrasó, H. Falk-Windisch, J. Froitzheim, J.-E. Svensson, and R. Haugsrud. Reduced Long Term Electrical Resistance in Ce/Co-Coated Ferritic Stainless Steel for Solid Oxide Fuel Cell Metallic Interconnects. *International Journal of Hydrogen Energy* **40** (2015), 8579–8585. DOI: 10.1016/j.ijhydene.2015.04.147.
- [60] W. R. Grove. LVI. On a New Voltaic Combination. *The London, Edinburgh, and Dublin Philosophical Magazine and Journal of Science* **13** (1838), 430–431. DOI: 10.1080/14786443808649618.
- [61] W. R. Grove. XXIV. On Voltaic Series and the Combination of Gases by Platinum. *The London, Edinburgh, and Dublin Philosophical Magazine and Journal of Science* **14** (1839), 127–130. DOI: 10.1080/14786443908649684.
- [62] C. F. Schoenbein. X. On the Voltaic Polarization of Certain Solid and Fluid Substances. *The London, Edinburgh, and Dublin Philosophical Magazine and Journal of Science* **14** (1839), 43–45. DOI: 10.1080/14786443908649658.
- [63] J. F. Keithley. “A Carefully Prepared Leg of a Dead Frog Twitches When Stimulated Electrically”. *The Story of Electrical and Magnetic Measurements: From 500 BC to the 1940s*. Ed. by R. F. Hoyt. New York, US: Wiley-IEEE Press, 1999, pp. 49–51. DOI: 10.1109/9780470546628.ch10.
- [64] L. Galvani. Aloysii Galvani De Viribus Electricitatis in Motu Musculari Commentarius. *Bononiae: Ex Typographia Instituti Scientiarum* (1791). DOI: 10.5479/sil.324681.39088000932442.
- [65] A. Volta. XVII. On the Electricity Excited by the Mere Contact of Conducting Substances of Different Kinds. In a Letter from Mr. Alexander Volta, F. R. S. Professor of Natural Philosophy in the University of Pavia, to the Rt. Hon. Sir Joseph Banks, Bart. K.B. P. R. S. *Philosophical Transactions of the Royal Society of London* **90** (1800), 403–431. DOI: 10.1098/rstl.1800.0018.
- [66] S. Srinivasan. *Fuel Cells: From Fundamentals to Applications*. Boston, MA: Springer US, 2006. DOI: 10.1007/0-387-35402-6_1.
- [67] S.-W. Cha, W. Colella, F. B. Prinz, and R. O’Hayre. *Fuel Cell Fundamentals*. Somerset, US: John Wiley & Sons, Inc., 2016. ISBN: 978-1-1191-1415-4.
- [68] D. F. Shriver and P. W. Atkins. *Shriver and Atkins Inorganic Chemistry*. 3rd ed. Oxford University Press, 1999. ISBN: 978-0-1985-0331-6.
- [69] J. Larminie and A. Dicks. *Fuel Cell Systems Explained*. 2nd ed. West Sussex: John Wiley & Sons Ltd, 2003. DOI: 10.1002/9781118878330.
- [70] A. Kirubakaran, S. Jain, and R. K. Nema. A Review on Fuel Cell Technologies and Power Electronic Interface. *Renewable and Sustainable Energy Reviews* **13** (2009), 2430–2440. DOI: 10.1016/j.rser.2009.04.004.
- [71] E4tech. *Fuel Cell Industry Review*. Report. <http://www.fuelcellindustryreview.com/>, 2019.

-
- [72] Y. Larring, R. Haugsrud, and T. Norby. HT Corrosion of a Cr-5 wt% Fe-1 wt% Y₂O₃ Alloy and Conductivity of the Oxide Scale. Effects of Water Vapor. *Journal of the Electrochemical Society* **150** (2003), B374–B379. DOI: 10.1149/1.1587726.
 - [73] S. C. Singhal. “Solid Oxide Fuel Cells: Past, Present and Future”. *Solid Oxide Fuels Cells: Facts and Figures: Past, Present and Future Perspectives for SOFC Technologies*. Ed. by J. T. S. Irvine and P. Connor. 1st ed. London: Springer London, 2013, pp. 1–23. DOI: 10.1007/978-1-4471-4456-4_1.
 - [74] K. Lee, B. Yoon, J. Kang, S. Lee, and J. Bae. Evaluation of Ag-Doped (Mn,Co)₃O₄ Spinel as a Solid Oxide Fuel Cell Metallic Interconnect Coating Material. *International Journal of Hydrogen Energy* **42** (2017), 29511–29517. DOI: 10.1016/j.ijhydene.2017.10.017.
 - [75] S. C. Singhal and K. Kendall. “Introduction to SOFCs”. *High Temperature Solid Oxide Fuel Cells - Fundamentals, Design and Applications*. Ed. by S. C. Singhal and K. Kendall. 1st ed. Oxford: Elsevier, 2003. ISBN: 978-1-8561-7387-2.
 - [76] H. Nirasawa. Current Status of National SOFC Projects in Japan. *ECS Transactions* **78** (2017), 33–40. DOI: 10.1149/07801.0033ecst.
 - [77] A. Perna and M. Minutillo. “Chapter 9 - Residential Cogeneration and Trigeneration With Fuel Cells”. *Current Trends and Future Developments on (Bio-) Membranes*. Ed. by A. Basile and G. Spazzafumo. Elsevier, 2020, pp. 197–239. DOI: 10.1016/B978-0-12-817807-2.00009-5.
 - [78] T. Nakao, S. Inoue, S. Uenoyama, Y. Takuwa, and M. Suzuki. Progress of SOFC Residential CHP System: Over 50,000 Units Market Experience of Osaka Gas. *ECS Transactions* **91** (2019), 43–49. DOI: 10.1149/09101.0043ecst.
 - [79] W. Winkler. “Thermodynamics”. *High Temperature Solid Oxide Fuel Cells - Fundamentals, Design and Applications*. Ed. by S. C. Singhal and K. Kendall. 1st ed. Oxford: Elsevier, 2003. ISBN: 978-1-8561-7387-2.
 - [80] J. G. Grolig. “Coated ferritic stainless steels as interconnects in solid oxide fuel cells”. Doctor of Philosophy. Gothenburg, Sweden: Chalmers University of Technology, 2015. ISBN: 978-9-1759-7234-3.
 - [81] T. Ishihara, N. M. Sammes, and O. Yamamoto. “Electrolytes”. *High Temperature Solid Oxide Fuel Cells - Fundamentals, Design and Applications*. Ed. by S. C. Singhal and K. Kendall. 1st ed. Oxford: Elsevier, 2003. ISBN: 978-1-8561-7387-2.
 - [82] C. Xia. “Electrolytes”. *Solid Oxide Fuel Cells: Materials Properties and Performance*. Ed. by J. W. Fergus, R. Hui, X. Li, D. P. Wilkinson, and J. Zhang. Florida: Taylor & Francis Group, 2009. ISBN: 978-0-3673-8643-6.
 - [83] J. A. Kilner, J. Druce, and T. Ishihara. “Electrolytes”. *High-Temperature Solid Oxide Fuel Cells for the 21st Century - Fundamentals, Design and Applications*. Ed. by K. Kendall and M. Kendall. Elsevier, 2016. DOI: 10.1016/B978-0-12-410453-2.00007-5.
 - [84] M. Cassidy, P. A. Connor, J. T. S. Irvine, and C. D. Savaniu. “Anodes”. *High-Temperature Solid Oxide Fuel Cells for the 21st Century - Fundamentals, Design and Applications*. Ed. by K. Kendall and M. Kendall. Elsevier, 2016. DOI: 10.1016/B978-0-12-410453-2.00007-5.

- [85] Z. Cheng, J.-H. Wang, and M. Liu. “Anodes”. *Solid Oxide Fuel Cells: Materials Properties and Performance*. Ed. by J. W. Fergus, R. Hui, X. Li, D. P. Wilkinson, and J. Zhang. Florida: Taylor & Francis Group, 2009. ISBN: 978-0-3673-8643-6.
- [86] T. Kawada and T. Horita. “Cathodes”. *High-Temperature Solid Oxide Fuel Cells for the 21st Century - Fundamentals, Design and Applications*. Ed. by K. Kendall and M. Kendall. Elsevier, 2016. DOI: 10.1016/B978-0-12-410453-2.00007-5.
- [87] S. P. Jiang and J. Li. “Cathodes”. *Solid Oxide Fuel Cells: Materials Properties and Performance*. Ed. by J. W. Fergus, R. Hui, X. Li, D. P. Wilkinson, and J. Zhang. Florida: Taylor & Francis Group, 2009. ISBN: 978-0-3673-8643-6.
- [88] Z. Yang and J. W. Fergus. “Interconnects”. *Solid Oxide Fuel Cells: Materials Properties and Performance*. Ed. by J. W. Fergus, R. Hui, X. Li, D. P. Wilkinson, and J. Zhang. Florida: Taylor & Francis Group, 2009. ISBN: 978-0-3673-8643-6.
- [89] A. Brouzgou, A. Demin, and P. Tsiakaras. “Interconnects for Solid Oxide Fuel Cells”. *Advances in Medium and High Temperature Solid Oxide Fuel Cell Technology*. Ed. by M. Boaro and A. A. Salvatore. 1st ed. Cham: Springer International Publishing, 2017, pp. 119–153. DOI: 10.1007/978-3-319-46146-5_4.
- [90] N. Birks, G. H. Meier, and F. S. Pettit. *Introduction to the High-Temperature Oxidation of Metals*. 2nd ed. Cambridge: Cambridge University Press, 2006. ISBN: 978-0-5214-8517-3.
- [91] D. J. Young. *High Temperature Oxidation and Corrosion of Metals*. 2nd ed. Elsevier Ltd., 2016. DOI: 10.1016/B978-0-08-100101-1.00002-9.
- [92] H. J. T. Ellingham. Reducibility of Oxides and Sulphides in Metallurgical Processes. *Journal of the Society of Chemical Industry* **63** (1944), 125–160. DOI: 10.1002/jctb.5000630501.
- [93] I. Barin. *Thermochemical Data of Pure Substances*. 3rd ed. Vol. 1. Weinheim, Germany: VCH Verlagsgesellschaft mbH, 1995. ISBN: 978-3-5272-8745-1.
- [94] H. V. Keer. *Principles of the Solid State*. Wiley, 1993. ISBN: 978-0-4702-2052-8.
- [95] P. Sarrazin, A. Galerie, and J. Fouletier. *Mechanisms of High Temperature Corrosion - A Kinetic Approach*. Trans Tech Publications Ltd, 2008. ISBN: 978-0-87849-484-2.
- [96] C. Wagner. Beitrag zur Theorie des Anlaufvorgangs. *Zeitschrift für Physikalische Chemie* **21B** (1933), 25–41. DOI: 10.1515/zpch-1933-2105.
- [97] C. Wagner. Fehlordnungserscheinungen in kristallisierten polaren Verbindungen als Grundlage für Elektronen- und Ionen-Leitung. *Zeitschrift für Elektrochemie und angewandte physikalische Chemie* **39.7b** (1933), 543–545. ISSN: 0372-8323. DOI: 10.1002/bbpc.19330390719.
- [98] A. S. Khanna. “High Temperature Oxidation”. *Handbook of Environmental Degradation of Materials*. Ed. by M. Kutz. 2nd ed. Oxford: William Andrew Publishing, 2012, pp. 127–194. DOI: 10.1016/B978-1-4377-3455-3.00005-5.
- [99] C. Wagner. Equations for Transport in Solid Oxides and Sulfides of Transition Metals. *Progress in Solid State Chemistry* **10** (1975), 3–16. DOI: 10.1016/0079-6786(75)90002-3.
- [100] N. B. Pilling and R. E. Bedworth. The Oxidation of Metals at High Temperatures. *Journal of the Institute of Metals* **29** (1923), 529–582. DOI: 10.1098/rspa.1926.0062.

- [101] A. R. West. *Basic Solid State Chemistry*. 2nd Edition. West Sussex, England: John Wiley and Sons Ltd., 2006. ISBN: 978-0-471-98755-0.
- [102] P. Shewmon. *Diffusion in Solids*. 2nd ed. Switzerland: Springer International Publishers, 2016. ISBN: 978-0-87339-105-4.
- [103] H. Asteman. “Water Vapour Induced Active Oxidation of Stainless Steel”. Doctor of Philosophy. Gothenburg, Sweden: University of Gothenburg, 2002.
- [104] E. McCafferty. *Introduction to Corrosion Science*. 1st ed. New York: Springer, 2010. DOI: 10.1007/978-1-4419-0455-3.
- [105] A. S. Khanna. *Introduction to High Temperature Oxidation and Corrosion*. ASM International, 2002. ISBN: 978-0-871-70762-8.
- [106] R. A. Rapp. The Transition From Internal to External Oxidation and the Formation of Interruption Bands in Silver-Indium Alloys. *Acta Metallurgica* **9** (1961), 730–741. DOI: 10.1016/0001-6160(61)90103-1.
- [107] G. H. Meier, K. Jung, N. Mu, N. M. Yanar, F. S. Pettit, J. Pirón Abellán, T. Olszewski, L. Nieto Hierro, W. J. Quadakkers, and G. R. Holcomb. Effect of Alloy Composition and Exposure Conditions on the Selective Oxidation Behavior of Ferritic Fe–Cr and Fe–Cr–X Alloys. *Oxidation of Metals* **74** (2010), 319–340. DOI: 10.1007/s11085-010-9215-5.
- [108] C. Wagner. Oxidation of Alloys Involving Noble Metals. *Journal of The Electrochemical Society* **103** (1956), 571–580. DOI: 10.1149/1.2430159.
- [109] C. Wagner. Reaktionstypen bei der Oxydation von Legierungen. *Zeitschrift für Elektrochemie, Berichte der Bunsengesellschaft für physikalische Chemie* **63** (1959), 772–782. DOI: 10.1002/bbpc.19590630713.
- [110] H. E. Evans, A. T. Donaldson, and T. C. Gilmour. Mechanisms of Breakaway Oxidation and Application to a Chromia-Forming Steel. *Oxidation of Metals* **52** (1999), 379–402. DOI: 10.1023/a:1018855914737.
- [111] M. Schütze, D. Renusch, and M. Schorr. Chemical-Mechanical Failure of Oxide Scales on 9 % Cr Steels in Air With H₂O. *Materials at High Temperatures* **22** (2005), 113–120. DOI: 10.1179/mht.2005.013.
- [112] E. Essuman, G. H. Meier, J. Żurek, M. Hänsel, L. Singheiser, and W. J. Quadakkers. Enhanced Internal Oxidation as Trigger for Breakaway Oxidation of Fe–Cr Alloys in Gases Containing Water Vapor. *Scripta Materialia* **57** (2007), 845–848. DOI: 10.1016/j.scriptamat.2007.06.058.
- [113] G. Hultquist, B. Tveten, and E. Hörnlund. Hydrogen in Chromium: Influence on the High-Temperature Oxidation Kinetics in H₂O, Oxide-Growth Mechanisms, and Scale Adherence. *Oxidation of Metals* **54** (2000), 1–10. DOI: 10.1023/a:1004610626903.
- [114] L. Luo, M. Su, P. Yan, L. Zou, D. K. Schreiber, D. R. Baer, Z. Zhu, G. Zhou, Y. Wang, S. M. Bruemmer, Z. Xu, and C. Wang. Atomic Origins of Water-Vapour-Promoted Alloy Oxidation. *Nature Materials* **17** (2018), 514–518. DOI: 10.1038/s41563-018-0078-5.
- [115] A. W. Bredvei Skilbred and R. Haugsrud. Sandvik Sanergy HT – A Potential Interconnect Material for LaNbO₄-Based Proton Ceramic Fuel Cells. *Journal of Power Sources* **206** (2012), 70–76. DOI: 10.1016/j.jpowsour.2012.01.101.

- [116] M. Palcut, L. Mikkelsen, K. Neufeld, M. Chen, R. Knibbe, and P. V. Hendriksen. Corrosion Stability of Ferritic Stainless Steels for Solid Oxide Electrolyser Cell Interconnects. *Corrosion Science* **52** (2010), 3309–3320. DOI: 10.1016/j.corsci.2010.06.006.
- [117] H. Falk-Windisch, J.-E. Svensson, and J. Froitzheim. The Effect of Temperature on Chromium Vaporization and Oxide Scale Growth on Interconnect Steels for Solid Oxide Fuel Cells. *Journal of Power Sources* **287** (2015), 25–35. DOI: 10.1016/j.jpowsour.2015.04.040.
- [118] T. Brylewski, M. Nanko, T. Maruyama, and K. Przybylski. Application of Fe–16Cr Ferritic Alloy to Interconnector for a Solid Oxide Fuel Cell. *Solid State Ionics* **143** (2001), 131–150. DOI: 10.1016/S0167-2738(01)00863-3.
- [119] S. Fontana, R. Amendola, S. Chevalier, P. Piccardo, G. Caboche, M. Viviani, R. Molins, and M. Sennour. Metallic Interconnects for SOFC: Characterisation of Corrosion Resistance and Conductivity Evaluation at Operating Temperature of Differently Coated Alloys. *Journal of Power Sources* **171** (2007), 652–662. DOI: 10.1016/j.jpowsour.2007.06.255.
- [120] V. Sauchuk, S. Megel, E. Girdauskaite, N. Trofimenko, M. Kusnezoff, and A. Michaelis. Influence of Protective Layers on SOFC Operation. *Russian Journal of Electrochemistry* **47** (2011), 522. DOI: 10.1134/S1023193511050107.
- [121] Z. Yang, M. Guo, N. Wang, C. Ma, J. Wang, and M. Han. A Short Review of Cathode Poisoning and Corrosion in Solid Oxide Fuel Cell. *International Journal of Hydrogen Energy* **42** (2017), 24948–24959. DOI: 10.1016/j.ijhydene.2017.08.057.
- [122] S. Megel. “Kathodische Kontaktierung in Planaren Hochtemperatur-Brennstoffzellen”. Doctor of Philosophy. Stuttgart, Deutschland: Fraunhofer Institut für Keramische Technologien und Systems IKTS, 2009. ISBN: 978-3-8396-0066-5.
- [123] R. Sachitanand, M. Sattari, J.-E. Svensson, and J. Froitzheim. Evaluation of the Oxidation and Cr Evaporation Properties of Selected FeCr Alloys Used as SOFC Interconnects. *International Journal of Hydrogen Energy* **38** (2013), 15328–15334. DOI: 10.1016/j.ijhydene.2013.09.044.
- [124] E. J. Carlson, Y. Yang, and C. Fulton. *Solid Oxide Fuel Cell Manufacturing Cost Model: Simulating Relationships between Performance, Manufacturing, and Cost of Production*. Report. DOE Contract No. DE-FC26-02NT41568: TIAx, 2004.
- [125] J. Fergus and Y. Zhao. Low-Chromium Alloys for Solid Oxide Fuel Cell Interconnects. *ECS Transactions* **35** (2011), 2447–2453. DOI: 10.1149/1.3570242.
- [126] M. R. Ardigo, I. Popa, S. Chevalier, S. Weber, O. Heintz, and M. Vilasi. Effect of Water Vapor on the Oxidation Mechanisms of a Commercial Stainless Steel for Interconnect Application in High Temperature Water Vapor Electrolysis. *Oxidation of Metals* **79** (2013), 495–505. DOI: 10.1007/s11085-012-9338-y.
- [127] Z. Yang, G.-G. Xia, C.-M. Wang, Z. Nie, J. Templeton, J. W. Stevenson, and P. Singh. Investigation of Iron–Chromium–Niobium–Titanium Ferritic Stainless Steel for Solid Oxide Fuel Cell Interconnect Applications. *Journal of Power Sources* **183** (2008), 660–667. DOI: 10.1016/j.jpowsour.2008.05.037.
- [128] W. Qu, L. Jian, J. M. Hill, and D. G. Ivey. Electrical and Microstructural Characterization of Spinel Phases as Potential Coatings for SOFC Metallic Interconnects.

- Journal of Power Sources* **153** (2006), 114–124. DOI: 10.1016/j.jpowsour.2005.03.137.
- [129] J. G. Grolig, J. Froitzheim, and J.-E. Svensson. Coated Stainless Steel 441 as Interconnect Material for Solid Oxide Fuel Cells: Evolution of Electrical Properties. *Journal of Power Sources* **284** (2015), 321–327. DOI: 10.1016/j.jpowsour.2015.03.029.
- [130] J. G. Grolig, J. Froitzheim, and J.-E. Svensson. Coated Stainless Steel 441 as Interconnect Material for Solid Oxide Fuel Cells: Oxidation Performance and Chromium Evaporation. *Journal of Power Sources* **248** (2014), 1007–1013. DOI: 10.1016/j.jpowsour.2013.08.089.
- [131] F. Cheng, J. Cui, L. Wang, S. Li, and J. Sun. Performance of CoNiO Spinel Oxide Coating on AISI 430 Stainless Steel as Interconnect for Intermediate Temperature Solid Oxide Fuel Cell. *International Journal of Hydrogen Energy* **42** (2017), 12477–12484. DOI: 10.1016/j.ijhydene.2017.03.217.
- [132] N. Hosseini, M. H. Abbasi, F. Karimzadeh, and G. M. Choi. Development of $\text{Cu}_{1.3}\text{Mn}_{1.7}\text{O}_4$ Spinel Coating on Ferritic Stainless Steel for Solid Oxide Fuel Cell Interconnects. *Journal of Power Sources* **273** (2015), 1073–1083. DOI: 10.1016/j.jpowsour.2014.10.017.
- [133] N. Shaigan, D. G. Ivey, and W. Chen. Metal–Oxide Scale Interfacial Imperfections and Performance of Stainless Steels Utilized as Interconnects in Solid Oxide Fuel Cells. *Journal of The Electrochemical Society* **156** (2009), B765–B770. DOI: 10.1149/1.3116252.
- [134] M. Stanislawski, E. Wessel, K. Hilpert, T. Markus, and L. Singheiser. Chromium Vaporization From High-Temperature Alloys: I. Chromia-Forming Steels and the Influence of Outer Oxide Layers. *Journal of The Electrochemical Society* **154** (2007), A295–A306. DOI: 10.1149/1.2434690.
- [135] H. Colpaert and Updated and Translated by A. L. V. da Costa e Silva. *Metallography of Steels - Interpretation of Structure and the Effects of Processing*. Ohio, USA: ASM International, 2018. ISBN: 978-1-62708-148-1.
- [136] J. Froitzheim, G. H. Meier, L. Niewolak, P. J. Ennis, H. Hattendorf, L. Singheiser, and W. J. Quadakkers. Development of High Strength Ferritic Steel for Interconnect Application in SOFCs. *Journal of Power Sources* **178** (2008), 163–173. DOI: 10.1016/j.jpowsour.2007.12.028.
- [137] K. Yamamoto, Y. Kimura, F.-G. Wei, and Y. Mishima. Design of Laves Phase Strengthened Ferritic Heat Resisting Steels in the Fe–Cr–Nb(–Ni) System. *Materials Science and Engineering: A* **329–331** (2002), 249–254. DOI: 10.1016/S0921-5093(01)01586-6.
- [138] W. J. Quadakkers, J. Piron-Abellan, V. Shemet, and L. Singheiser. Metallic Interconnectors for Solid Oxide Fuel Cells – A Review. *Materials at High Temperatures* **20** (2003), 115–127. DOI: 10.1179/mht.2003.015.
- [139] J. Stringer. The Reactive Element Effect in High-Temperature Corrosion. *Materials Science and Engineering: A* **120–121** (1989), 129–137. DOI: 10.1016/0921-5093(89)90730-2.
- [140] K. A. Unocic, J. Bergholz, T. Huang, D. Naumenko, B. A. Pint, R. Vaßen, and W. J. Quadakkers. High-Temperature Behavior of Oxide Dispersion Strengthening

- CoNiCrAlY. *Materials at High Temperatures* **35** (2018), 108–119. DOI: 10.1080/09603409.2017.1389423.
- [141] J. T. DeMasi-Marcin and D. K. Gupta. Protective Coatings in the Gas Turbine Engine. *Surface and Coatings Technology* **68-69** (1994), 1–9. DOI: 10.1016/0257-8972(94)90129-5.
- [142] J. Klöwer. Factors Affecting the Oxidation Behaviour of Thin Fe-Cr-Al Foils. Part II: The Effect of Alloying Elements: Overdoping. *Materials and Corrosion* **51** (2000), 373–385. DOI: 10.1002/(sici)1521-4176(200005)51:5<373::Aid-maco373>3.0.Co;2-o.
- [143] K. L. Luthra and C. L. Briant. Mechanism of Adhesion of Alumina on MCrAlY Alloys. *Oxidation of Metals* **26** (1986), 397–416. DOI: 10.1007/BF00659344.
- [144] D. P. Whittle and J. Stringer. Improvements in High Temperature Oxidation Resistance by Additions of Reactive Elements or Oxide Dispersions. *Philosophical Transactions of the Royal Society of London. Series A, Mathematical and Physical Sciences* **295** (1980), 309–329. DOI: 10.1098/rsta.1980.0124.
- [145] W. J. Quadakkers, H. Holzbrecher, K. G. Briefs, and H. Beske. Differences in Growth Mechanisms of Oxide Scales Formed on ODS and Conventional Wrought Alloys. *Oxidation of Metals* **32** (1989), 67–88. DOI: 10.1007/bf00665269.
- [146] C. M. Cotell, G. J. Yurek, R. J. Hussey, D. F. Mitchell, and M. J. Graham. The Influence of Implanted Yttrium on the Mechanism of Growth of Cr_2O_3 on Cr. *Journal of The Electrochemical Society* **134** (1987), 1871–1872. DOI: 10.1149/1.2100775.
- [147] D. Naumenko, B. A. Pint, and W. J. Quadakkers. Current Thoughts on Reactive Element Effects in Alumina-Forming Systems: In Memory of John Stringer. *Oxidation of Metals* **86** (2016), 1–43. DOI: 10.1007/s11085-016-9625-0.
- [148] H. Falk-Windisch, P. Malmberg, M. Sattari, J.-E. Svensson, and J. Froitzheim. Determination of the Oxide Scale Growth Mechanism Using ^{18}O -Tracer Experiments in Combination With Transmission Electron Microscopy and Nanoscale Secondary Ion Mass Spectrometry. *Materials Characterization* **136** (2018), 128–133. DOI: 10.1016/j.matchar.2017.12.001.
- [149] H. Falk-Windisch. “Improved Oxidation Resistance and Reduced Cr Vaporization from Thin-Film Coated Solid Oxide Fuel Cell Interconnects”. Doctor of Philosophy. Gothenburg, Sweden: Chalmers University of Technology, 2017. ISBN: 978-91-7597-540-5.
- [150] J. C. W. Mah, A. Muchtar, M. R. Somalu, and M. J. Ghazali. Metallic Interconnects for Solid Oxide Fuel Cell: A Review on Protective Coating and Deposition Techniques. *International Journal of Hydrogen Energy* **42** (2016), 9219–9229. DOI: 10.1016/j.ijhydene.2016.03.195.
- [151] W. J. Quadakkers, H. Greiner, M. Hänsel, A. Pattanaik, A. S. Khanna, and W. Malléner. Compatibility of Perovskite Contact Layers Between Cathode and Metallic Interconnector Plates of SOFCs. *Solid State Ionics* **91** (1996), 55–67. DOI: 10.1016/S0167-2738(96)00425-0.
- [152] M. Stanislawski, J. Froitzheim, L. Niewolak, W. J. Quadakkers, K. Hilpert, T. Markus, and L. Singheiser. Reduction of Chromium Vaporization From SOFC

- Interconnectors by Highly Effective Coatings. *Journal of Power Sources* **164** (2007), 578–589. DOI: 10.1016/j.jpowsour.2006.08.013.
- [153] A. Petric and H. Ling. Electrical Conductivity and Thermal Expansion of Spinel at Elevated Temperatures. *Journal of the American Ceramic Society* **90** (2007), 1515–1520. DOI: 10.1111/j.1551-2916.2007.01522.x.
- [154] J. Froitzheim and J.-E. Svensson. Multifunctional Nano-Coatings for SOFC Interconnects. *ECS Transactions* **35** (2011), 2503–2508. DOI: 10.1149/1.3570248.
- [155] M. Mirzaei, A. Simchi, M. A. Faghihi-Sani, and A. Yazdanyar. Electrophoretic Deposition and Sintering of a Nanostructured Manganese–Cobalt Spinel Coating for Solid Oxide Fuel Cell Interconnects. *Ceramics International* **42** (2016), 6648–6656. DOI: 10.1016/j.ceramint.2016.01.012.
- [156] Å. H. Persson, L. Mikkelsen, P. V. Hendriksen, and M. A. J. Somers. Interaction Mechanisms Between Slurry Coatings and Solid Oxide Fuel Cell Interconnect Alloys During High Temperature Oxidation. *Journal of Alloys and Compounds* **521** (2012), 16–29. DOI: 10.1016/j.jallcom.2011.12.095.
- [157] S.-I. Lee, J. Hong, H. Kim, J.-W. Son, J.-H. Lee, B.-K. Kim, H.-W. Lee, and K. J. Yoon. Highly Dense Mn-Co Spinel Coating for Protection of Metallic Interconnect of Solid Oxide Fuel Cells. *Journal of The Electrochemical Society* **161** (2014), F1389–F1394. DOI: 10.1149/2.0541414jes.
- [158] X. Deng, P. Wei, M. R. Bateni, and A. Petric. Cobalt Plating of High Temperature Stainless Steel Interconnects. *Journal of Power Sources* **160** (2006), 1225–1229. DOI: 10.1016/j.jpowsour.2006.03.024.
- [159] H. Falk-Windisch, J. Claquesin, M. Sattari, J.-E. Svensson, and J. Froitzheim. Co- and Ce/Co-coated Ferritic Stainless Steel as Interconnect Material for Intermediate Temperature Solid Oxide Fuel Cells. *Journal of Power Sources* **343** (2017), 1–10. DOI: 10.1016/j.jpowsour.2017.01.045.
- [160] J. W. Fergus. Metallic Interconnects for Solid Oxide Fuel Cells. *Materials Science and Engineering A* **397** (2005), 271–283. DOI: 10.1016/j.msea.2005.02.047.
- [161] A. Holt and P. Kofstad. Electrical Conductivity and Defect Structure of Cr_2O_3 . II. Reduced Temperatures ($<\sim 1000^\circ\text{C}$). *Solid State Ionics* **69** (1994), 137–143. DOI: 10.1016/0167-2738(94)90402-2.
- [162] A. Holt and P. Kofstad. Electrical Conductivity and Defect Structure of Cr_2O_3 . I. High Temperatures ($>\sim 1000^\circ\text{C}$). *Solid State Ionics* **69** (1994), 127–136. DOI: 10.1016/0167-2738(94)90401-4.
- [163] P. Huczowski, N. Christiansen, V. Shemet, L. Niewolak, J. Piron-Abellan, L. Singheiser, and W. J. Quadackers. Growth Mechanisms and Electrical Conductivity of Oxide Scales on Ferritic Steels Proposed as Interconnect Materials for SOFC's. *Fuel Cells* **6** (2006), 93–99. DOI: 10.1002/fuce.200500110.
- [164] J. A. Crawford and R. W. Vest. Electrical Conductivity of Single-Crystal Cr_2O_3 . *Journal of Applied Physics* **35** (1964), 2413–2418. DOI: 10.1063/1.1702871.
- [165] W. C. Hagel and A. U. Seybolt. Cation Diffusion in Cr_2O_3 . *Journal of The Electrochemical Society* **108** (1961), 1146–1152. DOI: 10.1149/1.2427973.
- [166] H. Nagai, T. Fujikawa, and K.-i. Shoji. Electrical Conductivity of Cr_2O_3 Doped With La_2O_3 , Y_2O_3 and NiO . *Transactions of the Japan Institute of Metals* **24** (1983), 581–588. DOI: 10.2320/matertrans1960.24.581.

- [167] J. H. Park and K. Natesan. Electronic Transport in Thermally Grown Cr_2O_3 . *Oxidation of Metals* **33** (1990), 31–54. DOI: 10.1007/BF00665668.
- [168] K. Huang, P. Y. Hou, and J. B. Goodenough. Characterization of Iron-Based Alloy Interconnects for Reduced Temperature Solid Oxide Fuel Cells. *Solid State Ionics* **129** (2000), 237–250. DOI: 10.1016/S0167-2738(99)00329-X.
- [169] L. Latu-Romain, Y. Parsa, S. Mathieu, M. Vilasi, and Y. Wouters. Chromia Scale Thermally Grown on Pure Chromium Under Controlled $p(\text{O}_2)$ Atmosphere: I. Spallation Investigation Using Photoelectrochemical Techniques at a Mesoscale. *Oxidation of Metals* **90** (2018), 255–266. DOI: 10.1007/s11085-018-9844-7.
- [170] S. Chandra-Ambhorn, S. Hayashi, L. Latu-Romain, and P. Wongpromrat. High Temperature Oxidation of Stainless Steels. *Solid State Phenomena* **300** (2020), 81–106. DOI: 10.4028/www.scientific.net/SSP.300.81.
- [171] L. Latu-Romain, Y. Parsa, S. Mathieu, M. Vilasi, M. Ollivier, A. Galerie, and Y. Wouters. Duplex n- and p-Type Chromia Grown on Pure Chromium: A Photoelectrochemical and Microscopic Study. *Oxidation of Metals* **86** (2016), 497–509. DOI: 10.1007/s11085-016-9648-6.
- [172] L. Latu-Romain, S. Mathieu, M. Vilasi, G. Renou, S. Coindeau, A. Galerie, and Y. Wouters. The Role of Oxygen Partial Pressure on the Nature of the Oxide Scale on a NiCr Model Alloy. *Oxidation of Metals* **88** (2017), 481–493. DOI: 10.1007/s11085-016-9670-8.
- [173] L. Latu-Romain, Y. Parsa, S. Mathieu, M. Vilasi, A. Galerie, and Y. Wouters. Towards the Growth of Stoichiometric Chromia on Pure Chromium by the Control of Temperature and Oxygen Partial Pressure. *Corrosion Science* **126** (2017), 238–246. DOI: 10.1016/j.corsci.2017.07.005.
- [174] A. Holt and P. Kofstad. Electrical Conductivity and Defect Structure of Mg-Doped Cr_2O_3 . *Solid State Ionics* **100** (1997), 201–209. DOI: 10.1016/S0167-2738(97)00352-4.
- [175] A. Holt and P. Kofstad. Electrical Conductivity of Cr_2O_3 Doped With TiO_2 . *Solid State Ionics* **117** (1999), 21–25. DOI: 10.1016/S0167-2738(98)00244-6.
- [176] A. Navrotsky and O. J. Kleppa. The Thermodynamics of Cation Distributions in Simple Spinel. *Journal of Inorganic and Nuclear Chemistry* **29** (1967), 2701–2714. DOI: 10.1016/0022-1902(67)80008-3.
- [177] Z. Lu, J. Zhu, E. A. Payzant, and M. P. Paranthaman. Electrical Conductivity of the Manganese Chromite Spinel Solid Solution. *Journal of the American Ceramic Society* **88** (2005), 1050–1053. DOI: 10.1111/j.1551-2916.2005.00205.x.
- [178] N. Sakai, T. Horita, Y. P. Xiong, K. Yamaji, H. Kishimoto, M. E. Brito, H. Yokokawa, and T. Maruyama. Structure and Transport Property of Manganese–Chromium–Iron Oxide as a Main Compound in Oxide Scales of Alloy Interconnects for SOFCs. *Solid State Ionics* **176** (2005), 681–686. DOI: 10.1016/j.ssi.2004.11.012.
- [179] Z. Yang, M. S. Walker, P. Singh, J. W. Stevenson, and T. Norby. Oxidation Behavior of Ferritic Stainless Steels Under SOFC Interconnect Exposure Conditions. *Journal of the Electrochemical Society* **151** (2004), B669–B678. DOI: 10.1149/1.1810393.

- [180] A. W. Bredvei Skilbred and R. Haugsrud. The Effect of Dual Atmosphere Conditions on the Corrosion of Sandvik Sanergy HT. *International Journal of Hydrogen Energy* **37** (2012), 8095–8101. DOI: 10.1016/j.ijhydene.2011.10.096.
- [181] J. Rufner, P. Gannon, P. White, M. Deibert, S. Teintze, R. Smith, and H. Chen. Oxidation Behavior of Stainless Steel 430 and 441 at 800 °C in Single (Air/Air) and Dual Atmosphere (Air/Hydrogen) Exposures. *International Journal of Hydrogen Energy* **33** (2008), 1392–1398. DOI: 10.1016/j.ijhydene.2007.12.067.
- [182] P. Gannon and R. Amendola. High-Temperature, Dual-Atmosphere Corrosion of Solid-Oxide Fuel Cell Interconnects. *Journal of the Minerals Metals and Materials Society* **64** (2012), 1470–1476. DOI: 10.1007/s11837-012-0473-3.
- [183] Y. Zhao and J. Fergus. High Temperature Oxidation Behavior of Stainless Steel 441 in Dual Atmosphere - Effects of Flow Rate and Humidity. *ECS Transactions* **16** (2009), 57–64. DOI: 10.1149/1.3224744.
- [184] H. Kurokawa, Y. Oyama, K. Kawamura, and T. Maruyama. Hydrogen Permeation Through Fe-16Cr Alloy Interconnect in Atmosphere Simulating SOFC at 1073 K. *Journal of The Electrochemical Society* **151** (2004), A1264–A1268. DOI: 10.1149/1.1767349.
- [185] D. J. Young, J. Zurek, L. Singheiser, and W. J. Quadackers. Temperature Dependence of Oxide Scale Formation on High-Cr Ferritic Steels in Ar–H₂–H₂O. *Corrosion Science* **53** (2011), 2131–2141. DOI: 10.1016/j.corsci.2011.02.031.
- [186] J. Żurek, E. Wessel, L. Niewolak, F. Schmitz, T. U. Kern, L. Singheiser, and W. J. Quadackers. Anomalous Temperature Dependence of Oxidation Kinetics During Steam Oxidation of Ferritic Steels in the Temperature Range 550–650 °C. *Corrosion Science* **46** (2004), 2301–2317. DOI: 10.1016/j.corsci.2004.01.010.
- [187] L. Sánchez, M. P. Hierro, and F. J. Pérez. Effect of Chromium Content on the Oxidation Behaviour of Ferritic Steels for Applications in Steam Atmospheres at High Temperatures. *Oxidation of Metals* **71** (2009), 173–186. DOI: 10.1007/s11085-008-9134-x.
- [188] S. K. Yen and Y. C. Tsai. Critical Hydrogen Concentration for the Brittle Fracture of AISI 430 Stainless Steel. *Journal of The Electrochemical Society* **143** (1996), 2736–2741. DOI: 10.1149/1.1837100.
- [189] H. Kurokawa, K. Kawamura, and T. Maruyama. Oxidation Behavior of Fe–16Cr Alloy Interconnect for SOFC Under Hydrogen Potential Gradient. *Solid State Ionics* **168** (2004), 13–21. DOI: 10.1016/j.ssi.2004.02.008.
- [190] E. Essuman, G. H. Meier, J. Żurek, M. Hänsel, and W. J. Quadackers. The Effect of Water Vapor on Selective Oxidation of Fe–Cr Alloys. *Oxidation of Metals* **69** (2008), 143–162. DOI: 10.1007/s11085-007-9090-x.
- [191] G. R. Holcomb, M. Ziomek-Moroz, S. D. Cramer, B. S. Covino, and S. J. Bullard. Dual-Environment Effects on the Oxidation of Metallic Interconnects. *Journal of Materials Engineering and Performance* **15** (2006), 404–409. DOI: 10.1361/105994906x117198.
- [192] Z. Yang, K. S. Weil, D. M. Paxton, and J. W. Stevenson. Selection and Evaluation of Heat-Resistant Alloys for SOFC Interconnect Applications. *Journal of The Electrochemical Society* **150** (2003), A1188–A1201. DOI: 10.1149/1.1595659.

- [193] B. Tveten, G. Hultquist, and T. Norby. Hydrogen in Chromium: Influence on the High-Temperature Oxidation Kinetics in O₂, Oxide-Growth Mechanisms, and Scale Adherence. *Oxidation of Metals* **51** (1999), 221–233. DOI: 10.1023/a:1018866505708.
- [194] G. F. Vander Voort. *Metallography: Principles and Practice*. Materials Park, Ohio, USA: ASM International, 1999. ISBN: 978-0-87170-672-0.
- [195] J. Froitzheim, H. Ravash, E. Larsson, L. G. Johansson, and J.-E. Svensson. Investigation of Chromium Volatilization From FeCr Interconnects by a Denuder Technique. *Journal of The Electrochemical Society* **157** (2010), B1295–B1300. DOI: 10.1149/1.3462987.
- [196] C. Goebel, P. Alnegren, R. L. Faust, J.-E. Svensson, and J. Froitzheim. Influence of Pre-Oxidation on Dual Atmosphere Effect on AISI 441 Interconnects for Solid Oxide Fuel Cell Applications. *ECS Transactions* **78** (2017), 1559–1563. DOI: 10.1149/07801.1559ecst.
- [197] R. Faust. “Dual Atmosphere Corrosion of Ferritic Stainless Steel Used for Solid Oxide Fuel Cell Applications - The Importance of the Location of Pre-Oxidation Scales”. Master of Science. Gothenburg, Sweden: Chalmers University of Technology, 2017.
- [198] M.-C. Fournier-Salaün and P. Salaün. Quantitative Determination of Hexavalent Chromium in Aqueous Solutions by UV-Vis Spectrophotometer. *Central European Journal of Chemistry* **5** (2007), 1084–1093. DOI: 10.2478/s11532-007-0038-4.
- [199] E. Moore and L. Smart. *Solid State Chemistry: An Introduction*. 3rd ed. Boca Raton: CRC Taylor & Francis, 2005. ISBN: 978-0-2034-9635-0.
- [200] W. H. Bragg, W. L. Bragg, R. W. James, and H. Lipson. *The Crystalline State*. New York: Macmillan, 1934.
- [201] M. A. Olivas Ogaz. “High Temperature Corrosion of Low-Alloyed and Stainless Steels: Mechanistic Study of Chlorine Induced Corrosion”. Doctor of Philosophy. Gothenburg, Sweden: Chalmers University of Technology, 2019. ISBN: 978-91-7905-104-4.
- [202] R. F. Egerton. *Physical Principles of Electron Microscopy - An Introduction to TEM, SEM, and AEM*. 2nd ed. Switzerland: Springer International Publishing, 2016. DOI: 10.1007/978-3-319-39877-8.
- [203] K. L. Scrivener. Backscattered Electron Imaging of Cementitious Microstructures: Understanding and Quantification. *Cement and Concrete Composites* **26** (2004), 935–945. DOI: 10.1016/j.cemconcomp.2004.02.029.
- [204] J. I. Goldstein, D. E. Newbury, J. R. Michael, N. W. M. Ritchie, J. H. J. Scott, and D. C. Joy. “Secondary Electrons”. *Scanning Electron Microscopy and X-Ray Microanalysis*. Ed. by J. I. Goldstein, D. E. Newbury, J. R. Michael, N. W. M. Ritchie, J. H. J. Scott, and D. C. Joy. 4th ed. New York, USA: Springer, 2018, pp. 29–37. DOI: 10.1007/978-1-4939-6676-9_3.
- [205] J. I. Goldstein, D. E. Newbury, J. R. Michael, N. W. M. Ritchie, J. H. J. Scott, and D. C. Joy. “Backscattered Electrons”. *Scanning Electron Microscopy and X-Ray Microanalysis*. Ed. by J. I. Goldstein, D. E. Newbury, J. R. Michael, N. W. M. Ritchie, J. H. J. Scott, and D. C. Joy. 4th ed. New York, USA: Springer, 2018, pp. 15–28. DOI: 10.1007/978-1-4939-6676-9_2.

- [206] J. I. Goldstein, D. E. Newbury, J. R. Michael, N. W. M. Ritchie, J. H. J. Scott, and D. C. Joy. “X-Rays”. *Scanning Electron Microscopy and X-Ray Microanalysis*. Ed. by J. I. Goldstein, D. E. Newbury, J. R. Michael, N. W. M. Ritchie, J. H. J. Scott, and D. C. Joy. 4th ed. New York, USA: Springer, 2018, pp. 39–63. DOI: 10.1007/978-1-4939-6676-9_4.
- [207] D. B. Williams and C. B. Carter. “Diffraction in TEM”. *Transmission Electron Microscopy: A Textbook for Materials Science*. Ed. by D. B. Williams and C. B. Carter. Boston, USA: Springer, 2009, pp. 197–209. DOI: 10.1007/978-0-387-76501-3_11.
- [208] B. Talic, S. Molin, K. Wiik, P. V. Hendriksen, and H. L. Lein. Comparison of Iron and Copper Doped Manganese Cobalt Spinel Oxides as Protective Coatings for Solid Oxide Fuel Cell Interconnects. *Journal of Power Sources* **372** (2017), 145–156. DOI: 10.1016/j.jpowsour.2017.10.060.
- [209] S. N. Hosseini, M. H. Enayati, F. Karimzadeh, and A. M. Dayaghi. LaCrO₃/CuFe₂O₄ Composite-Coated Crofer 22 APU Stainless Steel Interconnect of Solid Oxide Fuel Cells. *Metallurgical and Materials Transactions A* **48** (2017), 3490–3496. DOI: 10.1007/s11661-017-4084-z.
- [210] F. Shen and K. Lu. Co₃O₄/Sm-Doped CeO₂/Co₃O₄ Trilayer Coating on AISI 441 Interconnect for Solid Oxide Fuel Cells. *ACS Applied Materials & Interfaces* **9** (2017), 6022–6029. DOI: 10.1021/acsami.6b14562.
- [211] H. Falk-Windisch, J. Claquesin, J.-E. Svensson, and J. Froitzheim. The Effect of Metallic Co-Coating Thickness on Ferritic Stainless Steels Intended for Use as Interconnect Material in Intermediate Temperature Solid Oxide Fuel Cells. *Oxidation of Metals* **89** (2018), 233–250. DOI: 10.1007/s11085-017-9782-9.
- [212] J. A. K. Tareen, A. Małecki, J. P. Doumerc, J. C. Launay, P. Dordor, M. Pouchard, and P. Hagenmuller. Growth and Electrical Properties of Pure and Ni-Doped Co₃O₄ Single Crystals. *Materials Research Bulletin* **19** (1984), 989–997. DOI: 10.1016/0025-5408(84)90212-5.
- [213] M. W. Lundberg, R. Berger, J. Westlinder, and H. Holmberg. Multilayered Pre-coated AISI 441 for Solid Oxide Fuel Cell Interconnects. *ECS Transactions* **68** (2015), 1681–1689. DOI: 10.1149/06801.1681ecst.
- [214] J. Takada, S. Yamamoto, S. Kikuchi, and M. Adachi. Internal Oxidation of Fe-Al Alloys in the α -Phase Region. *Oxidation of Metals* **25** (1986), 93–105. DOI: 10.1007/BF00807998.
- [215] J. Takada and M. Adachi. Determination of Diffusion Coefficient of Oxygen in α -Iron From Internal Oxidation Measurements in Fe-Si Alloys. *Journal of Materials Science* **21** (1986), 2133–2137. DOI: 10.1007/BF00547959.
- [216] P. I. Williams and R. G. Faulkner. Chemical Volume Diffusion Coefficients for Stainless Steel Corrosion Studies. *Journal of Materials Science* **22** (1987), 3537–3542. DOI: 10.1007/BF01161455.
- [217] F. Gesmundo and F. Viani. Transition From Internal to External Oxidation for Binary Alloys in the Presence of an Outer Scale. *Oxidation of Metals* **25** (1986), 269–282. DOI: 10.1007/BF01072908.
- [218] P. Huczowski, N. Christiansen, V. Shemet, J. Piron-Abellan, L. Singheiser, and W. J. Quadackers. Oxidation Induced Lifetime Limits of Chromia Forming Ferritic

- Interconnector Steels. *Journal of Fuel Cell Science and Technology* **1** (2004), 30–34. DOI: 10.1115/1.1782925.
- [219] P. Huczowski, V. Shemet, J. Piron-Abellan, L. Singheiser, W. J. Quadackers, and N. Christiansen. Oxidation Limited Life Times of Chromia Forming Ferritic Steels. *Materials and Corrosion* **55** (2004), 825–830. DOI: 10.1002/maco.200303798.
- [220] H. Falk-Windisch, J. Froitzheim, and J.-E. Svensson. Influence of Chromium Evaporation and Oxidation on Interconnect Steels at 650–850 °C. *ECS Transactions* **57** (2013), 2225–2233. DOI: 10.1149/05701.2225ecst.
- [221] A. Chyrkin, P. Huczowski, V. Shemet, L. Singheiser, and W. J. Quadackers. Sub-Scale Depletion and Enrichment Processes During High Temperature Oxidation of the Nickel Base Alloy 625 in the Temperature Range 900–1000 °C. *Oxidation of Metals* **75** (2011), 143–166. DOI: 10.1007/s11085-010-9225-3.
- [222] M. H. B. Ani, T. Kodama, M. Ueda, K. Kawamura, and T. Maruyama. The Effect of Water Vapor on High Temperature Oxidation of Fe-Cr Alloys at 1073 K. *Materials Transactions* **50** (2009), 2656–2663. DOI: 10.2320/matertrans.M2009212.
- [223] K. Segerdahl, J. E. Svensson, and L. G. Johansson. Protective and Nonprotective Behavior of 11% Cr Steel in O₂+H₂O Environment at 450–700 °C. *Journal of The Electrochemical Society* **151** (2004), B394–B398. DOI: 10.1149/1.1753584.
- [224] P. Alnegren. “Corrosion of Ferritic Stainless Steel Interconnects for Solid Oxide Cells – Challenging Operating Conditions”. Doctor of Philosophy. Gothenburg, Sweden: Chalmers University of Technology, 2018. ISBN: 978-91-7597-748-5.
- [225] V. Nemanic. Hydrogen Permeation Barriers: Basic Requirements, Materials Selection, Deposition Methods, and Quality Evaluation. *Nuclear Materials and Energy* **19** (2019), 451–457. DOI: 10.1016/j.nme.2019.04.001.
- [226] V. Bongiorno, P. Piccardo, S. Anelli, and R. Spotorno. Influence of Surface Finishing on High-Temperature Oxidation of AISI Type 444 Ferritic Stainless Steel Used in SOFC Stacks. *Acta Metallurgica Sinica (English Letters)* **30** (2017), 697–711. DOI: 10.1007/s40195-017-0543-1.
- [227] S. Leistikow, I. Wolf, and H. J. Grabke. Effects of Cold Work on the Oxidation Behavior and Carburization Resistance of Alloy 800. *Materials and Corrosion* **38** (1987), 556–562. DOI: 10.1002/maco.19870381003.
- [228] R. Amendola, P. Gannon, B. Ellingwood, K. Hoyt, P. Piccardo, and P. Genocchio. Oxidation Behavior of Coated and Preoxidized Ferritic Steel in Single and Dual Atmosphere Exposures at 800 °C. *Surface and Coatings Technology* **206** (2012), 2173–2180. DOI: 10.1016/j.surfcoat.2011.09.054.
- [229] P. E. Gannon, V. I. Gorokhovskiy, M. C. Deibert, R. J. Smith, A. Kayani, P. T. White, S. Sofie, Z. Yang, D. McCready, S. Visco, C. Jacobson, and H. Kurokawa. Enabling Inexpensive Metallic Alloys as SOFC Interconnects: An Investigation Into Hybrid Coating Technologies to Deposit Nanocomposite Functional Coatings on Ferritic Stainless Steels. *International Journal of Hydrogen Energy* **32** (2007), 3672–3681. DOI: 10.1016/j.ijhydene.2006.08.012.